

ATOMIC-SCALE INVESTIGATION OF STRAIN EFFECT ON SURFACE PROPERTIES OF SILICON AND MINERAL MATERIALS

Zur Erlangung des akademischen Grades einer
DOKTORIN DER NATURWISSENSCHAFTEN
(Dr. rer. nat)

von der KIT-Fakultät für Chemie und Biowissenschaften
des Karlsruher Instituts für Technologie (KIT)

genehmigte
DISSERTATION
von

MSc. Tahereh Mohammadi Hafshejani

aus
Shahrekord, Iran

KIT-Dekan: Prof. Dr. Hans-Achim Wagenknecht

Referent: PD Dr. Peter Thissen

Korreferent: Prof. Dr. Felix Studt

Tag der mündlichen Prüfung: 19/10/2021

Die vorliegende Arbeit wurde im Zeitraum von November 2018 bis September 2021 unter Anleitung von Dr. Peter Thissen am Karlsruher Institut für Technologie - Universitätsbereich angefertigt.

Hiermit bestätige ich wahrheitsgemäß, dass ich die vorliegende Arbeit im Rahmen der Betreuung durch Dr. Peter Thissen selbstständig verfasst und keine anderen Quellen und Hilfsmittel als die angegebenen verwendet habe. Wörtlich oder inhaltlich übernommene Stellen sind als solche kenntlich gemacht und die Satzung des Karlsruher Instituts für Technologie (KIT) zur Sicherung guter wissenschaftlicher Praxis wurde beachtet. Des Weiteren erkläre ich, dass ich mich derzeit in keinem weiteren laufenden Promotionsverfahren befinde und keine vorausgegangenen Promotionsversuche unternommen habe.

Karlsruhe, den 01.11.2018

Tahereh Mohammadi Hafshejani

ABSTRACT

We aim at how strain effect on surface properties of silicon and mineral materials (calcite(10.4) and cement-based material) at the atomic-level. We designed two mechanical devices with the capability of combining them with infrared (IR) spectroscopy and a drop shape analyzer system to provide an atomic-scale explanation. Density functional theory (DFT) is also used to support the experimental findings and to provide a deeper understanding of material's behavior under strain. First, the effect of strain on surface reactivity and surface chemistry of hydrogen terminated silicon (H-Si(111)) is studied. The strain effect on microstructure of H-Si(111) is discovered using IR spectra taken after applying strain at various values (0.006-1.0 / percent), which aids in the construction of a correct model for our DFT calculations. The surface reactivity of unstrained and strained H-Si(111) against liquid water is then studied at various reaction times. The surface reactivity of samples against liquid water is controlled using the Si-H band intensity as a probe. The surface chemistry of strained H-Si(111) after reactivity with water is discovered using IR spectra and DFT calculations. Second, we studied how the binding energy, the vibrational frequencies and the adsorption geometries of carbon monoxide on the calcite(10.4) surface are modified when the solid is subjected to strain. The parameters controlling the thermodynamics of adsorption such as the adsorption energy, the vibrational frequencies of the adsorbed molecules and the interaction energy between the molecules have been calculated using DFT calculations. Moving forward, our research is inspired by a desire to detect the energy dissipation mechanism in cement-based materials, which is actually one of the most widely used compounds in construction. To do so, a series of polyurethane triple-shape polymers were synthesized, and polymer-coated SiO₂ particles were added to the cement matrix. The contribution of each compound (polymer, SiO₂ particle, and cement matrix) to energy dissipation and crack propagation in strained modified cement samples was determined using in-situ IR spectroscopy.

ZUSAMMENFASSUNG

Unser Ziel ist es, den Einfluss der Dehnung auf die Oberflächenchemie von silizium- und mineralbasierten Materialien (Kalzit(10.4) und zementbasiertes Material) auf atomarer Ebene zu untersuchen. Hierzu haben wir zwei mechanische Geräte entwickelt, die mit Infrarotspektroskopie und einem Kontaktwinkelanalyzesystem kombiniert werden, um eine Erklärung im atomaren Maßstab zu liefern. Die Dichtefunktionaltheorie (DFT) wird verwendet, um die experimentellen Ergebnisse zu unterstützen und ein tieferes Verständnis des Materialverhaltens unter Belastung zu ermöglichen. Zuerst wird der Einfluss der Spannung auf die Oberflächenreaktivität und die Oberflächenchemie von Silizium mit endständigem Wasserstoff (H-Si(111)) untersucht. Dehnungseffekte auf die Mikrostruktur von H-Si(111) werden mit Hilfe von IR-Spektren aufgedeckt, die nach der Anwendung von Dehnungen bei verschiedenen Werten (0.006-1.0 / Prozent) aufgenommen wurden. Diese Daten sollen zur Konstruktion eines korrekten Modells für unsere DFT-Berechnungen dienen. Anschließend wird die Oberflächenreaktivität von ungespanntem und gespanntem H-Si(111) gegenüber flüssigem Wasser bei verschiedenen Reaktionszeiten untersucht. Die Oberflächenreaktivität von Materialproben gegenüber flüssigem Wasser wird unter Verwendung der Si-H-Bandenintensität als Sonde kontrolliert. Die Oberflächenchemie von gespanntem H-Si(111) nach Reaktivität mit Wasser wird mithilfe von IR-Spektren und DFT-Rechnungen aufgeklärt. Zweitens haben wir untersucht, wie sich die Bindungsenergie, Schwingungsfrequenzen und Adsorptionsgeometrien von Kohlenmonoxid auf der Kalzit(10.4)oberfläche verändern, wenn der Festkörper einer Belastung ausgesetzt wird. Die Parameter Adsorptionsenergie, Schwingungsfrequenzen der adsorbierten Moleküle und die Wechselwirkungsenergie zwischen den Molekülen, welche die Thermodynamik der Adsorption steuern, wurden unter Verwendung der Dichtefunktionaltheorie berechnet. Für die Zukunft ist unsere Forschung von dem Wunsch inspiriert, den Energiedissipationsmechanismus in zementbasierten Materialien zu erkennen, die aktuell eine der am häufigsten verwendeten Verbindungen im Bauwesen sind. Hierzu wurden eine Reihe von Polyurethan-Triple-Shape-Polymeren synthetisiert und der Zementmatrix wurden polymerbeschichtete SiO₂-Partikel zugesetzt. Der Beitrag einer jeden Komponente (Polymer, SiO₂-Partikel und Zementmatrix) zur Energiedissipation und Rissausbreitung in belasteten modifizierten Zementproben wurde mit In-situ-IR-Spektroskopie bestimmt.

Declaration

I, Tahereh Mohammadi Hafshejani declare that this thesis entitled “ATOMIC-SCALE INVESTIGATION OF STRAIN EFFECT ON SURFACE PROPERTIES OF SILICON AND MINERAL MATERIALS” and the works presented in it are my own works under the supervision of PD Dr. Peter Thissen at the Institute of Functional Interface (IFG), at the Karlsruhe Institute of Technology (KIT).

I confirm that:

- This work was done wholly while in candidature for a research degree at KIT.
- The whole thesis was written by me and no other sources other than the specified were used.
- The roles of ensuring good scientific practice of the Karlsruhe Institute of Technology (KIT) have been used and the submission and archiving of the primary data, in accordance with section A (6) of the rules for ensuring good scientific practice of KIT, has been ensured.
- The electronic version of the work is consistent with the written version.
- Where I have consulted the published work of others, this is always clearly attributed.
- I have acknowledged all main sources of help.
- Where the thesis is based on work done by myself jointly with others, I have made clear exactly what was done by others and what I have contributed myself.
- Furthermore, I declare that I did not undertake any previous doctoral studies and that I am currently not enrolled in any other ongoing doctoral procedure.

Signature:

Date

Deklaration

Ich, Tahereh Mohammadi Hafshejani, erkläre, dass diese Thesis mit dem Titel “UNTERSUCHUNG DER WIRKUNG VON DEHNUNGEN AUF DIE OBERFLÄCHENEIGENSCHAFTEN VON SILIZIUM UND MINERALISCHEN MATERIALIEN AUF ATOMARER SKALA“ und die darin vorgestellten Arbeiten von mir selbst unter der Aufsicht von Dr. Peter Thissen am Institut für Funktionelle Grenzflächen sind (IFG) am Karlsruher Institut für Technologie (KIT) durchgeführt worden sind.

Ich bestätige hiermit:

- Diese Arbeit wurde vollständig während der Kandidatur für ein Forschungsstudium am KIT durchgeführt wurde.

- Die gesamte Arbeit wurde von mir verfasst und es wurden keine anderen Quellen als die angegebenen verwendet.

- Die Rolle der Gewährleistung einer guten wissenschaftlichen Praxis des Karlsruher Instituts für Technologie (KIT) wurde angewendet und die Übermittlung und Archivierung der Primärdaten gemäß Abschnitt A (6) der Regeln zur Gewährleistung einer guten wissenschaftlichen Praxis des KIT wurden sichergestellt.

- Die elektronische Fassung des Werkes entspricht der schriftlichen Fassung.

- Im falls, dass ich die veröffentlichten Arbeiten anderer konsultiert habe, wird dies immer eindeutig zugeordnet.

- Ich habe alle wichtigen Hilfsquellen zur Kenntnis genommen.

- Wenn die Arbeit auf Arbeiten basiert, die ich selbst gemeinsam mit anderen geleistet habe, habe ich kenntlich gemacht, was genau von anderen geleistet wurde und was ich selbst beigetragen habe.

- Des Weiteren erkläre ich, dass ich kein vorheriges Promotionsstudium absolviert habe und mich derzeit nicht in einem anderen laufenden Promotionsverfahren befinde.

Unterschrift:

Datum:

TABLE OF CONTENTS

Chapter 1.....	1
1. INTRODUCTION	1
1.1. General Remarks.....	1
1.2. Motivations.....	1
1.3. Research Objectives.....	4
1.4. Research Methodology.....	4
1.5. Layout of the Thesis.....	4
1.6. Summary.....	5
Chapter 2.....	6
2. THEORETICAL BACKGROUND	6
2.2. Adsorption of CO on calcite(10.4).....	7
2.2.1. Strain effect on adsorption process	7
2.2.2. Calcium carbonate (CaCO ₃).....	8
2.3. Strain effect on cement-based materials.....	9
2.4. Definition of strain and stress.....	11
2.4.1. Strain tensor.....	11
2.4.2. Stress tensor.....	12
2.5. Structure of single crystal silicon surface.....	13
2.5.1 Silicon surface preparation	15
2.6. Wetting	16
2.6.1. Surfaces and wetting.....	16
2.6.2. Theoretical model of surface wettability of flat surfaces.....	16
2.7. Computational method.....	17
2.7.1. The Schrödinger equation	17
2.7.2. Density Functional Theory	18
2.7.3. FTIR calculation	19
2.7.4. Locating Transition States	20
Chapter 3.....	22
3. INSTRUMENTATION	22
3.1. Bending test.....	22
3.2. New mechanical setup (called Bieger) for combining with IR spectroscopy	23
3.2.1. An introduction to the device and its performance.....	23
3.2.2. Calculation of strain, stress and force equations	25
3.3. New mechanical machine to combine with drop shape analyzer device	26
3.4. Analytical method.....	28
3.4.1. Fourier Transform Infrared Spectroscopy (FTIR).....	28
3.4.1.1. Basic principle	28
3.4.2. Instrumentation	29
Chapter 4.....	31
4. STRAIN EFFECT ON THE OXIDATION OF HYDROGEN TERMINATED SILICON (111)	31
4.1. Surface reactivity of hydrogen terminated Si(111).....	31
4.2. Methodology.....	31
4.3. Strain effect on hydrogen terminated Si(111) / experiment (I).....	35
4.4. Surface reactivity of unstrained H-Si(111) towards liquid water/experiment (II)	39

4.5.	Surface reactivity of strained H-Si(111) towards liquid water / experiment (III).....	41
4.6.	Conclusion.....	44
Chapter 5.....		45
5.	STRAIN EFFECT ON CO ADSORPTION ON CALCITE(10.4) SURFACE	45
5.1.	Aims and objectives	45
5.2.	Methodology.....	45
5.2.1.	Infrared reflection absorption spectroscopy.....	45
5.2.2.	Non-contact atomic force microscopy (NC-AFM)	46
5.3.	Computational method.....	47
5.4.	Results and Discussion	48
5.4.1.	Experimental part.....	48
5.4.2.	Computational part.....	51
5.4.2.1.	CO adsorption on unstrained calcite(10.4)	51
5.4.2.2.	CO adsorption on strained calcite(10.4).....	53
5.4.2.3.	Effect of strain on CO adsorption.....	54
5.5.	CONCLUSION.....	57
Chapter 6.....		59
6.	MONITORING THE CRACK PROPAGATION IN CEMENT BASED MATERIALS WHILE BENDING TEST59	
6.1.	Novelty of instrumental method	59
6.2.	The importance of energy dissipation in cement-based materials.....	59
6.3.	Adding admixtures in cement-based materials	60
6.4.	General view	60
6.5.	Methodology.....	60
6.5.1.	Chemicals	60
6.5.2.	Preparation of polymer coated particles and cement-based composites	61
6.5.3.	In-situ FTIR measurement	62
6.5.4.	Scanning Electron Microscope (SEM) analysis	62
6.5.5.	Nanoindentation investigation	62
6.6.	Synthesis and characterization	63
6.7.	In-situ IR measurements during mechanical test	65
6.8.	Summary.....	71
Chapter 7.....		72
7.	CONCLUSION AND RECOMMENDATIONS	72
7.1.	General Remarks.....	72
7.2.	Research Objectives and Outcomes	72
7.3.	Recommendations and Scope for Future Research.....	73
REFERENCES		75
APPENDIX		85
LIST OF ABBREVIATIONS.....		105
LIST OF FIGURES		107
LIST OF TABLES		112
ACKNOWLEDGEMENTS		113

Chapter 1

1. INTRODUCTION

1.1. General Remarks

Silicon represents the most technologically relevant surface used for applications in photonics or electronics while mineral materials such as calcite and cement-based materials constitutes a large portion of building raw materials, three of which constitute important classes of hard materials to be exploited for their properties. This thesis is devoted to study the strain effect on surface properties of mentioned materials at an atomic-scale. Controlled strain is applied externally as a uniaxial force using our self-made three-points mechanical devices. The surface properties of the hard surfaces probed using the applied strain are (1) oxidation and surface reactivity, (2) strain-induced changes in parameters controlling the thermodynamic of adsorption such as (adsorption energy, the vibrational frequencies) and geometry of the adsorbed molecule, and (3) energy dissipation process by monitoring the stretching vibration of compounds for cement-based samples. Vibrational spectroscopy, and in particular, infrared absorption spectroscopy is among the most powerful probes of fundamental processes in microelectronics and mineral materials. It provides insight into critical aspects of surface structure and reactivity by analyzing the surface vibrational frequencies, band intensities, and line shape. Using this technique, structural information in the atomic scale is obtained with an in-situ Infrared spectrometer during the mechanical test or taking IR spectra after applying mechanical force. Considering the need for innumerable assumptions and models for the latter, density functional theory (DFT) was additionally used to corroborate the findings from the experimental part.

1.2. Motivations

Lately, the number of researches about silicon has increased, all thanks to the enormous usage of this substance for the necessary parts in microelectronic devices¹⁻². The growth of SiO₂ on the silicon surface is the main reason for its excellent electrical properties^{1, 3-4}. In modern integrated circuit (IC) technology, because of lowering overall package height of profile and obtaining more functional dice per wafer unit area, decreasing the size of microelectronic circuits makes them so interesting⁵⁻⁷. In addition, due to down-scaling, the quality of the gate oxides is governed by the quality of the structural transition layer⁸⁻⁹. Therefore, although Si oxidation has been studied for many years, the formation dynamics of Si/SiO₂ interfaces remains unresolved making it a vital area of research. At the same time, considerable effort has been invested in manipulating Si oxidation kinetics. For example, uni- and biaxial strains have been used in manufacturing Si-based devices, taking advantage of the fact that tensile stress increase the overall rate of thermally grown oxides¹⁰. The effect of strain on increasing the reactivity of Si surfaces is studied, however, an atomic-level understanding of the specific

effects of strain on surface chemistry is presently not fully understood. It is therefore, imperative that the effect of strain on oxidation kinetics be studied in detail. Figure 1.1 shows a schematic representation of our hypothesis about the strain effect on microstructures and changing surface reactivity.

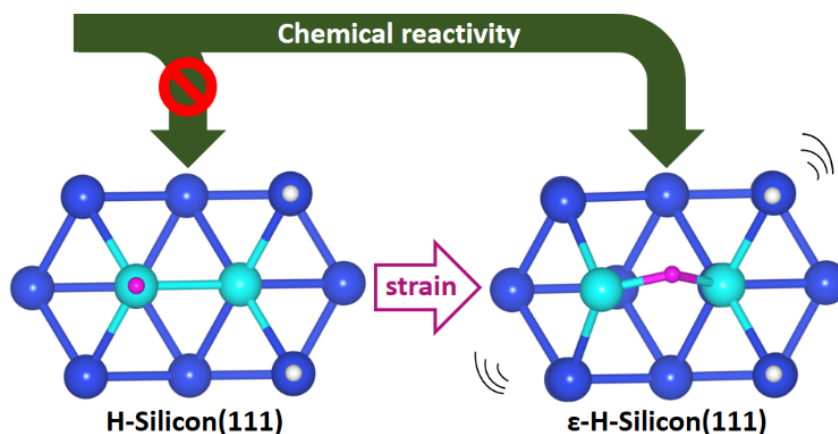


Figure 1.1. Schematic illustration of general concept behind the strain-induced changes on the microstructure which lead to increasing surface reactivity. Dark and blue colors represent silicon atoms, whereas white and pink colors represent hydrogen atoms. Our hypothesis was that strain caused changes in the microstructure of H-Silicon(111), such as hydrogen diffusion and the formation of new bonds. The formation of new bond like Si-H-Si is shown in the picture of ϵ -H-Silicon(111).

It's unsurprising that stretching a surface has an impact on the chemistry going on there. Strain alters the distance between surface atoms, causing the adsorbates' properties to vary¹¹. The only question is whether this change can be significant enough to matter, at least in certain circumstances. If this is the case, a subject of physical chemistry called "elastochemistry" could show its influence in this field. In our study, density functional calculations have been used to explore the effect of surface strain on the properties of the carbon dioxide on calcite(10.4). Calcium carbonate (CaCO_3) is a common mineral that makes up a significant portion of the Earth's crust¹². Calcite is the most stable polymorph of CaCO_3 , and it is found in all natural rock types¹³. We investigated how adsorbed CO characteristics are affected by uniform strain in a plane parallel to the surface of calcite(10.4). Figure 1.2 indicates the application of calcite as gas reservoir.

Moving forward, our study is motivated by the investigation of the strain effect on cement-based materials, which today is one of the most popular compound in building materials. Fracture mechanics, is a field of mechanics pursuing the study of the propagation of cracks in materials¹⁴. On the subject of performance of unreinforced and reinforced concrete, crack formation and crack growth have massive roles¹⁵. Fracture as a physics problem is a challenge since many of the features seen in an experiment on failure exhibit complex phenomena. Understanding why and how is important both for fracture mechanics and for the fundamental reasons that give rise to such behavior, and the understanding of how strong materials are, and why, is quite challenging. Having said this, the main goal of this part of the thesis is to investigate

the energy properties of SiO_2 @polymer–matrix composites during the fracture process. The primary characteristic of concrete deforming and fracturing is energy absorption, which can reflect the dynamic process of micro-cracks developing, strength reduction and ultimate fracture. Consequently, by analyzing energy dissipation properties of these materials during the fracture process, the damage properties (such as the crack initiation, propagation, coalescence and interaction) can be effectively reflected. Here, considering the absorption and transformation of IR spectroscopy energy into the molecular vibration, we use the indirect method to study the damping capability of our samples. Figure 1.3 depicts a schematic representation of the above-mentioned explanations for the study's concern.

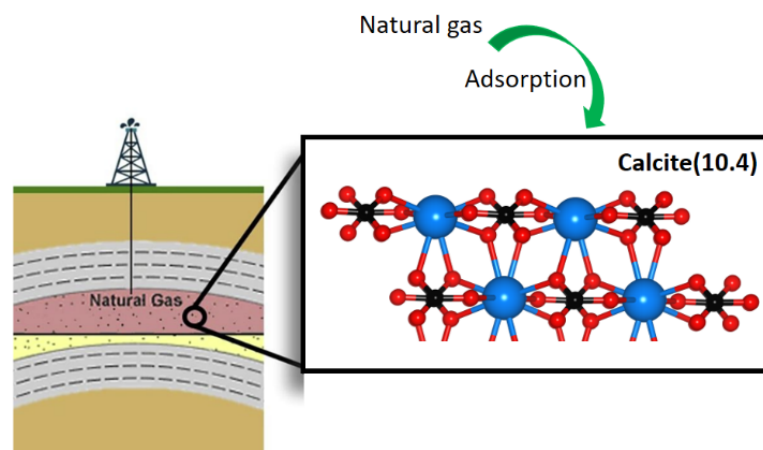


Figure 1.2. Schematic illustration of calcite(10.4) surface as one of the main gas adsorption reservoir. Carbon, oxygen, and calcium are represented by the colors black, red, and blue, respectively.

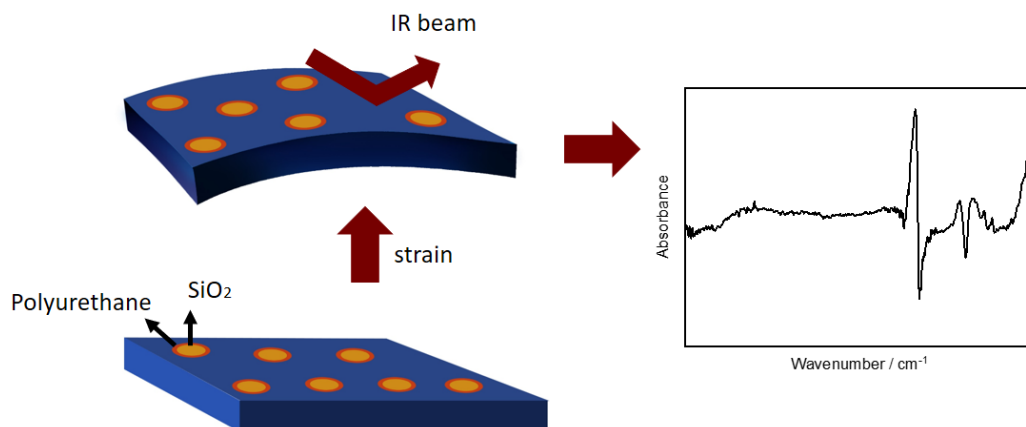


Figure 1.3. Schematic illustration of SiO_2 @polymer-matrix composite before and after mechanical test. The multiple pathways of energy adsorption by materials compounds are represented by the IR graph derived from the in-situ IR measurement during the mechanical test. Blue, yellow and orange colors represent the cement-matrix, SiO_2 particles and polyurethane, respectively. Our assumption was that the mechanical energy is often transferred through the entire process of specimen deformation and destruction that can be detected through the bond vibrations.

1.3. Research Objectives

There are three interrelated core objectives within this thesis: the investigation of (1) the surface reactivity of strained hydrogen terminated silicon during oxidation process; (2) the effect of strain on the factors that determine the thermodynamics of CO molecule adsorption on calcite(10.4); and (3) energy dissipation mechanism in reinforced cement-based materials during bending. To achieve both of these research objectives the following three items will be addressed:

- (a) strain impact on chemical reactivity of hydrogen terminated silicon at the bond level.
- (b) strain impact on adsorption energies, stretching vibration of CO molecule at different coverages and geometry of adsorbed CO on calcite(10.4).
- (c) understanding how our modified cement samples (SiO₂@polymer–matrix composites) react to mechanical loading and, as well, their mechanism in energy dissipation.

1.4. Research Methodology

To achieve the aims and objectives, multiple stages of research are required.

Stage 1: The initial stage is comprised of an extensive literature review, used primarily to highlight the major gaps and omissions in previous research in order to establish a framework for the research.

Stage 2: Method development to achieve the desired outcome of an experiment. This includes the design and fabrication of new mechanical devices with desirable dimensions to fit appropriately into an inert atmosphere unit, such as a glovebox. Furthermore, the devices were combined with an IR spectrometer and contact angle instrument to enable in-situ measurements.

Stage 3: DFT calculations are carried out to provide deeper interpretation of experimental parts, accompanied by accurate theoretical modeling.

1.5. Layout of the Thesis

Following the introduction presented, **Chapter 2** contains a literature review of the published studies which are most relevant to the presented issues on this research, and the concept behind strain and stress in crystal structure, silicon surface preparation and DFT calculations.

Chapter 3 presents details of our self-made mechanical devices, their performance to apply strain and the proposed equations to calculate the value of curvature, stress, strain and force in different bending levels.

In **Chapter 4**, we indicate how silicon surface chemistry is influenced by strain. The IR spectra presented from the strained samples and DFT calculations show significant changes induced by strain on surface structure and surface reactivity. Monitoring the surface reactivity on strained surface, with the measurements of in-situ contact angle, was the motivation of our last part's study.

In **Chapter 5**, we started with obtaining detailed information on structural, and physical

properties of natural cleaved calcite(10.4) surfaces. In the experimental part, the vibrational frequencies of adsorbed CO species were determined by polarization-resolved infrared reflection absorption spectroscopy (IRRAS). Since there were no previous experimental data of this type, the interpretation of the results was aided by employing density functional theory calculations to determine adsorption geometries, binding energies, and vibrational frequencies of carbon monoxide on the calcite(10.4) surface. Finally, the results regarding the calculated adsorption parameters on strained calcite(10.4) surface is reported.

In **Chapter 6**, we focus on the second group of materials for this thesis. We intend to discover the mechanisms of energy dissipation in SiO₂@polymer–matrix composites in order to evaluate the damping behavior of the samples. The most important point considered in our study, was to use in-situ infrared spectroscopy combined with our self-made mechanical instrument, so that we can apply loads and IR radiation simultaneously. It is assumed that the obtained IR spectra can be the source of useful information about the reaction of modified samples to mechanical loading and, also their mechanism in energy dissipation.

The final chapter, **Chapter 7**, summarises the main findings of the research, draws conclusions and identifies the shortcomings. Then we present recommendations for the anticipated applications of the current findings, and make suggestions for further research studies.

1.6. Summary

As initially highlighted in Section 1.1, strain is an overlapping core objective in all groups of samples, silicon, calcite and cement, in this study. Appending the current reports of the effects of applied strain on chemical, mechanical and optical properties of such materials, this thesis enunciates the need for the study of these effects at an atomic-scale. Thus, the goal of this dissertation is to provide deeper insight into strain impact on surface properties of silicon and mineral materials. To achieve some of the desired information, the newly constructed experimental device (three-point mechanical bending machine) combining an IR spectrometer and contact angle devices has been elaborated. Collecting these essential experimental data and precise DFT calculations act as the foundation for further knowledge that will contribute to the reaction of materials' atomic-scale to external force.

Chapter 2

2. THEORETICAL BACKGROUND

In this chapter, we mention the theory behind all the concepts and DFT calculations used in this thesis. In the first place, we introduce the theory of strain in semiconductors and some relevant studies are described, this part will clarify the importance of current study. In the following part, we overview some relevant researches regarding the calcite structure and the importance of strain effect on adsorption process. In the next section, the concept of using admixtures (polymers and SiO₂ particles) in cement-based materials, and the importance of studying energy dissipation in such materials is explained. Further, the concept of strain and stress in crystal structures, structure of single crystal silicon surface, silicon surface preparation and summary of surface wetting and contact angle, are detailed. Lastly, a brief explanation is presented for the theoretical background behind the electronic structure calculations.

2.1. Strain in Si semiconductor devices

In semiconductor physics, strain is a well-known concept¹⁶. Scaling solid-state devices has the unique property of improving cost, performance, and power, giving any company with the most up-to-date technology a significant competitive advantage in the market¹⁶⁻¹⁷. As a result, over the last 40 years, the microelectronics industry has pushed transistor feature size scaling from 10 μm to 30 nm¹⁷⁻¹⁸. Scaling was mostly just a matter of reducing the feature size at this time. However, major changes occurred during specific periods, such as the industry's transition from Si bipolar to p-channel metal-oxide-semiconductor (MOS), then n-channel MOS, and finally complementary MOS (CMOS) planar transistors in the 1980s, which has remained the dominant technology for the past two decades¹⁷. The biggest difficulty ahead was that planar CMOS transistor scaling is coming to a stop when transistor sizes reach tens of nanometers. One of the path chosen by industry to address this problem was inducing lattice strain into the Si channel without any further shrinking of the transistor gate length. In comparison to previous high-mobility, III-V semiconductors, this technique drastically modifies the band structure and addresses Si transport deficiencies¹⁷. For example, the hole conductivity may be lowered by a factor of 1/4 by changing the position of Si atoms in the face-centered cubic unit cell, which enhances mobility and results in a 100 percent increase in transistor current and remarkable performance gains¹⁷.

Meanwhile, remarkable efforts were undertaken for manipulating Si oxidation kinetics. Bearing in mind that the overall rate of thermally grown oxides elevates due to tensile stress, manufacturing of Si-based devices has been performed by uni- and biaxial strains¹⁰. With the aid of obtained data from the second-harmonic generation (SHG), the stress effect on chemical reaction was discovered¹⁹. It was shown that the reactivity of strained bonds, related to unstrained bonds at the same interface, being increased by macroscopic tensile strain. In

addition, Daum et al. explained sub-oxide forms during oxidation by measuring the evolution of resonance in SHG spectra of (111)-oriented surfaces²⁰. These studies result in a necessity to study on the strain effect on oxidation kinetics. So far, basic aspect of initial stages of oxidizing unstrained hydrogen terminated Si(111) surfaces has been clarified. Using Si-H stretch spectrum as a probe, we were able to estimate the rate of surface oxidation process, which is especially sensitive to oxygen incorporations²¹⁻²². Chabal et al. found out a non-integer order of 1.5 in the Si-H consumption rate as an indicator of a multistep mechanism of oxidation²¹. In another study by Federico et al.²³, they concluded that in density functional theory, perfect hydrogenated Si(111) doesn't react towards H₂O vapor and O₂ at room temperature. The reason for increasing the chemical reactivity due to strain effect, on the other hand, is yet unclear. That's why, both experimentally and theoretically, we're looking into the atom-scale strain effect on H-Si (111) surface reactivity.

2.2. Adsorption of CO on calcite(10.4)

2.2.1. Strain effect on adsorption process

Surface strain is caused via chemisorption, and straining a surface changes the characteristics of adsorbed molecules, according to a number of researches^{11, 24-26}. The structure of a silicon surface can be modified by bending it, as proved by Webb, Lagally, and their students²⁷⁻²⁸. They worked with a thin silicon(100). Steps are separated by two types of terraces on this surface: on one side, the dimer rows are parallel to the steps, while on the other side, they are perpendicular to the steps. These terraces provide a variety of low electron diffraction (LEED) patterns. Because the size of these terraces is altered by strain, the relative LEED intensities change when the slab is bent. Ibach and co-workers²⁹⁻³² have shown a "reciprocal" phenomenon in which chemisorption on the surface of a very thin slab causes it to bend. If adsorption causes strain, then straining the surface should be able to influence adsorption. Menzel's team³³ used noble gas ions to cause local strain under a metal surface. They subsequently demonstrated that the stretched surface had different adsorption properties than the unstrained surface. Other researchers³⁴⁻³⁶ have stressed a surface by developing a very thin metal coating on a separate metal substrate. The atoms in the film are stretched or compressed if the two lattices are mismatched but the growth is in registry.

This has an impact on the film's chemisorption properties. In this type of experiment, the chemisorption properties are affected by strain as well as electronic effects generated by attaching to a different metal substrate. Experimentally, the two effects cannot be distinguished. The effect of surface strain on the characteristics of the adsorbates was also investigated using density functional calculations. The activation energy for Ag atom diffusion on an Ag surface is modified by strain, according to Ratsch, Seitsonen, and Scheffler³⁷. Consequently, it's not surprising that stretching a surface has an impact on the chemistry that occurs there. Strain alters the distance between surface atoms, altering the characteristics of adsorbates. The only question is whether this change can be significant enough to matter in some circumstances.

2.2.2. Calcium carbonate (CaCO_3)

Calcium carbonate (CaCO_3) is a common mineral that makes up a large portion of the Earth's crust¹². Calcite is the most stable polymorph of CaCO_3 , and it is found in all natural rock types¹³. This ionic molecule is found in abundance in living creatures, and it is integrated into bones, teeth, and mussel shells, as well as playing a key part in biomineralization^{13, 38}. Calcite has been used as a building material, for agricultural soil treatment, as a sorbent, for pharmaceutical uses³⁹, and in optical systems that take advantage of its birefringence⁴⁰. This carbonate also plays a key role in the composition of the planet's atmosphere as the greatest carbon dioxide repository⁴¹. Thus, understanding calcite surfaces, their precise structure, and chemical characteristics is crucial.

Calcite is an ionic crystal made up of calcium cations (Ca^{2+}) and carbonate anions (CO_3^{2-}) that are bound together by ionic bonding. The structure has an $R\bar{3}c$ space group and is trigonal (rhombohedral holohedral percent $\bar{3}2/m$)⁴². The thermodynamically most stable calcite(10.4) surface, with a surface energy of roughly 0.59 J m^{-2} , is the easiest to cleave⁴³. Furthermore, the calcite(10.4) surface is nonpolar, classified as a type I surface by Tasker, and so has no charge ($q = 0$) and no dipole moment ($m = 0$)⁴⁴. As a result, the majority of past surface investigations for this material have focused on this surface. Within the (1×1) unit cell (with a unit cell size of $5.0 \times 8.1 \text{ \AA}$), the calcite(10.4) surface (a structural model is replicated in Figure. 2.1), there are two calcium atoms and two carbonate groups, both of which are present in the top layer. Because the two carbonate groups are rotated in relation to one another, the upmost oxygen atom along the $[42\bar{1}]$ direction points either to the left or to the right⁴⁵⁻⁴⁶.

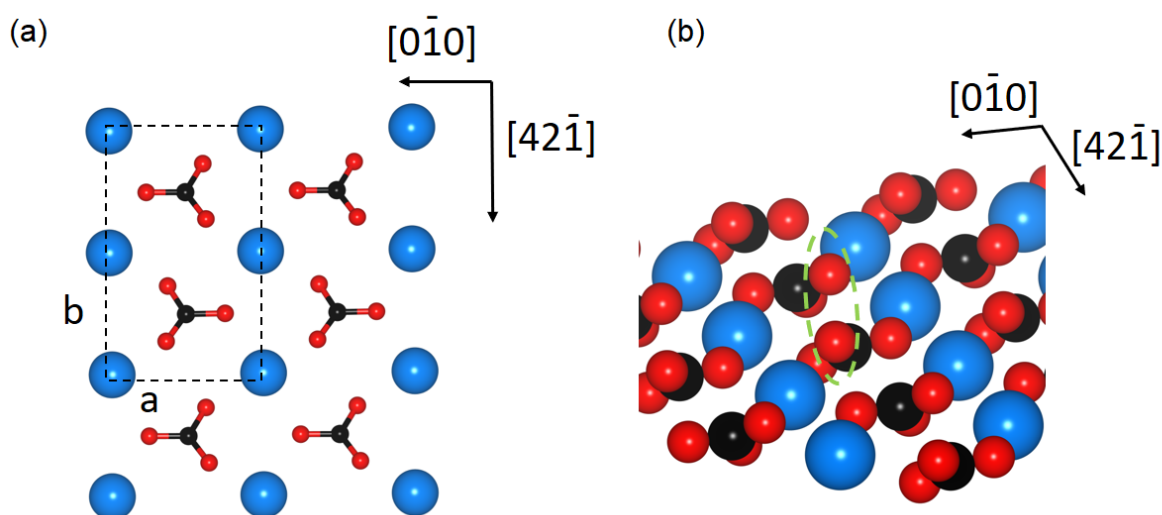


Figure 2.1. Top (a) and side (b) views of the (1×1) calcite(10.4) surface model ($a = 5.0 \text{ \AA}$ and $b = 8.1 \text{ \AA}$). The marked green section shows the atoms exposed at the surface, revealing that the oxygens are located at two different but equivalent positions. (red: oxygen, black: carbon, blue: calcium).

Geometrical complexity is a feature of calcite reservoirs⁴⁷, which takes into account pore size, permeability, stress caused by changes in thermal characteristics throughout the drilling

operation, and the geology of the rock itself⁴⁸⁻⁵⁰. Temperature and pressure fluctuations that occur naturally in the reservoir's rocks cause stress, producing a deformation in the rock structure (strain)⁵¹. The stress-strain curve of calcite has been studied experimentally. According to the data, the elastic zone of calcite is between 0 and 5% strain⁵²⁻⁵³. Therefore, natural thermodynamics and environmental changes frequently impact the geometrical features of reservoir rocks. These variables could change the distribution and volume of gas in the reservoir as it was shown⁵⁴. Here, we study the influence of strain on the adsorption of CO molecule in tight-gas carbonate reservoirs, which are represented by calcite, using density functional theory calculations.

2.3. Strain effect on cement-based materials

Even for the progressive science of today, finding the fracturing process of material is an essential problem for science and engineering. However, the effects of geometry, loading conditions, and material characteristics on the strength of materials have been studied empirically from ancient times. Concrete, the globally-popular construction substance, is used in major infrastructure projects such as bridges, tunnels, dams, railways, and wharves. Due to the rapid economic development and urbanization, there's a visible increase in the amount of concrete usage, especially in China⁵⁵. However, as the usage duration of concrete extends, many problems threaten its durability⁵⁶⁻⁵⁸. Such as cracks, erosion of large-scale areas or even collapse, these issues occur frequently, which have decreased the safety and reliability of construction. The life expectancy of about 600000 bridges in America is 42 years, with an estimated \$ 76 billion in need to deal with the damage problems. According to the ASCE's Failure to Act report on the costs of poor infrastructure, deficient bridges and pavements cost \$ 58 billion in 2020. If these bridges remain unattended, the costs would jump to \$ 651 billion by 2040⁵⁵. In Europe and some Asian countries, the annual repair cost has exceeded the cost of newly built constructions. Then in the recent decades, the concrete repairmen industry has become diverse and developed rapidly⁵⁹⁻⁶¹. Another problem regarding concrete structures is the energy dissipation and ductile properties¹⁵. The stress-strain relationship in concrete is non-linear and this material does not generally obey hook's law, thus it's not possible for an elastic limit to be identified. The result of this phenomenon is the sudden failure of concrete, which classifies this material as a brittle one¹⁵. The foundation of concrete matrix damage is the crack propagation which may occur at the aggregate-paste interface⁶². The position of crack initiation is depended to the bonds and the local stress positions. Therefore, to be able to discuss this action, interfacial transition zone (ITZ) comes into attention. ITZ is considered as the weakest zone in the matrix, which affects the strength of concrete extremely⁶³. ITZ is referred to the zone around the aggregates or fiber in which the microstructure of the paste is different than that of the main paste⁶⁴. To make an example, it is stated that increasing flexibility is usually associated with bond's failure in the ITZ of fibers, which required large amount of energy. For the ability of improving mechanical characteristics of concrete, the weak zones must also be strengthened. Also, for dealing with the mentioned challenges of concrete and improving its

performance on these areas, adding special materials to concrete can be a good solution. However, this method is nothing close to being new. The oldest available written scripts date back to 1909⁶⁵.

The polymer addition into concrete mixture could be also useful for eliminating concrete limitation⁶⁶. In many decades, this mixture was also used for widening the material's application. There are different ways of utilizing polymer, as binder with or even without cement in form of polymer modified concrete, polymer reinforcement concrete and even fillers⁶⁷. For improving the interfacial zone, polymer is used as binder, and to fill the void, polymer is used as filler⁶⁶. The result is low porosity concrete. There are variety of polymers for concrete additives, such as elastomer (natural rubber, synthetic rubber), thermoplastic (Polyvinylalcohol (PVA), styrene-acrylic, etc.), thermoset (epoxy), bituminous (tar, asphalt) and latex modification⁶⁶. Adding polymer into the mixture of concrete can help improving the earthquake resistant and damping capacity⁶⁶. Shape-memory polymers (SMPs) are a group of stimuli-responsive polymeric material⁶⁸. A feature in this type of polymer is that, if demanded, shape changes can be implemented by appropriate programming procedures⁶⁹. The most prominent among the available abilities of polymer shape-memory, is a one-way, thermally-induced shape-memory effect⁶⁸. Shape Memory Polymers (SMPs) are a fraction of smart materials. They have high potential for being used, e.g. actuators, electromechanical systems, clothing manufacturing, morphing and deployable space applications, control of structures, self-healing, biomedical devices and etc⁷⁰. The SMPs have the ability to change their shape in response to an external stimulus; the most typical one is thermal activation. Heating SMP above the glass transition temperature T_g , turns it into a soft, rubbery and easy shape-changer material. Cooling SMP below T_g afterwards, helps the material to retain the given shape (shape fixing characteristic)⁷¹⁻⁷². With heating SMP above T_g again, it returns to its original permanent shape autonomously⁷³. Using high amount of cement is essential in attaining a higher compressive strength. However, cement is a major cause of pollution. Utilizing materials with replacing the proportion of cement may lead to a rise in the compressive strength of concrete, and also a check to pollution. In addition, using silica particles in concrete mix increases the compressive, tensile and flexural strength of concrete. M. Nill et. al. (2009)⁷⁴ studied the combined effect of micro silica and colloidal nano silica on properties of concrete. As the outcome, he discovered that concrete will attain maximum compressive strength when it contains 6% micro silica and 1.5% nano silica. The highest electrical resistivity of concrete was observed at 7.5% micro and nano silica. The capillary absorption rate is lowest for the combination of 3% micro silica and 1.5% nano silica. B. W Jo et al. (2007)⁷⁵ studied the characteristics of cement mortar with Nano SiO_2 particles experimentally and observed higher strength of these blended mortars for 7 and 28 days. The microstructure analysis showed that SiO_2 acts as a filler to improve microstructure, and activator to the pozzolanic reaction. Alireza Naji Givi et al.⁷⁶ studied the effect of nano SiO_2 particles on water absorption of RHA blended concrete. They came to the conclusion that cement could be replaced up to 20% by RHA in

presence of nano SiO_2 particle up to 2%, this process improves physical and mechanical properties of concrete.

Therefore, this part of thesis presents the mechanical microscopic properties of cement-based composite, caused by SiO_2 particles coated with polymer (Figure 2.2). Then, we discuss the fracture morphology, microstructures, and the effect of these modifications on energy properties of matrix with the help of in-situ IR spectroscopy during mechanical loading. Eventually, the limitations and future perspective related to this study are introduced.

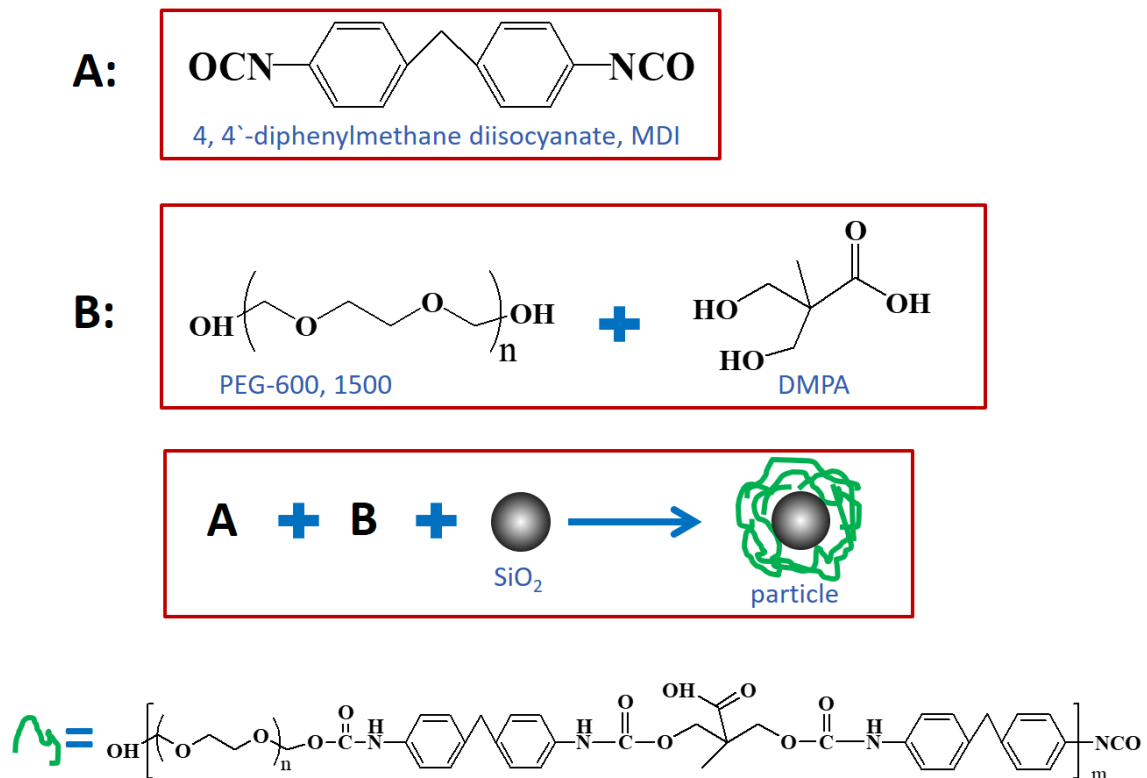


Figure 2.2. Schematic illustration of polymer (diphenylmethane diisocyanate (MDI), poly ethylene glycol (PEG) and dimethylolpropionic acid (DMPA)) coated SiO_2 particles used as admixture into the cement past. Different molecular weight of PEG (600 and 1500 g mol^{-1}) is used. $N-H$ and $C=O$ associated with the urethane groups which is expected to be observed in IR results after synthesis of polymer.

2.4. Definition of strain and stress

2.4.1. Strain tensor

Deformation causes strain in crystals, which is defined as relative lattice displacement^{16,77}. To demonstrate this concept, we utilize a 2D lattice model in Figure 2.3. As illustrated in Figure 2.3a, we can describe the unstrained lattice with two unit vectors \hat{x} , \hat{y} , which correspond to the lattice basis vectors in a basic square lattice. The two vectors are distorted in both orientation and length when the lattice is deformed uniformly, as seen in Figure 2.3b.

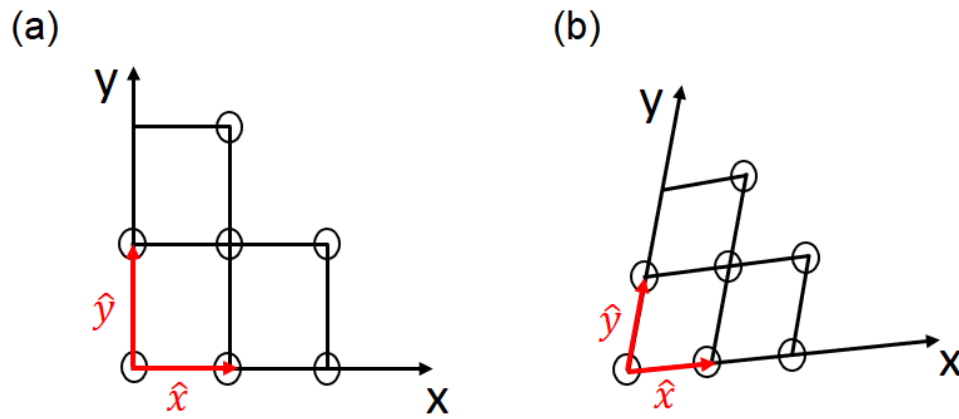


Figure 2.3. 2-dimensional diagram for (a) an undeformed lattice and (b) a deformed lattice¹⁶. \hat{x} and \hat{y} are two unit vectors to represent the unstrained lattice, and in the simple square lattice, they correspond to the lattice basis vectors.

The strain coefficients $\varepsilon_{\alpha\beta}$ are dimensionless and define the lattice's deformation. The strain tensor which is a 3×3 matrix is represented as:

$$\bar{\varepsilon} = \begin{pmatrix} \varepsilon_{xx} & \varepsilon_{xy} & \varepsilon_{xz} \\ \varepsilon_{yx} & \varepsilon_{yy} & \varepsilon_{yz} \\ \varepsilon_{zx} & \varepsilon_{zy} & \varepsilon_{zz} \end{pmatrix} \quad (2-1)$$

A tensor is a mathematical notation that describes a linear relationship between two physical quantities and is usually represented as an array. A tensor can take the form of a scalar, vector, or matrix. A scalar is a tensor with zero order, a vector is a tensor with first order, a matrix is a tensor with second rank, and so on. The tensor of strain is a second-order tensor. The strain tensor for a general varying strain can be expressed as:

$$\varepsilon_{\alpha,\beta} = \frac{\partial u_{\alpha}}{\partial x_{\beta}}, \quad u_{\alpha} = u_x, u_y, u_z, \quad x_{\beta} = x, y, z \quad (2-2)$$

where u_{α} is the displacement of lattice point under study along x_{β} .

Strain components can be specified also in other way as:

$$e_{xx} = \varepsilon_{xx}; \quad e_{yy} = \varepsilon_{yy}; \quad e_{zz} = \varepsilon_{zz} \quad (2-3)$$

which describes the infinitesimal distortions caused by a volume change. e_{xy} , e_{yz} , and e_{zx} are the other strain components that are specified in terms of angle changes between the basis vectors.

$$e_{xy} = \varepsilon_{xy} + \varepsilon_{yx} \quad (2-4)$$

$$e_{yz} = \varepsilon_{yz} + \varepsilon_{zy} \quad (2-5)$$

$$e_{zx} = \varepsilon_{zx} + \varepsilon_{xz} \quad (2-6)$$

2.4.2. Stress tensor

Externally imposed forces can cause crystal deformations; in other words, because a solid resists deformation, deformations will generate forces¹⁶. The force in reaction to strain in a unit area is known as stress. Stress is a second-order tensor with nine components and is

written as, $\tau_{\alpha\beta}$, $\alpha, \beta = x, y, z$. Figure 2.4 depicts the stress distribution on the surface of an infinitesimal volume cube, where τ_{xx} is a force applied in the x direction to a unit area of a plane whose outward-drawn normal is in the x direction, and τ_{xy} is a force applied in the x direction to a unit area of a plane whose outward-drawn normal is in the y direction.

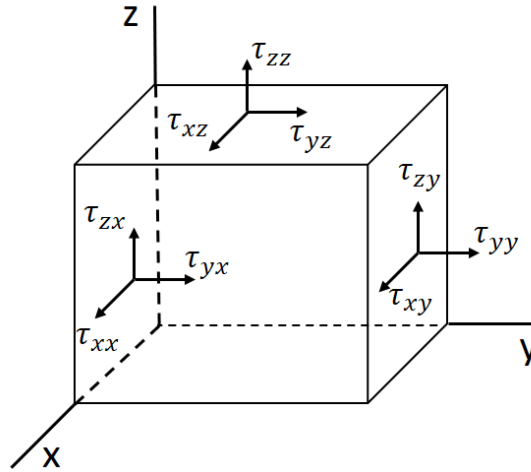


Figure 2.4. Illustration of an infinitesimal cube's surface stress components¹⁶. $\tau_{\alpha\beta}$ where $\alpha, \beta = x, y, z$ represents force applied in the α direction to the unit area of the plane whose outward-drawn normal lies in the β direction.

Based on the correlation between force and stress, we could resolve the force into components along the coordinate axes, i.e., F_{xx} , F_{yx} , and F_{zx} . The stress components in this plane are:

$$\tau_{xx} = \frac{F_{xx}}{A} \quad (2-7)$$

$$\tau_{yx} = \frac{F_{yx}}{A} \quad (2-8)$$

$$\tau_{zx} = \frac{F_{zx}}{A} \quad (2-9)$$

In the case of the uniaxial stress T along the $[100]$ direction (applied strain direction in our study), all stress components but τ_{xx} are zero, and $\tau_{xx} = T$.

$$\tau = \begin{pmatrix} T & 0 & 0 \\ 0 & 0 & 0 \\ 0 & 0 & 0 \end{pmatrix} \quad (2-10)$$

2.5. Structure of single crystal silicon surface

The basic structure of the most widely used single crystal surfaces is discussed in this section. Each Si atom is bonded to four others in a tetrahedral arrangement, giving the Si unit cell a diamond-like structure. This configuration corresponds to two interpenetrating Face-Centered Cubic (FCC) lattices, one of which is displaced from the other by $1/4$ of a lattice constant in each direction⁷⁸. Single crystal silicon substrates are used instead of polycrystalline substrates in the fabrication of microelectronic devices because they have a more uniform structure, making

their properties more consistent and predictable. In the semiconductor industry, the Si(100) and (111) orientations are the two most widely used structures. The miller indices for a cubic crystal structure are (100) and (111), respectively (Figure 2.5).

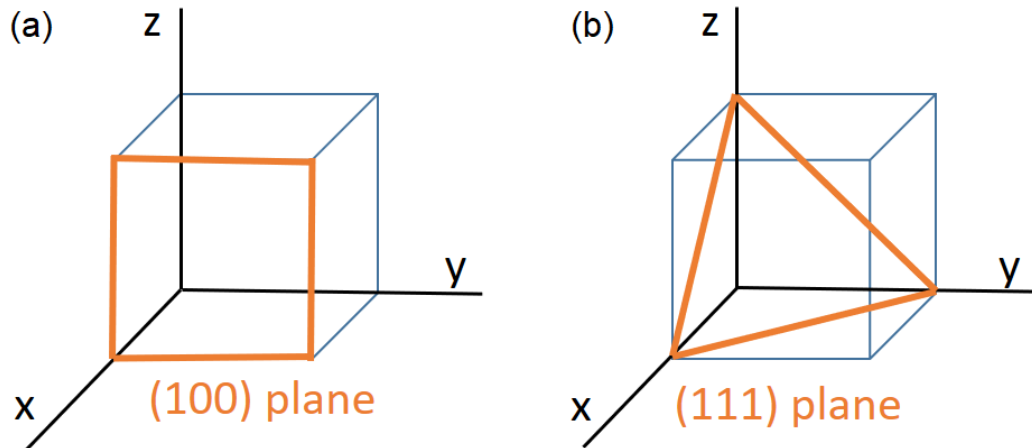


Figure 2.5. Crystal structure representing (a) (100) orientation (b) (111) orientation.

A substrate with a specific plane exposed is created by slicing single crystal silicon through a specific plane. Each of these planes is distinct due to differences in atom count and atom binding energies. Physical, chemical, and electrical properties vary as a result of these differences. Despite the fact that Si(100) is the orientation used in devices, Si(111) has gotten a lot of attention because it's easier to make smooth, defect-free H-terminated surfaces from which deeper insights into mechanisms can be gained.

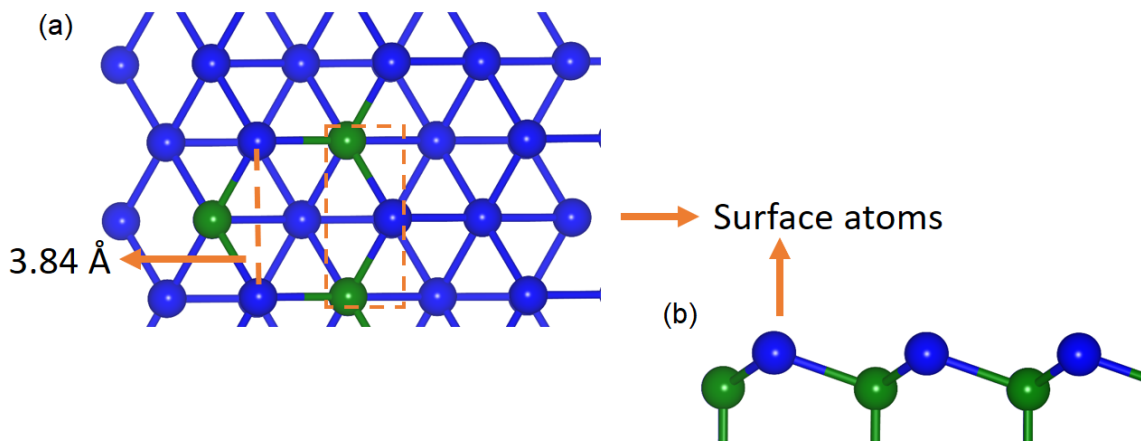


Figure 2.6. Structure of Si(111) (a) Top view, (b) Side view. The hexagonal symmetry of Si atoms is shown in top view image. Green and blue Si atoms are located under the surface and on the surface, respectively. The distance between Si atoms is 3.84 Å.

By comparing the positions of the silicon atoms in the structure, the epitaxial formation on a Si(111) substrate can be understood (Figure 2.6). The hexagonal symmetry is obvious: Si atoms can be located at the hexagons' vertices⁷⁹. Half of them (the green ones) are located just

under the surface. The other half (the blue ones) are on the surface with a dangling bond parallel to the Si(111) interface. The distance between these atoms is 3.84 \AA ⁷⁹. Surface reactivity is increased by the presence of dangling bonds, which can be reduced by surface reconstruction or capping these bonds with foreign atoms. The chemisorption of atomic hydrogen to the dangling bonds stabilizes the surface and prevents it from reacting further. As will be shown later, this is one of the key reasons for treating the silicon surface with hydrogen fluoride (HF).

2.5.1 Silicon surface preparation

The microelectronics industry's need for chemical etching of silicon oxide led to the invention of aqueous HF etching, a surprisingly simple process for producing stable surfaces in air. Although fluorine termination was once thought to be responsible for this stability⁸⁰, it was discovered more than two decades ago that HF-etched Si surfaces are H-terminated and contain no fluorine surface termination⁸¹. This conclusion was initially confusing because, as shown in Figure 2.7, Si-F is formed when the last oxygen of the oxide is removed, and the Si-F bond (5.0 eV) is 1.5 eV stronger than the Si-H bond. Because of the strong polarization of the Si-Si back bond caused by fluorine's high electronegativity, this Si-Si bond weakens, allowing the surface Si atom (to which F is attached) to be removed in the form of SiF_x (mainly SiF₄ and H₂SiF₆) molecules. This process causes the surface of microcrystalline Si to be terminated by hydrogen, as suggested by Ubara et al.⁸² and later verified by experiments⁸³ and ab-initio calculations⁸⁴. The H-terminated surface that results is less polar and therefore more resistant to HF chemical attack (i.e., there is no further etching in HF solution once the surface is H-terminated).

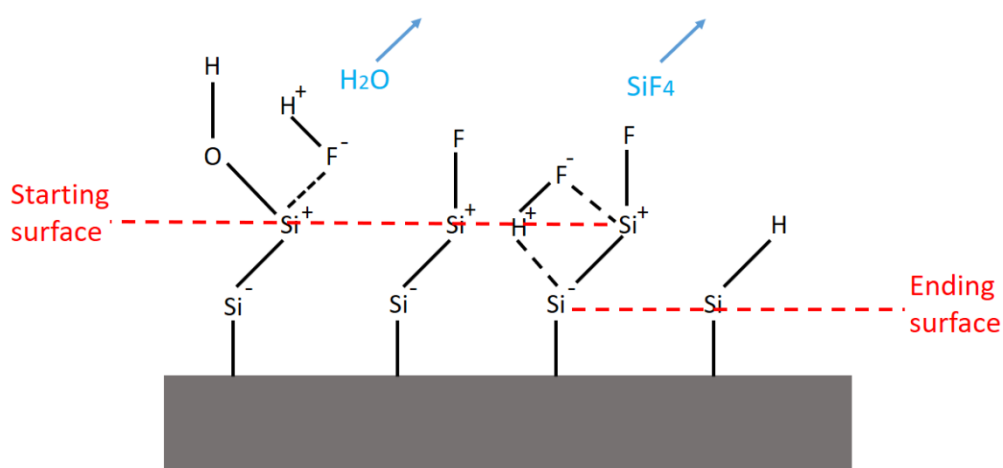


Figure 2.7. Mechanism leading to the formation of H-terminated Si surface by HF etching: The last step of oxygen removal from SiO₂ involves HF attack of the Si-O bond, with removal of OH as H₂O and termination of the surface Si atom with F. Further attack of the p-polarized Si^{δ-}-Si^{δ+} leads to H-termination⁸². Partially positive and negative charges of atoms are indicated as + and -, respectively.

2.6. Wetting

2.6.1. Surfaces and wetting

Wetting is the ability of a liquid to maintain contact with a solid surface, Resulting from intermolecular interactions when the two are brought together⁸⁵. For surface wettability characterization, the water contact angle (WCA) and contact angle hysteresis (CAH) are commonly used (Figure 2.8). The WCA is the angle formed by the intersection of the planes tangent to the solid-liquid and liquid-vapour surfaces. The contact line is the name given to this point of intersection.

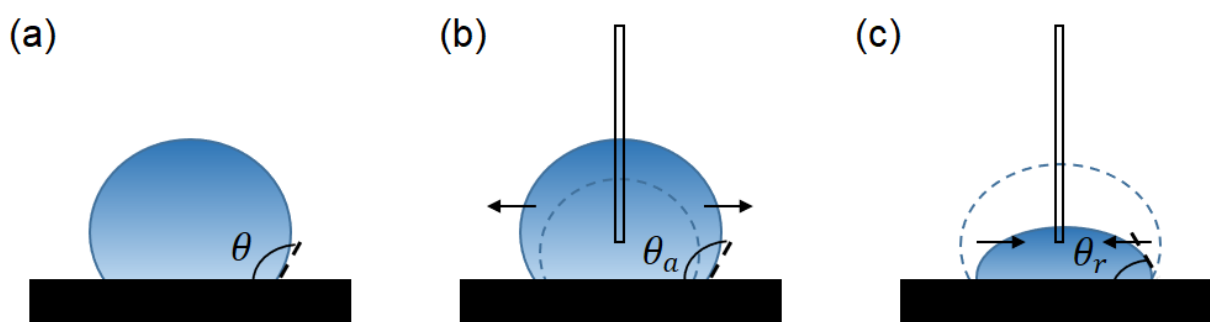


Figure 2.8. Water drop on a surface (a) with water contact angle θ , (b) advancing θ_a and (c) receding θ_r contact angles.

The contact line will not advance or recede until the contact angle reaches the crucial advancing or receding contact angle θ_a/θ_r after the addition or removal of some liquid from the droplet, or during droplet movement. Contact angle hysteresis is the difference between the approaching and receding contact (CAH)⁸⁵. Surface roughness, surface heterogeneity, and solution contaminants adsorbing on the surface are all common causes of CAH. A droplet must both advance (on the downhill side) and recede (on the uphill side) in order to move on a tilted surface (on the uphill side). As a result, the contact angle along with the static contact angle, hysteresis is a key parameter for determining the surface wettability⁸⁶. The principal approach for determining the surface hydrophobicity is to measure the contact angle. The sessile drop measurement, which involves placing a small drop of liquid on a surface, is the most common method. When the volume of the droplet increases and the wetting line begins to advance, the advancing contact angle is measured. If the drop volume is reduced after that, the receding contact angle is calculated at the moment when the wetting line is receding. Materials were previously classed as hydrophobic (static WCA $>90^\circ$) or hydrophilic (static WCA $<90^\circ$) until the words superhydrophobicity and later superhydrophilicity were introduced in 1996⁸⁷.

2.6.2. Theoretical model of surface wettability of flat surfaces

Young's equation, which was first published in 1805, is the fundamental equation of surface wetting⁸⁸. For the ideal solid surface at thermodynamic equilibrium, it relates contact angle to the specific energies of the solid-liquid, solid-gas, and liquid-gas interfaces:

$$\cos \theta = \frac{\gamma_{SV} - \gamma_{SL}}{\gamma_{LV}} \quad (2-11)$$

Where θ is static contact angle, and γ_{LV} , γ_{SL} and γ_{SV} are interfacial free energies of the liquid-vapour, solid-liquid, and solid-vapour interfaces, respectively. Because θ expresses inherent surface hydrophilicity or hydrophobicity, it is also known as intrinsic or Young's contact angle. Figure 2.9 represent the theoretical model of wetting for flat surfaces. Young's equation only works for surfaces that are flat and chemically homogeneous; for surfaces with different topological properties, additional models such as Wenzel or Cassie-Baxter are utilized. It is beyond the scope of this dissertation to explain these models.

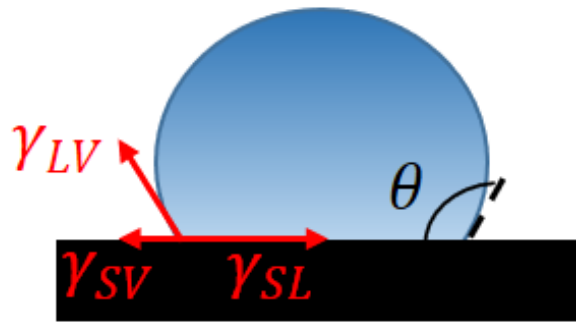


Figure 2.9. Young's model of surface wetting for flat surfaces; θ indicates static contact angle, and γ_{LV} , γ_{SL} and γ_{SV} are interfacial free energies of the liquid-vapour, solid-liquid, and solid-vapour interfaces, respectively.

2.7. Computational method

Density functional theory (DFT) is a quantum mechanical modeling method, useful in the fields of physics and chemistry for studying about the electronic structure of many-body systems, specifically, atoms, molecules, and the condensed phases. There isn't any available analytical and numerical solution of the many-electron Schrödinger equation. It's forcefully impossible in practice for more than a handful of electrons due to the finite speed and memory of computers; however, this issue is completely possible in theory. In this section, DFT will be introduced, a mean of circumventing the solution of the many-electron Schrödinger equation. Afterwards, we will mostly concentrate on Nudged elastic band (NEB) and Infrared spectroscopy (IR) calculations with DFT. In other words, these topics were our main concerns for theoretical part.

2.7.1. The Schrödinger equation

The Schrödinger's equation is a really fundamental equation in quantum mechanics⁸⁹. The solution of this equation is called wave function, the most complete description of any system. The general equation for one particle can be written as:

$$i\hbar \frac{\partial}{\partial t} \Psi(\mathbf{r}, t) = \widehat{H} \Psi(\mathbf{r}, t) = -\frac{\hbar^2}{2m} \nabla^2 \Psi(\mathbf{r}, t) + V(\mathbf{r})\Psi(\mathbf{r}, t) \quad (2-12)$$

where $\Psi(\mathbf{r}, t)$ is the wave function, \mathbf{r} is the position in three-dimensional space, \widehat{H} is the Hamiltonian operator, m is the mass and $V(\mathbf{r})$ is the potential at point \mathbf{r} . The time-independent

Schrödinger's equation can be written as:

$$E\Psi(\mathbf{r}) = -\frac{\hbar^2}{2m}\nabla^2\Psi(\mathbf{r}) + V(\mathbf{r})\Psi(\mathbf{r}), \quad (2-13)$$

which formulated the Schrödinger's equation as an eigenvalue problem.

Not so long after the validation of Schrödinger's equation for the electronic wave function for simple small systems like H₂ and many-electron atom He, so many were ready to bid farewell to the chemistry. The reason was, all that chemistry could provide, was included in the powerful equation. However, in most of the cases, the quantum mechanical equation is way too complicated to be solved exactly. As a result, finding proper approximation to Schrödinger's equation became an intuitive and straightforward solution. To state the truth, during the decades after Schrödinger's equation, the entire field of computational chemistry was built around approximate solutions. Some of these solutions are so crude and others are expected to be more accurate than any experiment that has been conducted. The knowledge of each approximation and how accurate the results, is expected to be the key to the choice of method. Extremely powerful computers, sometimes even supercomputers, are required for obtaining accurate results. In general, the larger the system (containing more particles) brings about more expensive computation.

2.7.2. Density Functional Theory

Density Functional Theory (DFT) method uses the electron density of a system, in order to provide us the ground states' properties. In 1960s, it was introduced for the first time by Hohenberg-Kohn⁹⁰ and Kohn-Sham in two seminar papers⁹⁰⁻⁹¹. Later, the theory has attracted a lot of research interest, in order to improve the adaption of this method, for practical and computation use. The last few decades, there has been an exponential increase of using prevailing applications of DFT method, especially after 90s. There are three important points in DFT development history: the first one, the rudimentary but inspirational form of DFT that was discussed in 1927 by Thomas and Fermi⁹², known as Thomas-Fermi theory. In 1964 and 1965, the Thomas-Fermi theory, known as Hohenberg-Kohn theory and Kohn-Sham equation, was asserted in two seminar papers. The roots of modern DFT are seen in the work of Pierre Hohenberg, Walter Kohn, and Lu Jeu Sham⁹³. Hohenberg and Kohn showed that we are able to define a universal functional for the complete electronic energy of an atom, molecule, or ion, $E_{\text{tot}}[n(\mathbf{r})]$, in terms of the electron density, $n(\mathbf{r})$ ⁹¹. They also stated that the whole electronic energy and other observable properties are a functional of $n(\mathbf{r})$. Additionally, they proved that putting the exact ground state electron density into this universal functional, yields the minimum global value of this energy functional. The work of Hohenberg and Kohn proved that the universal density functional must exist. However, their work neither prescribes the form for this functional, nor the way of describing electron density. The total electronic energy can be written as indicated in Eq. (2-14), where each term depended on the total electron density, $n(\mathbf{r})$. DFT turned into a practical computational tool, thanks to the equation developed by Kohn and Sham.

$$E_{tot} [n] = E_T [n] + E_V [n] + E_J [n] + E_X [n] + E_c [n] \quad (2-14)$$

where E_T is the total kinetic energy of the electrons, E_V is the total potential energy of the electrons due to their Coulombic attraction to the nuclear center(s), E_J is the total potential energy due to the average coulomb repulsion between pairs of electrons, E_X is the total quantum mechanical exchange energy of the electrons, and E_c is the total correlation energy of the electrons. The electron density can be represented using different several types of mathematical functions⁹⁴⁻⁹⁶. The original DFT calculations were performed using plane wave functions as basis sets. The infinite extent of these functions was an ideal option for computations on extended structures, such as metal surfaces or crystalline solids. For calculations related to discrete atoms and molecules, atom-centered-basis sets are generally more appropriate. For example, the electron density is represented by a single atom-centered function based on Gaussian, meaning $\chi_i(\mathbf{r})$. As a general rule, the optimization of the total electron density, $n(\mathbf{r})$, is accomplished by systematic variation of the linear expansion coefficients, c_i , in Eq. (2-15) for obtaining the lowest possible total energy:

$$n(\mathbf{r}) = \left(\sum_{i=1}^x (c_i \chi_i(\mathbf{r})) \right)^2 \quad (2-15)$$

2.7.3. FTIR calculation

Vibrational frequencies (most often reported in units of wavenumbers ($\tilde{\nu}$) in cm^{-1} , where $\tilde{\nu} = 1/\lambda$ and $\nu = c/\lambda$, and where ν is the frequency in Hertz, c is the speed of light in $\text{cm}\cdot\text{s}^{-1}$, and λ is the wavelength in cm) are related to the curvature of the potential energy versus interatomic distance function (i.e., the second derivative of potential energy as a function of atomic coordinates, $(\partial^2 E / \partial r^2)$, where E is the potential energy and r is the atomic coordinates)⁹⁷. The frequency is correlated with the bond strength, because stronger bonds require more energy to stretch. The relationship between potential energy and atomic coordinates in materials is called the potential energy surface (PES)⁹⁷. Quantum mechanical calculations can be used for predicting the most energetically-favorable position in atoms, and also the curvature of PES while atoms deviate from the minimum. This curvature or second derivation of PES provides an estimation of frequency either through analytic solution or numerical methods. Generally, the former is more accurate, but it can be impractical for larger model systems. Even the numerical solution can be impractical when the size of model system increases, as sometimes there's a necessity to calculate $3N$ energies (where N is the number of atoms) to obtain frequencies. A value of 6 is required because each atom must be displaced in both positive and negative x , y and z directions from the stable minimum energy. More points result in more accurate numerical approximation, but also more time-consuming. All are possible through at least one method, but like the case of frequency, analytical methods are more reliable compared to the numerical approximations. In general, intensity calculations are less accurate than frequency calculations because the former depend on properties such as the square of the dipole moment derivative rather than the latter that depends on the square-root of the second derivative of $(\partial^2 E / \partial r^2)$ the PES⁹⁸.

2.7.4. Locating Transition States

In this thesis, we utilized the Nudged Elastic Band (NEB) method⁹⁹, to seek the minimum energy pathway (MEP) and locate the saddle point of MEP. NEB method was developed by Hannes Jonsson et al.¹⁰⁰. The NEB is a method for determining the MEP between two stable states¹⁰¹. This pair has an initial and a final state in terms of reaction rates, both of which are local minima on the potential energy surface. The MEP has the property of having an energy minimum in all directions perpendicular to the path at any point on the path. At least one first-order saddle point is traversed on this path. The MEP is also known as the intersection of the steepest descending paths from saddle points to minima¹⁰².

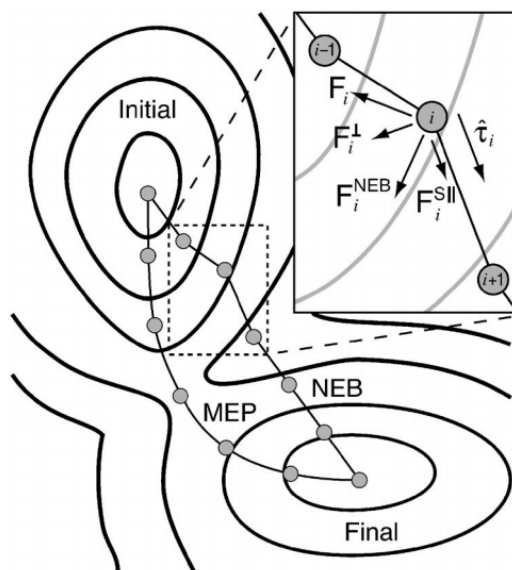


Figure 2.10. Two components make up the nudged elastic band force F_i^{NEB} : the spring force $F_i^{S||}$, along the tangent $\hat{\tau}_i$, and the perpendicular force due to the potential F_i^\perp . The unprojected force due to the potential F_i is also shown for completeness¹⁰².

The NEB is a chain-of-states method¹⁰³ in which a series of images representing the system's geometric configurations are utilized to illustrate a reaction pathway. Spring forces connect these configurations to provide equal spacing along the reaction path. The images describe the reaction process once the NEB and MEP have converged, up to the resolution of the images (see Figure 2.10). An initial pathway connecting the initial and final states is used to initiate a NEB calculation. A linear beginning path is usually sufficient, but in some circumstances, another option is preferable. Through a force projection scheme in which potential forces act perpendicular to the band and spring forces act along the band, the images along the NEB are relaxed to the MEP. The tangent along the path $\hat{\tau}$ is defined as the unit vector to the higher energy nearby image in order to make these projections⁹⁹. This up winding tangent increases the NEB's stability and prevents the formation of artificial bends at the path's high force zones. The NEB force on image i is made up of two separate components:

$$F_i^{NEB} = F_i^\perp + F_i^{S||} \quad (2-16)$$

Where F_i^\perp is the component of the force due to the potential perpendicular to the band, and F_i^{\parallel} is the spring force parallel to the band.

Within the harmonic transition state theory TST, the saddle point is particularly significant for characterizing the transition state. The climbing-image NEB (CI-NEB), which eliminates needing to do two separate optimizations or interpolate to get the saddle, is an efficient technique for finding a saddle between known states. The greatest energy image i experiences no spring forces and climbs to the saddle via a reflection of the force along the tangent in this way. Once the saddle has been located, the normal mode frequencies can be calculated to check that the saddle is first order and that the saddle is in the correct position. The NEB has been conveniently adapted as a connection with DFT calculation code VASP. I used the Perl code developed by Henkelman et al.⁹⁹ in my study.

Chapter 3

3. INSTRUMENTATION

This chapter describes the design, requirements, implementation and performance of our self-made mechanical devices. First, the machine which is built for combining with IR spectroscopy is described. This device is used to measure in-situ IR spectroscopy during the mechanical test of the samples (the results of using this set up widely will be explained in Chapter 6). The second mechanical system and its use in combination with a drop analyzer machine to measure in-situ contact angle measurement while bending is then addressed. The obtained results from this machine is investigated in Chapter 4. Lastly, important analytical method in this study (FTIR) is briefly explained.

3.1. Bending test

A bending test (also known as a bending tensile test) is a method of determining the bending strength and other critical properties of materials¹⁰⁴. Plastics, fiber-reinforced plastics (FRP), metals, and ceramic materials are all subjected to destructive materials testing. The series of bending tests is identical¹⁰⁴⁻¹⁰⁵. Standardized, often cylindrical specimens are mounted in the center of the checking fixture during bending tests. The rounded support rollers (bearings) are spaced apart and parallel to each other (support width). The cylindrical specimen's diameter is equal to the bearings' support width. The sample is loaded with increasing force by the test punch, which travels down slowly and at a steady speed, until it splits or approaches the previously defined deformation. The breaking force is the maximum load applied during the bending test¹⁰⁴. The bending force and deflection values are recorded during the test. After that, the material properties are determined. A stress-strain curve depicts the entire test series. This method is used to calculate the bending ability of brittle materials. In the case of an elastic deformation, the limit yield point, the greatest possible bending angle, and the Young's modulus are calculated when dealing with ductile materials¹⁰⁴. Figure 3.1 shows the image of common 3-point mechanical bending machine. As previously mentioned, we can only get some details about the mechanical properties of our sample from a typical mechanical system, which is insufficient for understanding how and why materials behave under mechanical force. As a result, in order to gather enough data to understand the fundamental reasons for the unique response of bent samples, we are developing new mechanical machines that can be combined with IR spectroscopy and a drop analyzer system. These new setups give us valuable information about how samples respond to external mechanical forces at the atomic level.



Figure 3.1. Bruker's 3-point-bend test setup on UMT Tribo laboratory. The image is taken from the 3-Point Bend Testing | Bruker.

3.2. New mechanical setup (called Bieger) for combing with IR spectroscopy

3.2.1. An introduction to the device and its performance

The Bieger is made up of a movable white sample holder (Figure 3.2(d), No. 1) that moves towards a nose-like metal piece (Figure 3.2(d), No. 3). The sample is placed inside the slot, which is located in sample holder (Figure 3.2(d), No. 2). The open current circuit connects the movable sample holder and the nose-like metal piece. The current circuit is closed and identified as zero position as soon as the sample comes into contact with the nose-like metal piece for the first time. It's worth noting that the stepper motor's complete rotation contains 51200 equivalent steps. Each step in the motor causes the spindle to rotate, meaning that the movable sample holder is moving downwards. The movable sample holder goes down as 0.75 mm after a complete rotation of the stepper motor. The software, written in LABVIEW, was used to set the number of steps and the value of deflections. We increase the steps in order after the sample reaches zero; for example, the spindle turns 200 steps, which equals a downward movement of 2,9 μm (the value of deflection). The FTIR calculation is then started in this location.

After performing the FTIR, the sample back to the zero position and the next FTIR test is performed. As a next position, the spindle is turned 400 steps, equal to 5.8 μm (the whole procedure is shown in Figure 3.2(c)). This process is repeated and stopped via a computer-based program controlling the movable sample holder movement.

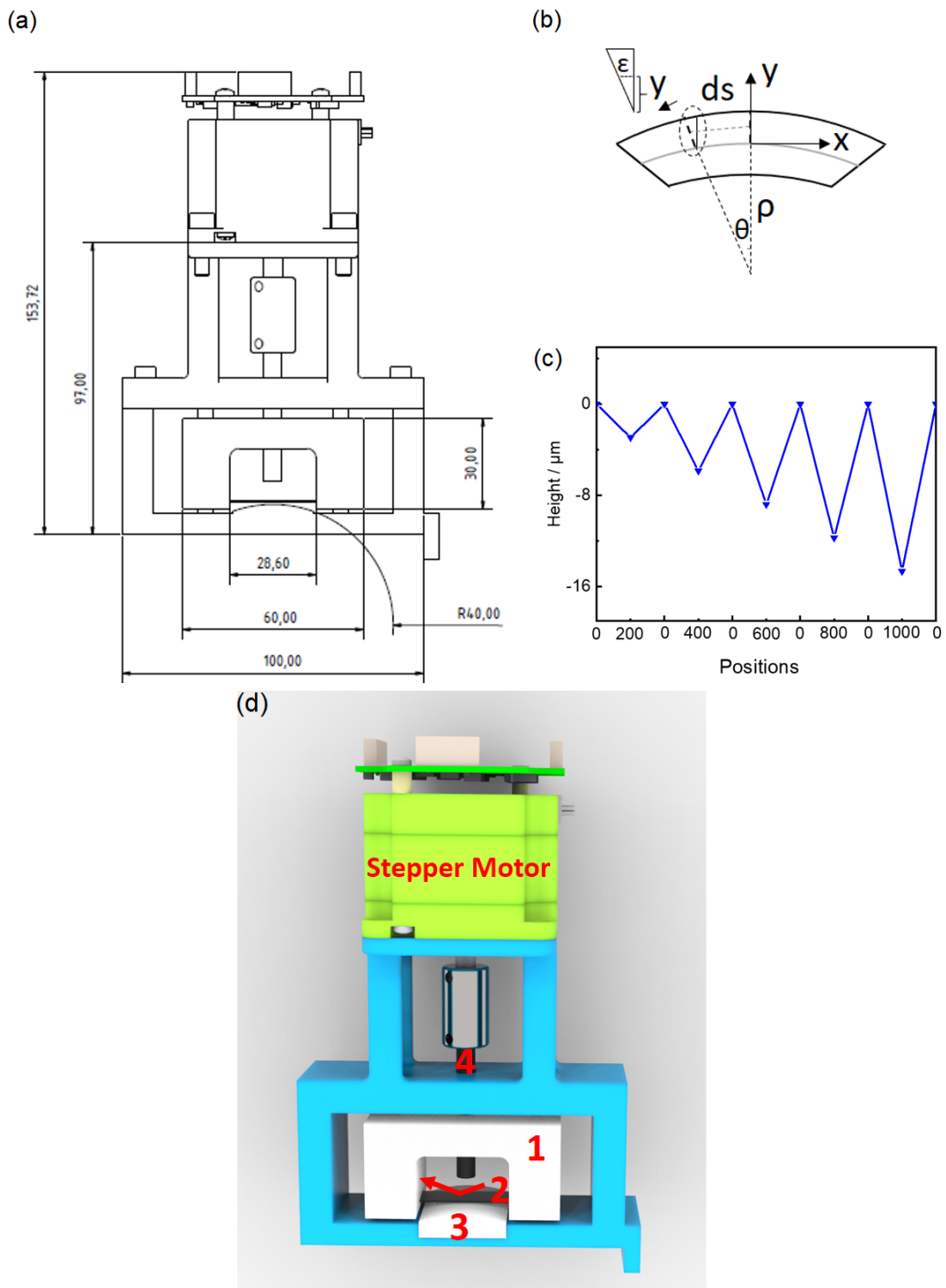


Figure 3.2. (a) Technical drawing of our self-made machine, (b) schematic illustration of the relation between the radius of curvature, ρ , wafer curvature and the strains within a wafer exposed to bending moments. (c) The graph shows the procedure of applying loading on the sample in different positions (the number of positions is equal to the number of spindle steps) and (d) the schematic illustration of the self-made instrument contain stepper motor, movable sample holder (1), sample (2), nose-like metal piece (3) and (4) spindle.

It's worth noting that the point of reflection (top of the sample's moment of inertia) remains constant during the bending process. To demonstrate this, we repeated the measurement with a deflection of 2,9 μm on samples with complete reflectivity, such as gold-coated Aluminum, several times; the results are shown in Figure 3.3. As a consequence, the obtained data show that changes in the IR spectra are caused by sample deformation.

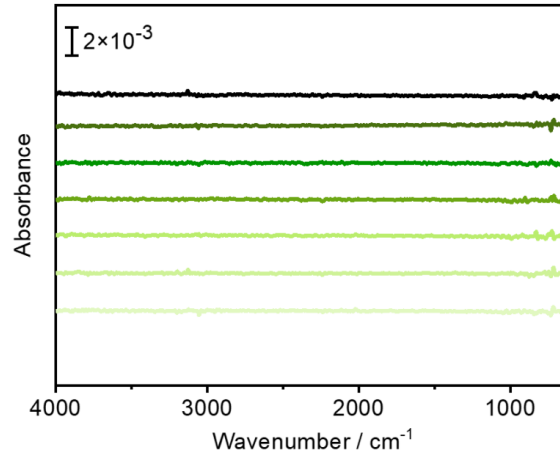


Figure 3.3. IR spectra of repeated measurements on gold-coated Aluminum which was bended equal to 2,9 μm in each step.

3.2.2. Calculation of strain, stress and force equations

The curvature is calculated in reference to the previous report from the following equation (3-1)

$$\rho = \frac{x^2}{8d} \quad (3-1)$$

where x is the sample length (30 mm) and d is deflection (μm) value in each position.

We use the Euler approximation to associate the bending moment with the deflection of the samples; ($\theta = \frac{\varepsilon}{y} = \frac{1}{\rho}$, $\rho d\theta = ds$, $\frac{dy}{dx} = \tan\theta$, Figure 3.2 (b)). And as a result, the below formula is acquired in order to force, stress and strain calculation.

$$\frac{\varepsilon}{d} = \frac{1}{\rho} = \frac{Fx}{2EI} \quad \text{Moment of inertia : } I = \frac{bh^3}{12} \quad (3-2)$$

So the strain formula is as

$$\varepsilon = \frac{6Fxd}{Ebh^3} \quad (3-3)$$

And at the end in order to stress calculation according to ($\sigma = E\varepsilon$),

$$\sigma = \frac{6Fxd}{bh^3} \quad (3-4)$$

where E is Young's modulus of Si (165 = GPa)¹⁰⁶, ρ the radius of curvature in each position (mm), F applied force (GPa mm²), d deflection (μm) and ε strain. I is called the moment of inertia ($I = \frac{bh^3}{12}$, where b and h are width and thickness of the sample, respectively).

3.3. New mechanical machine to combine with drop shape analyzer device

Every project included in this dissertation has been done with the aim of monitoring atomic-scale changes induced by strain. The effect of strain on surface reactivity was one of our key concerns in the thesis, as discussed in **Chapter 1** (general remarks). Contact angle measurements are often used to assess the effects of surface treatments produced as part of basic surface science research as well as for industrial applications. As a result, the effect of strain on chemical reactivity on a surface is investigated using in-situ contact angle measurement in combination with the system shown in Figure 3.4 as a second technique. The equations above are used to calculate the values of curvature, strain, stress, and force. The strain application process as well as the relationship between stepper motor rotations and spindle movement, are similar to the first setup (explained in section 3.2.1).

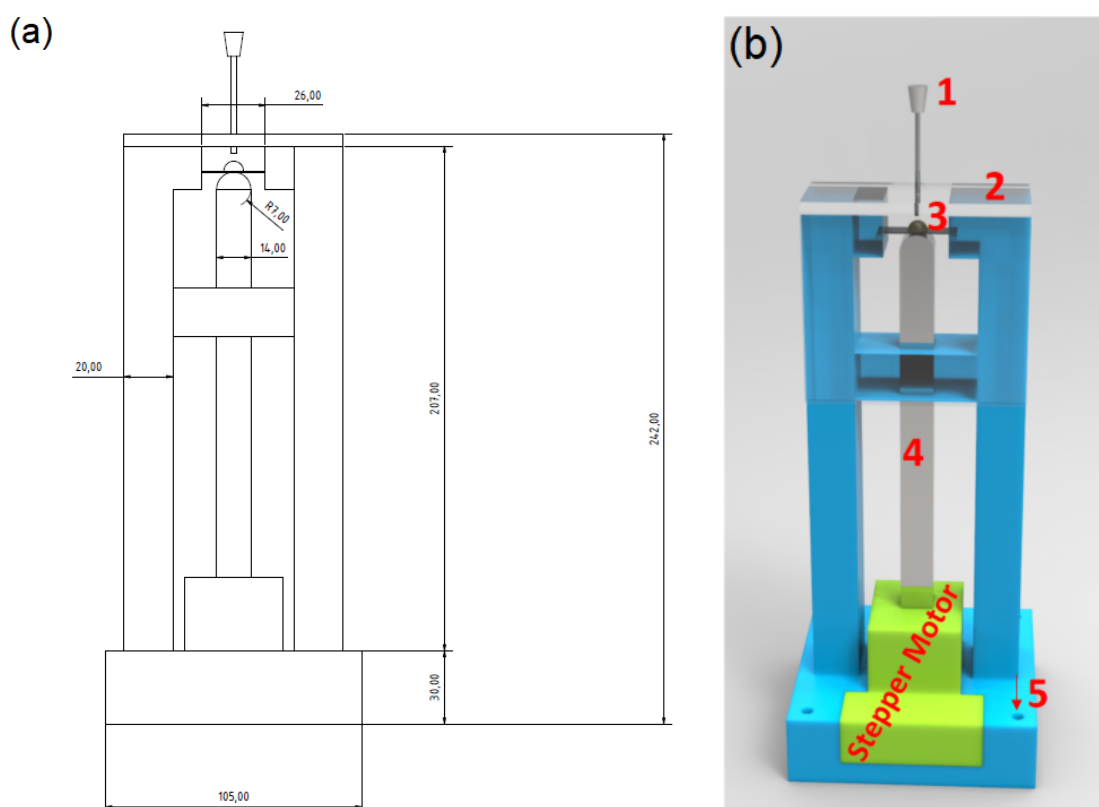


Figure 3.4. (a) Technical drawing of our second self-made bending device. (b) The schematic illustration of our self-made mechanical device for measuring in-situ contact angle while bending. Different parts of this machine are shown; needle (1), the white box which is filled by N_2 gas to keep the sample from the environment (2), sample (3), spindle (4), empty place to screw the mechanical machine with Shape-Analyzer-DSA100E device (5) and stepper motor (green part).

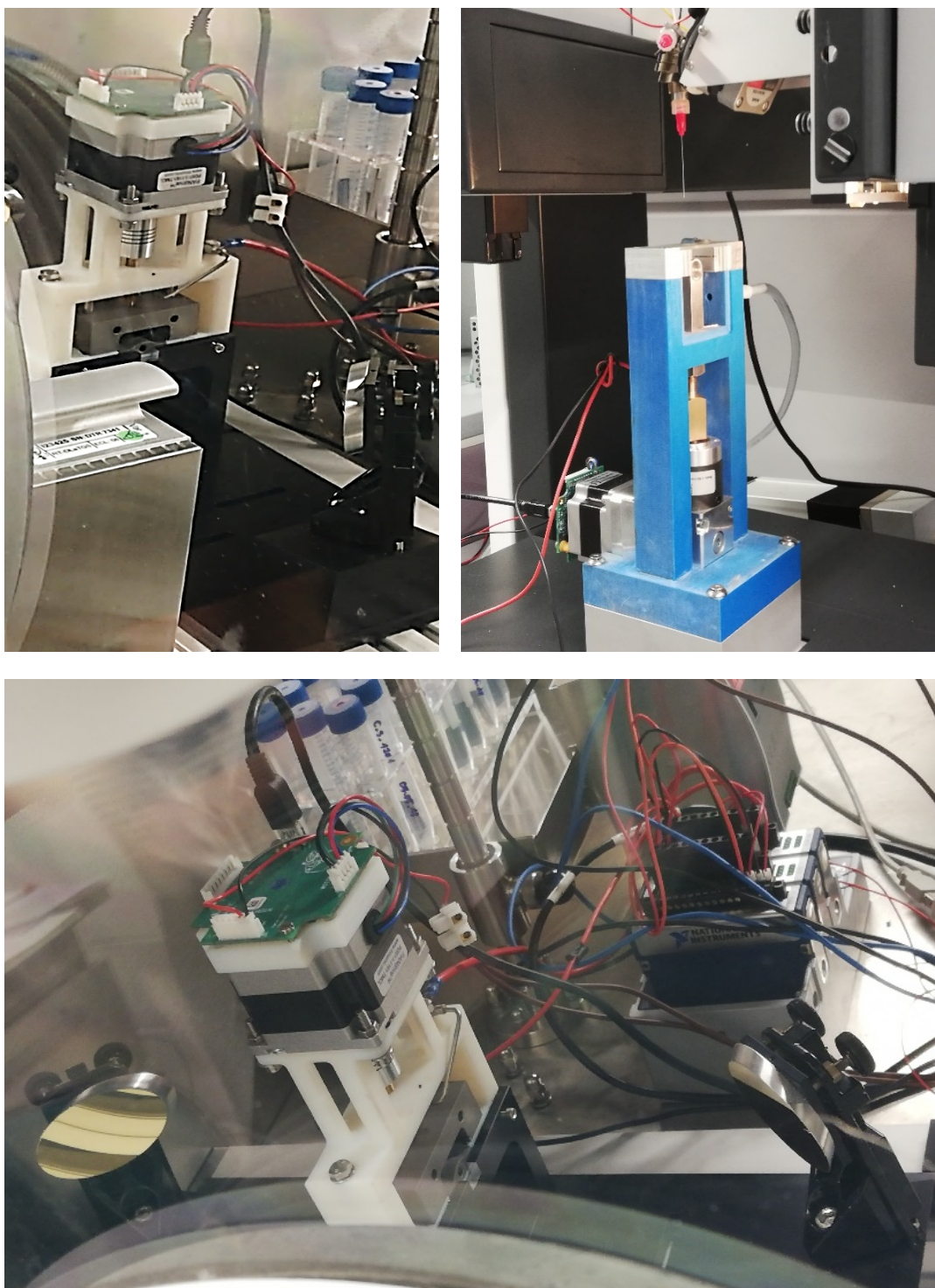


Figure 3.5. The actual images of our self-made mechanical devices; (up) the image of first device which was placed into glovebox for in-situ IR measurement, and (down) the picture of second device which was combined with drop shape analyzer machine.

3.4. Analytical method

3.4.1. Fourier Transform Infrared Spectroscopy (FTIR)

3.4.1.1. Basic principle

Infrared (IR) spectroscopy is the most popular spectroscopic technique used by organic and inorganic chemists¹⁰⁷⁻¹⁰⁸. It is concerned with radiation absorption in the infrared range of the electromagnetic spectrum. Since a molecule's vibrational and rotational energy levels change as it absorbs infrared radiation, IR spectroscopy is also known as vibrational-rotational spectroscopy. The near-infrared, mid-infrared, and far-infrared regions of the electromagnetic spectrum are normally classified into three categories based on their relationship to the visible spectrum (Figure 3.6). The higher energy near-IR, approximately $14000\text{-}4000\text{ cm}^{-1}$ ($0.8\text{-}2.5\text{ }\mu\text{m}$ wavelength) can excite overtone or harmonic vibrations. The fundamental vibrations and related rotational-vibrational structure can be studied using the mid-infrared wavelengths of $4000\text{-}400\text{ cm}^{-1}$ ($2.5\text{-}25\text{ }\mu\text{m}$). The far-infrared, which lies adjacent to the microwave region and has a wavelength range of $400\text{-}10\text{ cm}^{-1}$ ($25\text{-}1000\text{ }\mu\text{m}$), has low energy and can be used for rotational spectroscopy¹⁰⁸⁻¹⁰⁹. The fact that molecules absorb unique frequencies that are characteristic of their structure is exploited by infrared spectroscopy. These absorptions have resonant frequencies, which means that the frequency of the absorbed radiation is the same as the frequency of the vibrating bond or group. The shapes of the molecular potential energy surfaces, the masses of the atoms, and the resulting vibronic coupling define the energies. A vibrational mode in a molecule must be correlated with changes in the permanent dipole in order to be "IR active". A molecule can vibrate in a variety of ways, each of which is referred to as a vibrational mode. Nonlinear molecules have $3N-6$ degrees of vibrational modes, whereas linear molecules have $3N-5$ degrees (also called vibrational degrees of freedom). The non-linear molecule H_2O , for example, has $3\times 3-6=3$ degrees of vibrational freedom, or modes.

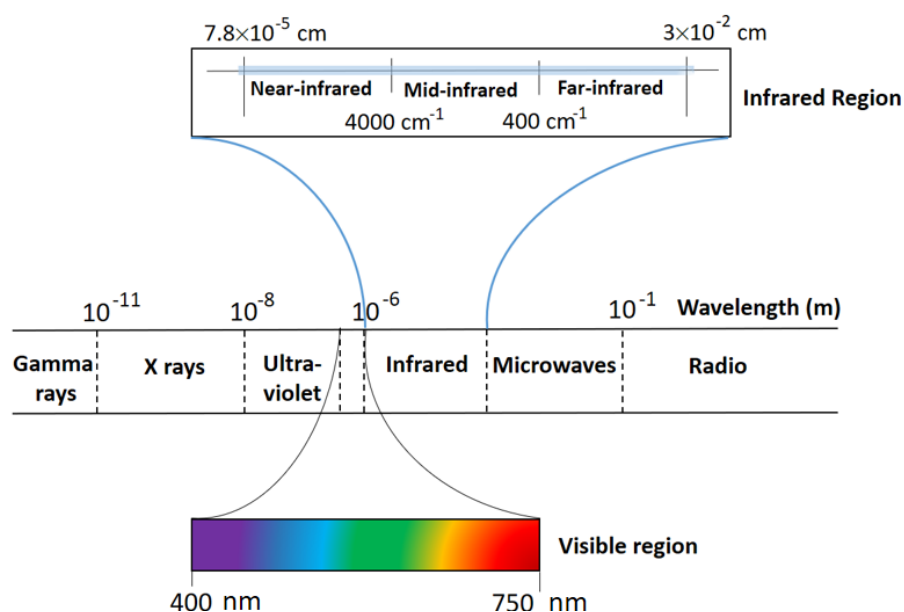


Figure 3.6. Electromagnetic spectrum. Infrared regions are separated into three regions: (1) Near-infrared ($12820\text{-}4000\text{ cm}^{-1}$); Mid-infrared ($4000\text{-}400\text{ cm}^{-1}$) and Far-infrared ($400\text{-}33\text{ cm}^{-1}$)¹¹⁰⁻¹¹¹.

3.4.2. Instrumentation

An optical instrument known as an interferometer is at the heart of any FTIR¹⁰⁸. FTIR manufacturers employ a variety of interferometer designs. The Michelson interferometer is the oldest and probably the most popular form of interferometer in use today. It was named after Albert Abraham Michelson (1852–1931), who invented the interferometer in the 1880s and won the Nobel Prize in Physics for his discoveries¹⁰⁸. Figure 3.7 depicts the optical configuration of a Michelson interferometer. Four arms make up the Michelson interferometer. The infrared source is located in the top arm of Figure 3.7, along with a collimating mirror that collects the light from the source and aligns its rays. The Michelson interferometer's bottom arm includes a fixed mirror, which is a mirror that does not move and is in a fixed position.

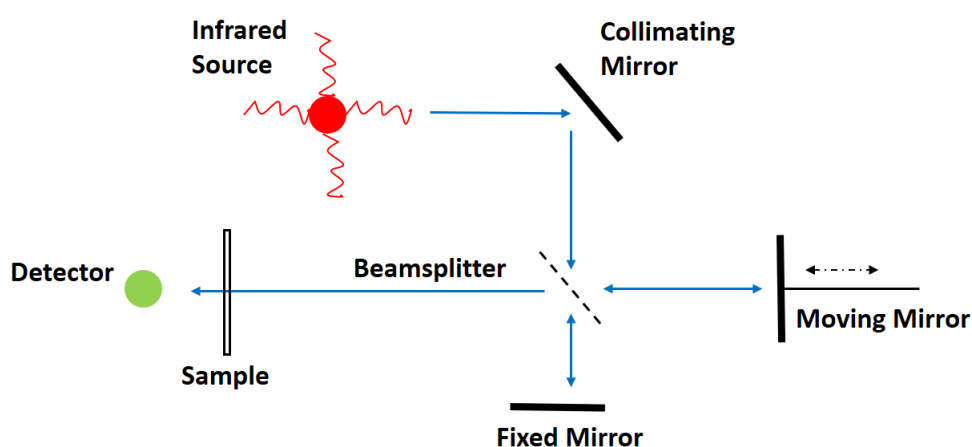


Figure 3.7. The optical diagram of a Michelson interferometer¹⁰⁸. The Michelson interferometer has four arms. The infrared source, as well as a collimating mirror that collects the light from the source and aligns its rays, are housed in the upper arm. A fixed mirror is a mirror that does not move and is in a fixed position in the Michelson interferometer's bottom arm.

This is in contrast to the interferometer's right arm, which incorporates a moving mirror that can move left and right. The sample and detector are located in the interferometer's left arm. An optical instrument known as a beamsplitter is at the center of the interferometer¹⁰⁸. A beamsplitter is a device that is designed to transmit some of the light it receives while also reflecting some of it. The light emitted by the beamsplitter is directed toward the fixed mirror in Figure 3.7, while the light reflected by the beamsplitter is directed toward the moving mirror. The light beams return to the beamsplitter after reflecting from these mirrors, where they are recombined into a single light beam that exits the interferometer, interacts with the sample, and strikes the detector. The mirror displacement in an interferometer is denoted by the Greek letter capital delta (Δ) and is the distance the mirror travels in the interferometer. Mirror translation of Δ gives an optical path difference of 2Δ because the light traverses the displaced distance twice on the way to and from the moving mirror.

$$\delta = 2\Delta \quad (3-5)$$

Where, δ is optical path difference and Δ is mirror displacement.

The intensity of the beam leaving the interferometer has changed dramatically by shifting the mirror a fraction of a wavelength. When the two beams are a whole number of cycles out of phase, constructive interference occurs. Conversely, the destructive interference occurs when the two beams are some number of cycles plus a half out of phase with each other. Thus, we can write for destructive interference that:

$$\delta = (n + \frac{1}{2})\lambda \quad (3-6)$$

Where, δ is optical path difference, λ is wavelength and $n = 0, 1, 2, \dots$ (any integer).

Since the fixed and moving mirror beams are in phase and positive interference occurs at zero path difference, the intensity is high. As we move the mirror away from the beam splitter, the beams become increasingly out of phase, and the resulting beam dims due to destructive interference. A plot of light intensity versus optical path difference is called an interferogram (Figure 3.8), which means “interference writing”. The fundamental measurement obtained by an FTIR is an interferogram. The interferograms obtained during scanning are Fourier transformed to produce a spectrum, hence the name Fourier Transform Infrared (FTIR) spectroscopy.

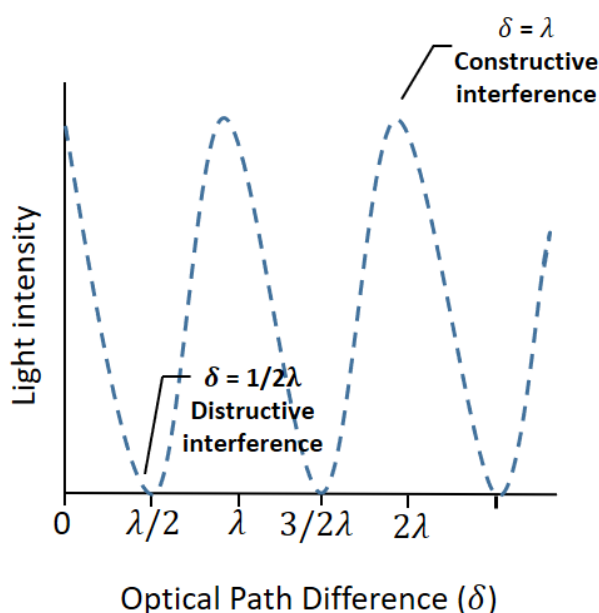


Figure 3.8. A plot of light intensity (or detector signal) versus optical path difference for a mirror moving away from the beamsplitter in a Michelson interferometer. Such a plot is called an interferogram. This is the interferogram for a single wavelength of light passing through the interferometer¹⁰⁸.

Chapter 4

4. STRAIN EFFECT ON THE OXIDATION OF HYDROGEN TERMINATED SILICON (111)

The concept of this study were adapted from the published article: "Strain Activation of Surface Chemistry on H-terminated Si(111)" with permission from Journal of Physical Chemistry C.

4.1. Surface reactivity of hydrogen terminated Si(111)

Since the Si/SiO₂ interface is virtually defect-free, integrated-circuits technology is possible^{18, 112-113}. As a consequence, one of the most significant chemical reactions is silicon oxidation. Its perfection also allows for a better understanding of the fundamentals of other surface processes. As a result, numerous experimental and theoretical instruments, such as IR spectroscopy¹¹⁴, x-ray absorption spectroscopy¹¹⁵, Auger electron spectroscopy¹¹⁶, and spectroscopic ellipsometry¹¹⁷, have been used to investigate it extensively. Si oxidation has also been studied using second-harmonic generation (SHG)²⁰. The evolution of resonances in SHG spectra of 111-oriented surfaces was studied by Daum et al.²⁰, who demonstrated that suboxides form during oxidation. SHG was found to provide details about chemical changes in the Si(111) surface along various bond directions, with n-type doping changing the chemical kinetics of up and back bonds differently during oxidation¹⁹. It was discovered, for example, that macroscopic tensile strain increases the reactivity of strained bonds at the same interface as compared to unstrained bonds¹¹⁸. However, the impact of strain on chemical reactivity at the bond level is still unknown. Several questions remain unanswered, including the rate of reactivity of the Si-H group by strain, modifying the composition of intermediates or the number of elementary reaction steps by strain and oxidation of H-Si(111) in a desired orientation by strain. In this work, the focus was on initial step of oxidation via monitoring the Si-H stretch vibration on flat H-Si(111). Automatic smooth H-Si(111) surfaces were used due to their simplicity, yielding atomically smooth terraces with a homogeneous array of identical Si-H bonds oriented normal to the surfaces. In principle, this surface only contains one reactant, reducing the number of potential reaction products. Second, water is very important. The majority of inorganic materials absorb water from the air. Adsorbed water has an effect on biology, material science, and tribology. Water's unique properties in the liquid state stem from its large dipole moment, high polarizability, and hydrogen bonding ability. As a result, both experimentally and theoretically, the strain effect (at the atomic scale) on the surface reactivity of H-Si(111) surface was verified in this research.

4.2. Methodology

Sample preparation: Pieces of p-type (CZ, resistivity of 0.1-1 Ω cm) Si(111) wafers, polished on both sides were prepared in 10 mm \times 30 mm \times 0.5 mm dimensions for mechanical measurements. In order to eliminate organic contaminations, samples were degreased in

acetone followed by cleaning procedure by 30 min exposure to an 80°C solution of 3:1 H₂SO₄ 90%/H₂O₂ (aq). Hydrogen terminated was performed on the samples in the order of 30 s dip in 10-20% HF (aq), a 2.5 min dip in 40% NH₄F (aq), and a final rinse in H₂O for 10s. This experiment has three parts: (I) strain effect on H-Si(111) microstructure, (II) surface reactivity of unstrained H-Si(111) towards liquid water, and (III) study the reactivity of strained H-Si(111) towards liquid water. The silicon wafer (Si(111)) is cleaned with piranha solution and placed in a N₂-purged glovebox before each experiment. After cleaning the sample, the IR spectrum was taken. Spectra with a nominal 4 cm⁻¹ resolutions were recorded (spectra from 400 to 4000cm⁻¹, transmission mode) using Fourier transform infrared (FTIR) spectrometer (VERTEX 70In). A room temperature pyroelectric detector (DTGS) was used for data collection. Furthermore, following the preparation of H-Si(111), all experiments (mechanical testing and IR measurement) on samples are carried out inside a glovebox. For stage (I), after preparation of H-Si(111), the IR spectrum of the sample is measured. The sample's side that was exposed to the IR beam is marked. After the IR measurement, the sample is placed inside the sample holder (the marked side top). Zero position is defined and the number of steps is set 400 steps. The spindle turns and the sample holder moves down 5.8 μm and the sample is kept under stress for 10 min. Subsequently, the curvature is removed, sample is taken out and the second IR spectrum in transmission mode is measured. As the next step, after completing the IR measurement, again the sample is placed inside the sample holder, goes to zero position. This time, the spindle turns 5000 steps which is corresponded to the straining sample at 0.1 %. After 10 min of remaining under stress, the bent specimen is removed and the third IR spectrum is measured afterward. This procedure continues until reaching the strain value of 1.0 %. All absorbance spectra are processed by subtracting IR spectrum of sample after piranha cleaning and then by flattening the baseline to remove drifts. OPUS software was used to integrate the peak areas, and, when appropriate, peaks were fitted using Origin software. Flow diagram of steps and procedure of this experiment is shown in Figure 4.1.

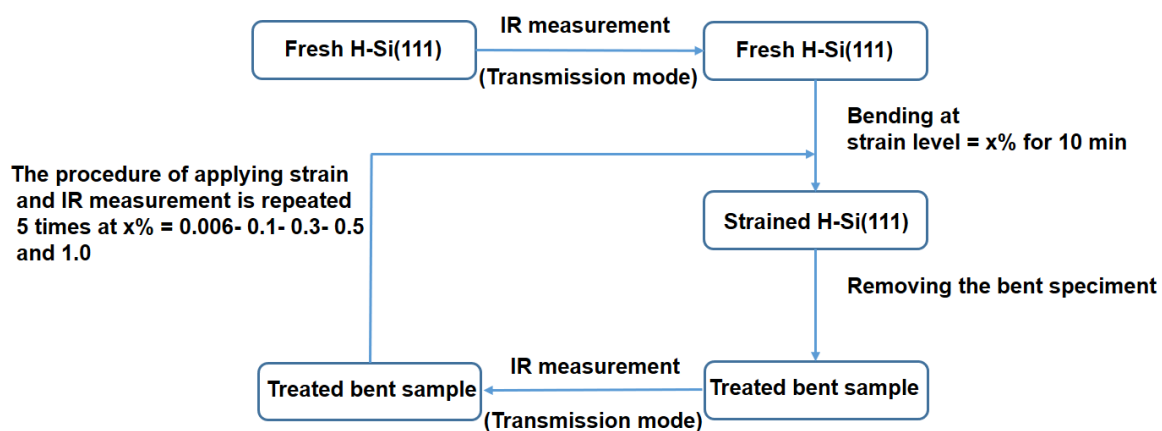


Figure 4.1. Flow diagram of applying strain and measuring IR spectra of hydrogen terminated silicon(111).

At stage (II), the first IR spectrum of fresh H-Si(111) is measured and the side of the sample

which has been in front of the IR beam is marked. Next, using the calibrated micropipette (10-100 μL / eppendort), 10 μL deionized water (resistivity 18.2 $\text{M}\Omega\text{ cm}$) is placed at the center of the sample (on the marked side). After 0.5 min of reaction time, the sample is completely dried using N_2 gas, and the second IR spectrum is measured. Following the IR measurement, the same volume of water is placed on the sample again. The sample is dried after 2 min of reaction time and third IR spectrum is taken. The same procedure is repeated for the reaction times of 5, 10 and 20 min as well. Figure 4.2 represent the procedure of experiment.

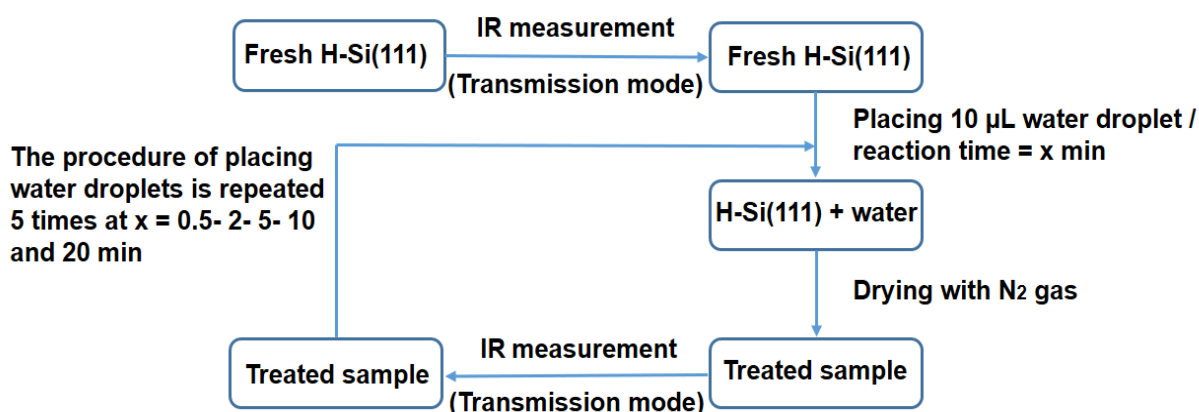


Figure 4.2. Flow diagram of procedure to study the reactivity of unstrained hydrogen terminated silicon toward liquid water at different reaction times of 0.5- 2- 5- 10 and 20 minute.

Step (III) is completed by keeping the strain value constant at 0.3 percent and running the experiment at various reaction times. Fresh H-Si(111) has its IR spectrum measured, and the side of the sample in front of the IR beam is marked. The sample is placed in the machine (marked side up). First, it reaches zero and, using a calibrated micropipette (10-100 μL / eppendort), 10 μL deionized water (resistivity 18.2 $\text{M}\Omega\text{ cm}$) from the same container stored in the glovebox for the experiment (II) is pipetted into the sample's center (on the marked side). Following a 123 μm downward movement of the sample holder (strain level = 0.3 percent), it is bent. The bent sample is removed after 0.5 minutes of reaction time and fully dried with N_2 gas. In transmission mode, the second IR measurement is taken. Following the IR calculation, the sample is put in the system and reset to zero. The same volume of deionized water is placed on the center of the sample and strained by applying 0.3% strain. The curvature is removed after 2 minutes of reaction time, and the sample is dried and ready for IR measurement. By varying the reaction time of bent H-Si(111) towards liquid water, this process is repeated five times. The procedure of experiment is shown in Figure 4.3.

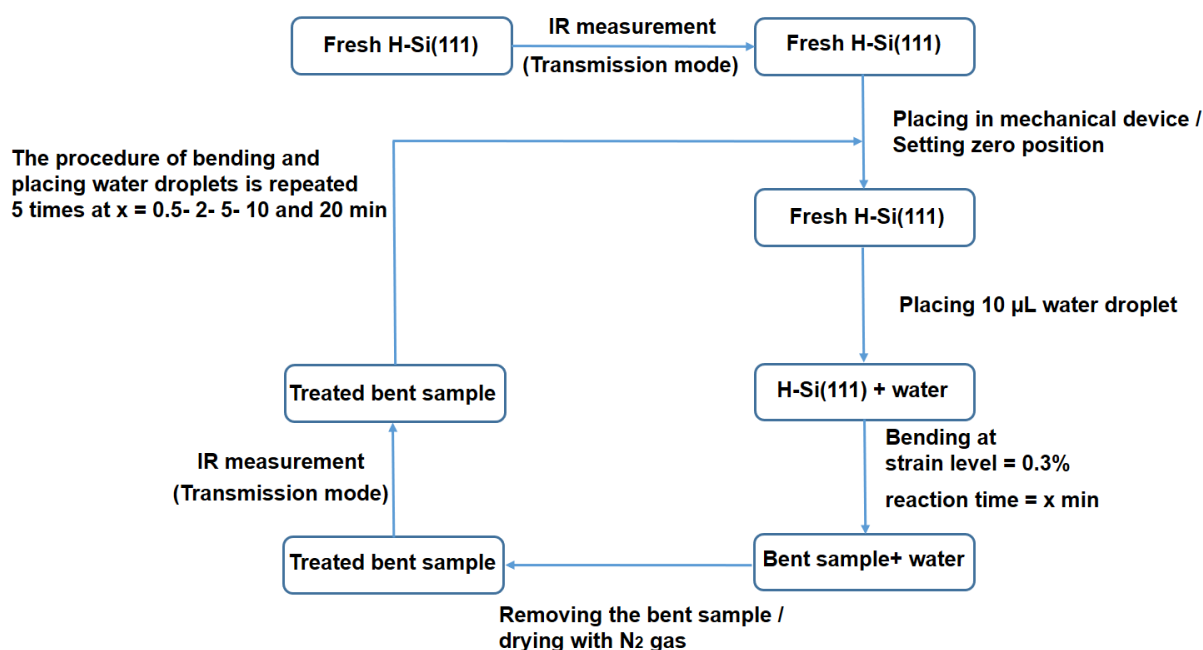


Figure 4.3. Flow diagram of procedure to study the reactivity of strained hydrogen terminated silicon (strain level = 0.3%) toward liquid water at different reaction times of 0.5- 2- 5- 10 and 20 minute.

The applied values of deflection, strain, and force to get the strain in the range of 0.006-1% are presented in Table 4.1.

Table 4.1. Calculated values of deflection, force and strain corresponding to number of steps.

Number of steps	Deflection / μm	Force / GPa mm^2	Strain
400	5.8	4.475E-24	0.006
5000	73	5.594E-23	0.1
8400	123	9.399E-23	0.3
10800	158	1.208E-22	0.5
15400	225	1.723E-22	1.0

Computational Details: DFT calculations were performed as implemented in the Vienna ab initio simulation package (VASP)¹¹⁹⁻¹²⁰ using the Perdew-Burke-Ernzerhof (PBE) generalized gradient approximation exchange-correlation functional¹²¹. The electron-ion interaction is described by the projector augmented wave (PAW) method¹²² with an energy cutoff of 360 eV. A super cell with 72 (Si: 54 and H: 18) atoms was completely relaxed for all of the samples studied, with geometry optimization using the conjugate gradient method. Periodic boundary conditions were applied in all directions. The Brillouin zone was sampled using a $4 \times 4 \times 1$ k-point mesh size with the Monkhorst-Pack mesh¹²³. Uniaxial loading conditions were applied after the optimized structure was obtained. To apply strain using the uniaxial tensile simulations, we elongated the periodic simulation box size along the loading direction [100] in one step with small engineering strain of

0.3%. Strain value is imposed due to the values obtained from experimental parts (strain range 0.006%-1.0%). The applied elongation, ΔL , can be obtained based on the initial length of the unstrained sample along the loading direction, L_0 , and the loading engineering strain which is equivalent to $\Delta L/L_0$. The simulation box size in the perpendicular direction of the loading was then adjusted accordingly to ensure uniaxial stress condition in the study, so that stress remained negligible in the perpendicular direction¹²⁴. After applying the loading conditions, structural relaxation was achieved using the conjugate gradient energy minimization method with 10–6eV criteria for energy convergence. To calculate IR spectra, the IBIRON = 8 is set to determine the Hessian matrix (matrix of second derivatives). Kinetic barriers were calculated by the nudged elastic band (NEB) method, using a string of geometric configurations to describe the reaction pathway of the system. A spring interaction between every configuration ensured continuity of the reaction pathway.

4.3. Strain effect on hydrogen terminated Si(111) / experiment (I)

Figure 4.4 demonstrated the IR spectra of H-Si(111) after mechanical test of the sample. Presence of Si-H stretching peak (2083.3 cm^{-1}) at the surface is confirmed by Si-H stretching vibration region^{21, 125}. The dark blue curve (Ref) shows the IR spectrum of fresh H-Si(111) before bending. The peak intensity of stretching Si-H mode is decreased by $54.2\pm 2\%$ following exposure of strain of 0.006% for 10 min. After strain enhancement to 0.3%, the intensity of Si-H peak reaches a value that is $64.2\pm 1.2\%$ less than that of the unstrained sample (dark blue curve). At higher strain, the decreasing trend becomes slower and at the 1.0% strain, the intensity decreases substantially to about 1/3 of the initial intensity. Deconvolution of absorbance bands into an elementary contribution is carried out using Origin software. The spectra are fitted by Lorentz profile and the data for the best fit are presented in *Appendix A*.

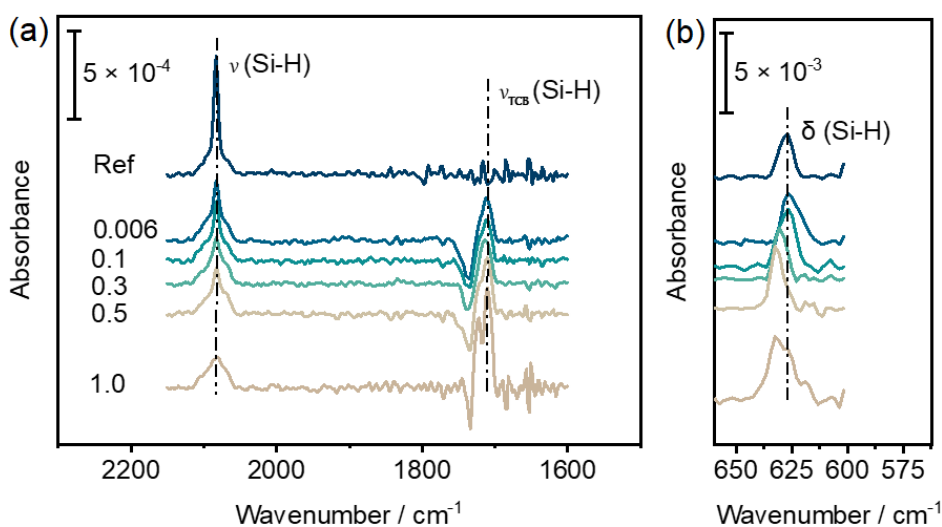


Figure 4.4. FTIR spectra of H-Si(111) surface subjected to different strain levels (percent). The dark blue spectrum (Ref) is corresponding to unstrained sample (fresh H-Si(111)). Spectrum of sample (silicon(111)) after piranha cleaning is used as background for all of the presented spectra.

Following strain enhancement, a decrease in the intensity of stretching Si-H mode (at 2083.3 cm^{-1}) possibly means a decrease of the total bonded hydrogen (Figure 4.5a). However, increasing the strain causes the amplitude of the band at 626.40 cm^{-1} to fluctuate in peak intensity (Figure 4.5c). Altogether it is suggested that redistribution of the bonded hydrogen in the silicon network is happened during the bending rather than decreasing in the hydrogen content¹²⁶.

Furthermore, strained samples develop a band at $\sim 1712\text{ cm}^{-1}$ which becomes sharper upon strain elevation (Figure 4.5a, 4.5b). There is no peak of IR spectrum (Figure 4.5a) at 1712 cm^{-1} for unstrained sample (dark blue curve).

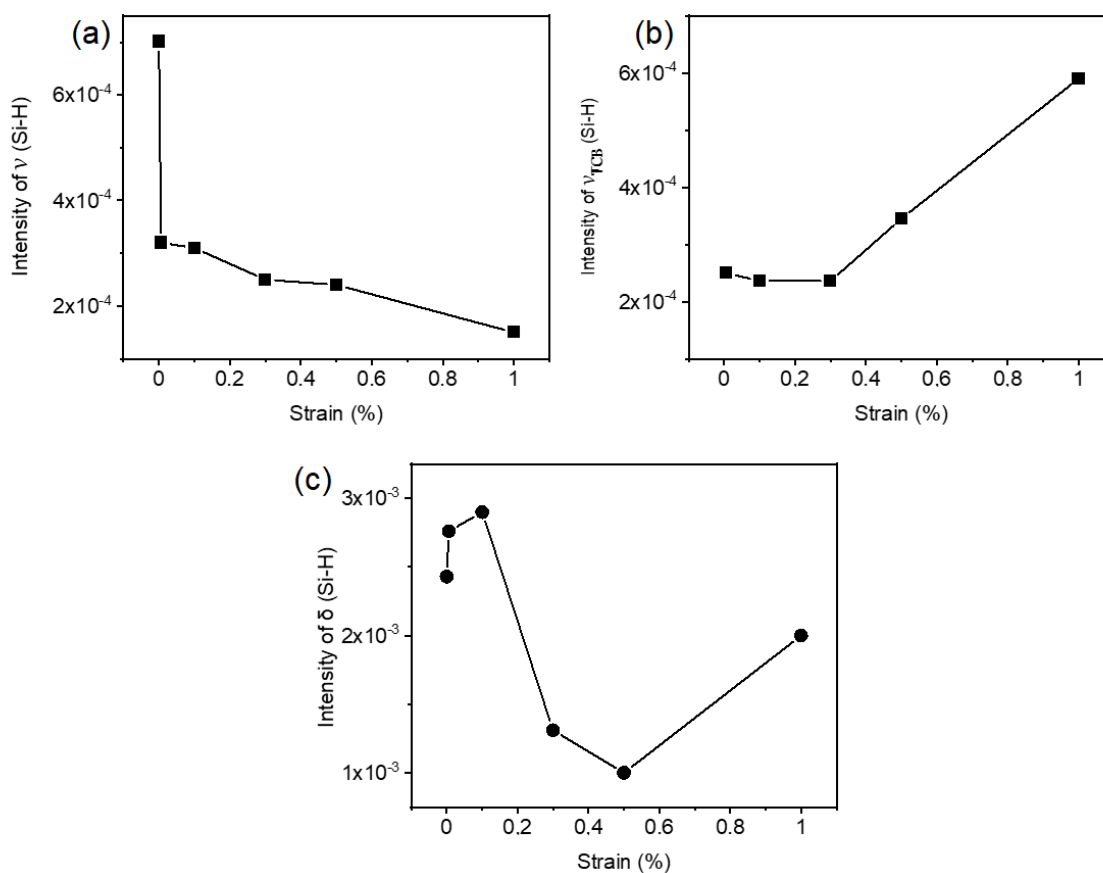


Figure 4.5. Variation of peak intensity as a function of strain: (a) intensity of stretching Si-H mode, (b) intensity of new induced band (three center bond (TCB)) due to strain effect, and (c) intensity of bending Si-H mode. All of the peaks are fitted by Lorentzian function (Appendix A, Table A1, A2 and A4).

Dissociation and transformation of some hydrogen bonding configurations into other configurations may be the underlying reason for stretching band intensity¹²⁶. In the current case, appearance of new band in the vibrational spectra of the bonded hydrogen is anticipated. Because experiments (applying strain and measuring the IR spectra) are performed inside a N_2 -purged glovebox, potential source of contamination is not involved to the band at $\sim 1712\text{ cm}^{-1}$. We hypothesize the generation of new band manifesting in the intensity change of bending mode at 626.40 cm^{-1} . Furthermore, deconvolution of the Si-H bending mode (626.40 cm^{-1}) into

three components (*Appendix A, Figure A3*) led to the discovery of even more new bending modes. The redistribution of hydrogen during the bending is clearly demonstrated in Figure 4.5, where we display the intensity of the bending band (626.40 cm^{-1}) and the intensity of the band at 2083.3 cm^{-1} as a function of strain.

Decreasing in intensity of the stretching band and fluctuation in intensity of bending band, goes with the appearance of a new peak at $\sim 1712\text{ cm}^{-1}$. Diffusion of a hydrogen atom from the Si-H site to form a three-center bond (TCB): Si-H-Si could be a reason¹²⁶. The formation of a TCB in crystalline silicon is predicted in which two silicon atoms harbor the hydrogen atom (bond-centered (BC) hydrogen) or in an asymmetric position¹²⁷⁻¹²⁹. The hydrogen is bonded to silicon atoms occupying antibonding (AB) positions in hydrogenated n-type GaAs: Si and there is a line corresponding to the Si-H vibration at 1717 cm^{-1} ¹³⁰. Several infrared transmission spectra show that hydrogen is capable to occupy two kind of sites in hydrogenated amorphous boron (a-B:H), a bridging hydrogen site (three B-H-B bond) or a terminal site (B-H)¹³¹. B-H complex and B-H-B show their absorption band at 2560 cm^{-1} and 2050 cm^{-1} , respectively. Findings that resonate from the above discussion are as follows: (a) a stretching band at frequency very similar to those of the corresponding complexes as with in crystalline or amorphous silicon is observed in the Si-H modes of strained H-Si(111); and (b) the Si-H bond with H in the TCB position is vibrated in our sample at a frequency that is lower than the stretching mode at 2038.3 cm^{-1} . According to the analogy with Si-H in H-Si(111) and B-H in a-B:H or other similar examples, band in strained H-Si(111) at $\sim 1712\text{ cm}^{-1}$ is proposed to be attributed to the stretching mode of TCB Si-H-Si formed during bending. The current findings are easily interpreted by the hydrogen diffusion model if the mentioned assignment is correct. Dissociation of Si-H bonds next to weak Si-Si bonds is occurred when strain along the [100] direction applies. In this regard, the H atom traverses to the off-bond sites leading to termination a normal dangling bond¹²⁶. Relying on this background, a new model for ϵ -H-Si(111) with Si-H-Si bond is constructed. Atomic configuration of relaxed unstrained and strained models is shown in Figure 4.6a.

The strained model (Figure 4.6a) is constructed in which strain is applied in direction of [100] with orientation of metastable Si-H-Si bonds in relation to directions of Si-Si back bonds; $[\bar{4}\bar{4}\bar{1}]$ direction. As it was shown¹⁹, the reactivity of the bonds is increased by the strain, especially in those most nearly aligned with the direction of the stress. Since the $[\bar{4}\bar{4}\bar{1}]$ direction has a lower angle ($\theta = 35.1^\circ$) with the strain direction (*Appendix A, Figure A4*), the oriented bonds in this direction are more affected, and the probability of Si-H-Si formation is higher along $[\bar{4}\bar{4}\bar{1}]$. According to the calculation, new orientation on the surface is evident by the hydrogen because of the strain. This demonstrates the ability of hydrogen to relieve strain on the network¹¹². In Table 4.2, data of changes in bond length of Si-Si back bonds and Si-H following strain is shown. In this model as the optimized structure indicate the H is not located at the center between two host Si atoms, and the optimized Si-H distance becomes 1.77 and 1.53 Å with a Si...H-Si angle of 121.6 deg (Figure 4.6d). Importantly, the findings of the experimental part and the assumption of the TCB model are in accordance with the results raised by DFT calculations of the relevant vibrational frequencies. The calculated IR spectra of unstrained H-Si(111) and

strained models are demonstrated in Figure 4.6e. Results of the experimental part is confirmed the presence of new Si-H stretching mode at around 1915 cm^{-1} and remarkable alterations in the intensity of Si-H stretching and bending modes. Therefore, the calculated peak at 1915 cm^{-1} corresponds to the measured peak at 1712 cm^{-1} . To interpret the observed new peak, we used Molden¹³², a visualization tool that allowed us to assign the calculated vibrational modes as accurately as possible (*Appendix A, Table A3*).

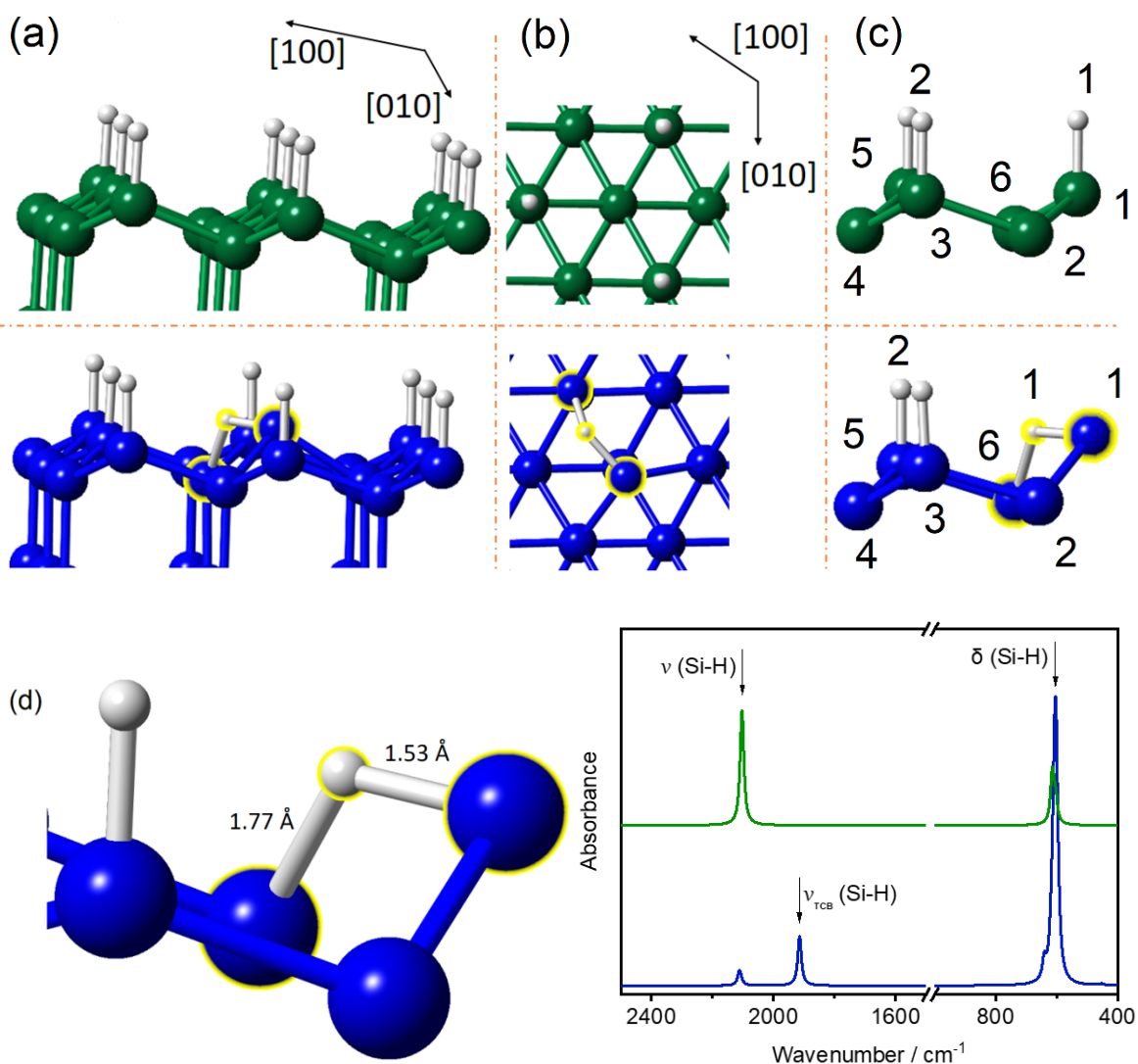


Figure 4.6. Possible configuration that resulted from strain effect on Si-Si and Si-H bond length and orientation; hydrogen diffusion, breaking Si-Si bond and formation of Si-H-Si (TCB). (a) and (b) show the side and top views of models, respectively. (c) Represent the part of models experienced higher change following hydrogen movement. Information regarding the Si-Si and Si-H bonds (presented in (c)) is provided in Table 4.2. (d) Measured bond distance of Si-H-Si using CrystalMaker software, and (e) calculated IR spectra of unstrained H-Si(111) (green curve) and 0.3% strained model (along [100] direction) containing Si-H-Si bond (blue curve). Molden is used to define the type of the vibrational modes of the Si-H-Si bond (*Appendix A, Table A3*).

Activation energy for the production of the metastable Si-H-Si configuration is significantly high, around 1.5 eV¹³³. However, this activation energy would be 1.7 eV based on our calculation which possibly recombination of excess band tail carriers at some of the weakest Si-Si bonds use the most energy transfer¹³³. The Si-Si bond next to the Si-H bond is weakened because the electronegativity of H is higher compared with that of Si. The H atoms possibly hop back to their initial configuration or diffuse apart upon the formation of Si-H-Si sites¹³³. Larger length of the Si-H bond in the three-center configuration than its initial configuration (Si-H / 1.5 Å) makes the bond of the H atom loose (metastable).

Table 4.2. Calculated Si-Si and Si-H bond lengths for the optimized structures of two models, unstrained H-Si(111) and strained H-Si(111).

Bond length / Å	Unstrained H-Si(111)	Strained H-Si(111)
Si ₁ -H ₁	1.504	1.531
Si ₅ -H ₂	1.504	1.504
Si ₁ -Si ₂	2.343	2.373
Si ₂ -Si ₃	2.343	2.352
Si ₃ -Si ₄	2.343	2.350
Si ₄ -Si ₅	3.343	2.345
Si ₅ -Si ₆	3.343	2.350
Si ₆ -Si ₁	3.343	2.890
Si ₆ -H ₁	1.504	1.776

The calculated IR spectrum (Figure 4.6e) also shows the splitting of bending Si-H mode. The vibrational mode of new peak (at 640.46 cm⁻¹), which shows the bending vibration related to TCB bond, is assigned using the Molden software. This observation aids in the identification of different species obtained by deconvolution of the measured bending Si-H peak in the experiment (Figure 4.4b). We concluded that the splitting of bending mode into three components may arise from (1) the formation of TCB bonds (frequency higher than ~626.40 cm⁻¹ (terrace monohydride bending mode) for the strained samples) and (2) in agreement with Refs. ¹³⁴⁻¹³⁵, we attribute the bending mode measured at lower frequency than 626.40 cm⁻¹, to a monohydride step vibrations.

4.4. Surface reactivity of unstrained H-Si(111) towards liquid water/experiment (II)

The chemical stability of a passivated Si substrate is determined by two forms of bonds: up Si-H bonds and Si-Si back bonds to the underlying layer. In order to have a better understanding as well as controlling of the chemical processes on H-terminated silicon surfaces, there is an essential need to characterize the chemical reactivity of these bonds. As a result, in this study the reactivity of up Si-H bonds is investigated first, followed by the reactivity of Si-Si back bonds. The IR spectra of H-Si(111) samples before and after reaction with water at various reaction times are shown in Figure 4.7. Monohydride Si gives rise to one peak at 2083.7 cm⁻¹ after

treatment of surface with HF/NH₄F²¹. The IR spectrum of fresh H-Si(111) before reactivity with water is shown in black curve (Ref). When the surface is reacted with water for different reaction times (green IR spectra), the Si-H peak almost remain unchanged. As previously shown in experimental observations, the reaction between water vapor and H-Si(111) surface is happened at the temperature threshold of 350°C in which OH dipole replaces with adsorbed H¹³⁶. It implies that there is energy barrier that must be resolved in order for the reaction to begin. NEB calculations are used to obtain more details about the reaction pathway and energy barriers. The relevant energy profile for oxidation of Si-H and Si-Si back bonds along the reaction pathway is depicted in Figure 4.7c. The activation energy of 1.8 eV (41.5 kcal mol⁻¹) characterizes the H₂O reaction with Si-H site on the flat surface forming Si-OH and H₂ (g) (Figure 4.7c, panel b). The reaction is exothermic with the ΔE value of -0.5 eV (-11.5 kcal mol⁻¹). As a result, the oxidation of up Si-H bonds (Si-H→Si-OH) is hindered by the high energy barrier of 1.8 eV. Peaks in the range of 2100-2300 cm⁻¹ and 1250-1000 cm⁻¹ relating to oxide surface, O_x-SiH, and SiO_x, respectively, are predicted to be observed during the oxidation of Si-Si back bonds²¹. No peak in IR spectra can be found in the described ranges, as shown in Figure 4.7a and 4.7b (green curves). Therefore, we proceed our NEB calculations to determine the energy barriers for the oxidation of Si-Si back bonds.

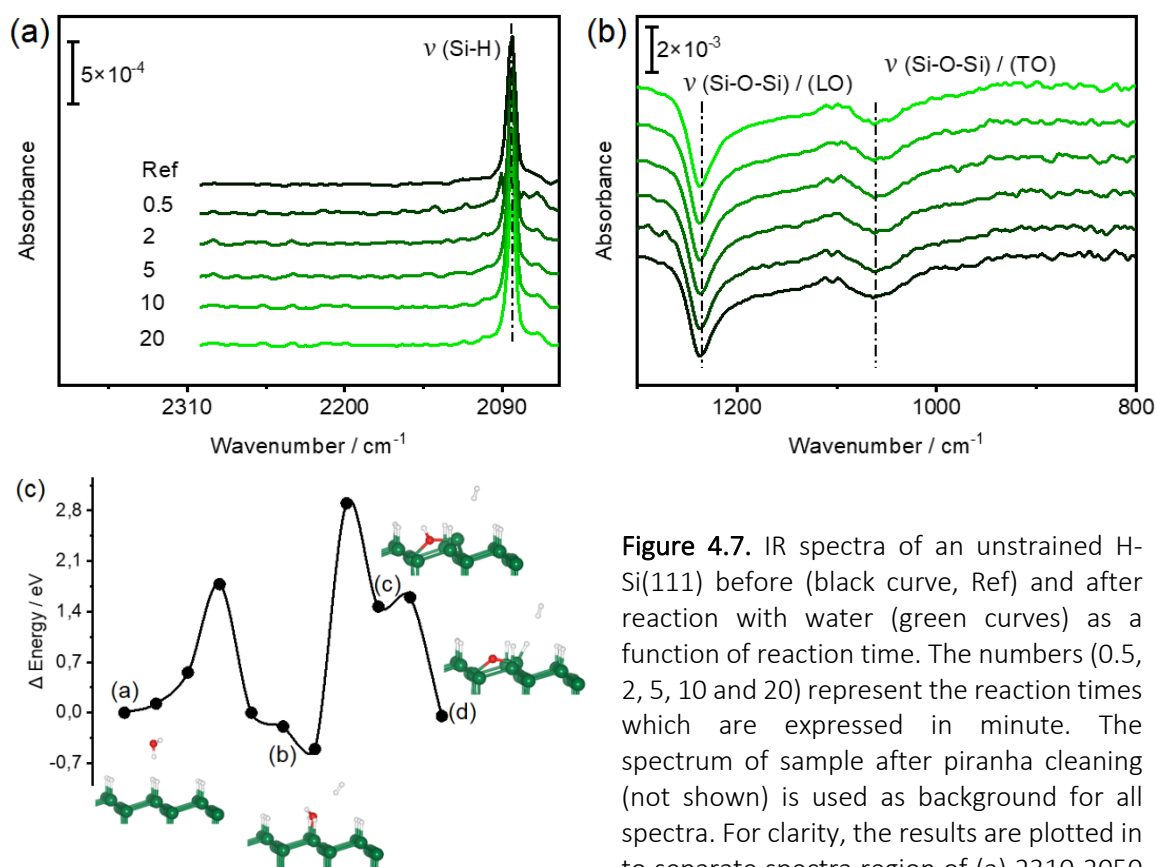


Figure 4.7. IR spectra of an unstrained H-Si(111) before (black curve, Ref) and after reaction with water (green curves) as a function of reaction time. The numbers (0.5, 2, 5, 10 and 20) represent the reaction times which are expressed in minute. The spectrum of sample after piranha cleaning (not shown) is used as background for all spectra. For clarity, the results are plotted in to separate spectra region of (a) 2310-2050

cm⁻¹ and (b) 1300-800 cm⁻¹. (c) Energy profile as a function of reaction coordinate for the reaction of water with the Si-H bond and Si-Si back bond. The panels (a, b, c and d) indicate the energy of the critical points taking as a reference the water molecule adsorbed on the surface.

According to calculations (Figure 4.7c, panel c), the insertion of the OH group of Si-OH into the Si-Si back bond is hampered by high energy (3.2 eV (73.79 kcal mol⁻¹). However, transferring the H atom of OH toward the close silyl radical (panel d) encounters a barrier of 0.84 eV (19.37 kcal mol⁻¹). Consequently, achieving the oxidized surface from a surface containing Si-OH group needs to overcome the high energy barriers. Incorporating very high temperature to the system is a way to address the high required issue^{21, 136}. Absence of peak corresponding to oxidation of silicon surface may be due to the existence of high energy barriers for the last steps (Figure 4.7c).

4.5. Surface reactivity of strained H-Si(111) towards liquid water / experiment (III)

As in section (II), the reactivity of up Si-H bonds is studied first, followed by the reactivity of Si-Si back bonds.

IR spectrum of fresh H-Si(111) is displayed in Figure 4.8 (black curve, Ref). The IR spectra of a strained H-Si(111) (strain = 0.3%) after reaction with water are shown in blue curves as a function of reaction time. After 0.5 minutes of water reaction with strained surface, the intensity of the Si-H stretching mode decreases (Figure 4.8a). This suggests oxidation of up Si-H bonds (replacing the H with OH groups). It is important to note that oxidation of up bonds is not the only factor that can cause the Si-H band intensity to decline. Since the IR spectrum of the sample after piranha cleaning is used as a background for all spectra, the effect of strain on decreasing Si-H stretching band intensity should also be considered (as explained in the section (I)). Appearance of Si-OH bending mode (800-1000 cm⁻¹) could possibly confirm the substitution of some atop Si-H groups with atop OH groups¹³⁷⁻¹³⁹. The peak related to the bending mode for Si-OH groups is around 809.61 cm⁻¹ (Figure 4.8b), (*Appendix A, Figure A5 and Table A5*). As a result, in comparison to unstrained H-Si(111), the results show that after reactivity with water, up Si-H bonds in ϵ -H-Si(111) are oxidized. The oxidation of up Si-H bonds in ϵ -H-Si(111) is also confirmed by our DFT calculations (*Appendix A, Figure A9*). Positive absorption modes at ~ 1050 cm⁻¹ and ~ 1220 cm⁻¹ in Figure 4.8c which is sequentially associated to the asymmetric Si-O-Si transverse optical (TO) and Si-O-Si longitudinal optical (LO) stretching modes, show oxidation of the silicon surface^{8-9, 137}. Remarkably, there is no Si-O-Si oxidation species underneath surface-bound Si-H sites as no clear absorption appeared in the range of 2150-2300 cm⁻¹ (Figure 4.8a) which represents to Si-H species with oxygen inserted in the Si-Si back bonds (designated as O_x-SiH species)^{21, 140}. The O_x-SiH modes are absent in this study as compared to experiments on H-Si(111) samples under certain conditions like gas-phase O₂ or H₂O at high temperatures²¹. These results suggest the dominance of different oxidation pathways while strain is applied to the samples.

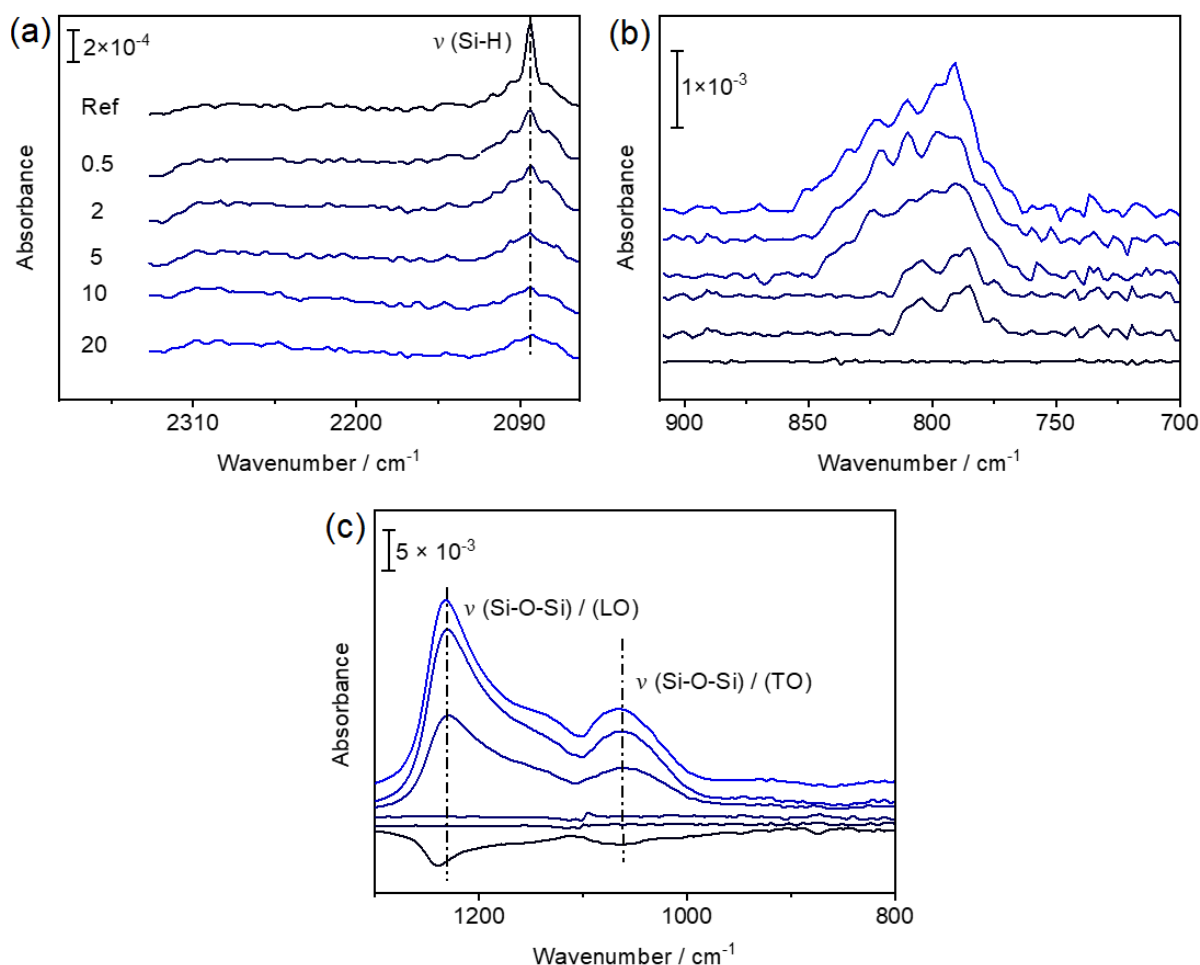


Figure 4.8. IR spectra of strained H-Si(111) after reaction with water as a function of reaction time. Black curve (Ref) is spectrum of fresh NH₄F/HF treated sample. The absorbance spectra are processed by subtracting IR spectrum of sample after piranha cleaning. The numbers (0.5, 2, 5, 10 and 20) show the reaction times (expressed in minute) of strained H-Si(111) (strain = 0.3%) with water. The spectra are separated into three important regions; (a) Si-H stretching peak, (b) generation of bending Si-OH mode, and (c) the formation of Si-O-Si modes. The data for the best fit with Lorentzian function is provided in Appendix A, Figures A5, A6 and A7.

After 0.5 and 2 minutes of reaction, the Si-H stretching modes are reduced, accompanied by rapid generation of Si-O-Si peaks and continuous Si-OH intensity enhancement. Two important points could be extracted from Figure 4.8: the formation of oxide was retarded in spite of decrease in Si-H intensity during the first 2 min of reaction time; the oxide thickness did not commence to increase concurrently as the Si-H intensity decreases. This provides the proof that the reduction in Si-H intensity only resulted from strain effect and oxidation of up Si-H bonds. The surface is attacked easily by H₂O when oxidation (partially) is occurred at the topmost layer of the H-Si(111) surface resulting in a sharp escalation in Si-O stretching vibration. It seems that Si-OH groups might remain intact throughout the oxidation of back bonds substantiating in continuous increase in Si-OH. Two possibilities are proposed for rapid surface oxidation; formation of (1) O_xSi-OH or (2) SiO_x. Any shift in the Si-OH vibration mode

could be seen upon residing of the oxygen atoms directly beneath the Si-OH¹³⁷. The obtained peak frequency related to Si-OH mode for different reaction time of the surface with water (*Appendix A, Table A5*) shows that the frequency almost remained unchanged around 809.61 cm⁻¹. DFT calculation is carried out on three Si-OH terminated ϵ -H-Si(111) oxide surfaces in order to test this hypothesis (*Appendix A, Figure A8*). The concluding remark could be covering the surface by Si₃Si-OH and SiO_x groups. The surface oxidation of hydroxylated H-Si(111) with water is investigated using NEB calculations to support these results. The initial structure we use is hydroxylated H-Si(111) which is strained along [100] and contains Si-H-Si group along the $[4\bar{4}\bar{1}]$ direction. According to the NEB calculation, this reaction progresses through two low-energy barriers (E value= -0.481 eV (-11.09 kcal mol⁻¹)) (Figure 4.9). A H₂ species and OH group (panel b) are produced following the reaction between water and metastable Si-H-Si bond with ΔE value of 0.3 eV (6.9 kcal mol⁻¹). Then, conversion into Si-O-Si bonds, as shown in panel c, with the activation energy of 1.0 eV (23 kcal mol⁻¹) is occurred. The final remark may be the Si₃Si-OH and SiO_x groups covering the surface of strained H-Si(111) after reaction with liquid water.

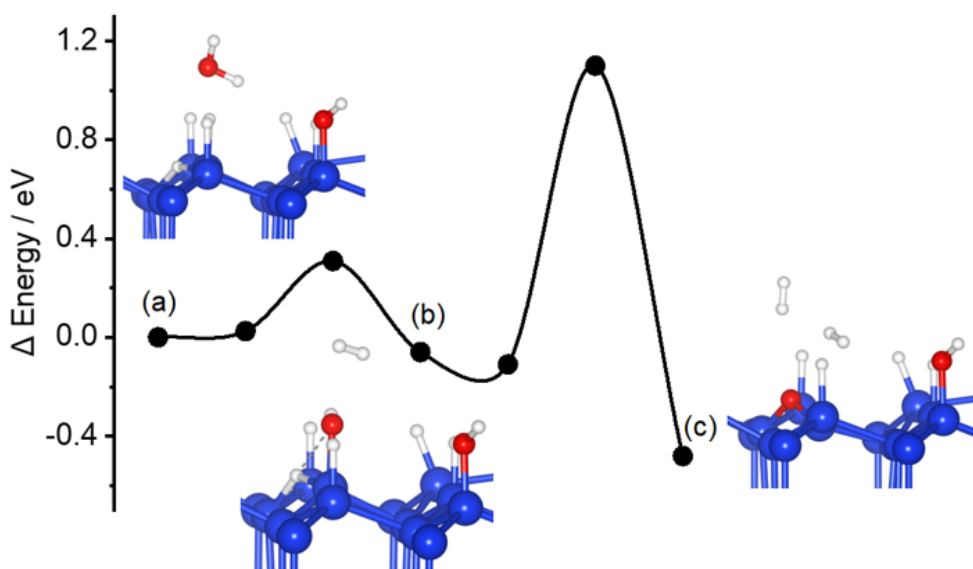


Figure 4.9. Energy profile for the reaction of hydroxylated strained H-Si(111) with water. (a-c) Panels show the initial, intermediate and final structures, respectively.

To monitor the strain effect on surface reactivity, we also performed in-situ contact angle measurements while bending. It is common practice to verify the roughness of the surfaces during these types of measurements with additional tests such as contact angle hysteresis, IR measurements, Atomic Force Microscope (AFM) and so on to ensure that the variations in contact angle are not due to surface roughness. To confirm the observation of change in contact angle values, we applied two more tests (IR measurement and DFT calculations) in this paper. However, to make sure about reliability of results this section must be completed and that was the reasons we add these part in *Appendix B (Figures B1, B2 and B3)*.

4.6. Conclusion

Two types of bonds, the up Si-H bonds and the Si-Si back bonds to the underlying layer, determine the chemical stability of passivated Si substrate. In order to have a better understanding as well as controlling of the chemical processes on H-terminated silicon surfaces, there is an essential need to characterize the chemical reactivity of the bonds. The dominant chemical process under an ambient condition is oxidation. The rate of oxidation is influenced by environmental factors, presence of reacting agents, and inherent sample specifications like surface morphology.

The spectra presented in this work demonstrate prominent aspects of the chemistry of silicon surface which is affected by strain. First, strain shows its potential to change the pathway reaction of hydrogen terminated surface that considerably shifts the kinetic of surface reactions. There is high priority of oxidation in subsurface Si-Si back bonds only after 5 min of the reaction time. This finding underlines the catalyzing role of strain in surface reactivity to overcome the activation energies. This study also revealed that Si-OH linkages with substrate oxidation is produced upon the reaction between water and strained hydrogen terminated surface. Also, it demonstrates the existence of oxidant producing the oxide layer; hydrated silicon oxide (Si-OH) and SiO_x species. We concluded in this study that strain causes fast oxidation of the Si-Si backbone, and Fuchs et al.¹⁴¹ demonstrated that oxygen atoms incorporated directly into Si-Si bonds at the interface are a source of optical anisotropy and induce strain on the structure. As a result, it's also worth noting that applied strain on the structure and Si-Si back-bond oxidations are mutually exclusive.

Chapter 5

5. STRAIN EFFECT ON CO ADSORPTION ON CALCITE(10.4) SURFACE

Some sections of this study that deal with CO adsorption on an unstrained calcite(10.4) surface were adapted from a previously published paper: "CO adsorption on the calcite(10.4) surface: a combined experimental and theoretical study" with permission from the journal of Physical Chemistry Chemical Physics.

5.1. Aims and objectives

Various experimental and theoretical methods have been used to investigate the microscopic nature of the calcite(10.4) surface^{46, 142-143}. The sources and geometry of two departures from the bulk-truncated (1×1) structure have been documented, but their origins and geometry are currently being debated. First, atomic force microscopy (AFM) results^{46, 144-145} revealed a loss of pg surface symmetry (often referred to as "row-pairing"); an asymmetric tip probing an unrelaxed surface can also explain this surface relaxation. Second, using low energy electron diffraction (LEED)¹⁴⁶ and AFM data^{145, 147}, the existence of a (2×1) reconstruction has been hypothesized. An rectangular supercell with dimension of 10.0 Å and 8.1 Å, positioned along the $[0\bar{1}0]$ and $[42\bar{1}]$ directions, characterizes this reconstruction. Here, we aimed to study the surface structure of the UHV-cleaved calcite(10.4) surface using polarization-resolved infrared reflection absorption spectroscopy (IRRAS) with CO as the probe molecule, as well as non-contact atomic force microscopy (NC-AFM) experiments and density functional theory (DFT) calculations. We would like to emphasize that no previous IRRAS studies of adsorbates on well-defined surfaces of macroscopic calcite single crystals are known. Technical difficulties in recording IR data utilizing reflection geometries for dielectric substrates have just recently been overcome, resulting in a lack of experimental data¹⁴⁸⁻¹⁴⁹. The influence of external strain on the adsorption characteristics of CO molecules in the calcite(10.4) surface is then determined using DFT. Compressive and tensile uniaxial strains of 1 %, 3 %, -1 %, and -3 % were examined¹⁵⁰.

5.2. Methodology

5.2.1. Infrared reflection absorption spectroscopy

In a multi-technique UHV apparatus, all IRRAS tests were carried out (Prevac, Poland). Korth Kristalle GmbH (Altenholz, Germany) provided 6 large blocks of calcite(10.4) single crystal (8×8×12 mm³) with optical quality. Before attaching the blocks to the sample container, they were cut into small pieces in the atmosphere. A scalpel blade coupled to a wobble stick was used to cleave the calcite single crystal in the UHV chamber. Figure 5.1 shows an image of the sample holder with a single calcite crystal fragment. The wobble stick inside the UHV chamber can

move the central part of the base plate in clockwise and anticlockwise directions to modify the azimuthal orientation of the specimen. Before cleavage, the single crystal was briefly annealed after being placed into the UHV system. The samples were instantly transferred to the IRRAS chamber after cleavage. The IRRAS data were collected using polarized infrared light with a spectral resolution of 1 cm^{-1} at a grazing incidence angle (80°). The UHV chamber's base pressure was set at 4.0×10^{-11} mbar. CO was dosed using a capillary tube that ended in front of the sample, with the sample temperature kept at 62 K. A K-type thermocouple affixed to the sample holder's edge was used to monitor the sample's temperature. 1.33×10^{-6} mbar s corresponds to one Langmuir (L) exposure.

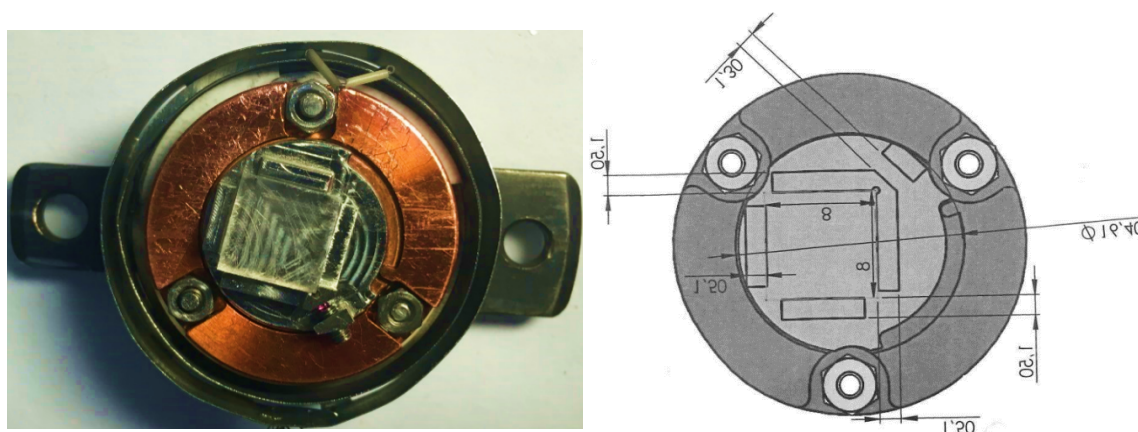


Figure 5.1. Photograph of a calcite (CaCO_3) single crystal mounted in the sample holder (designed for UHV cleavage) with the (10.4) surface pointing up. Size of the base plate of the sample holder is $8 \times 8\text{ mm}^2$.

5.2.2. Non-contact atomic force microscopy (NC-AFM)

In a system independent from the IRRAS setup, sample preparation and NC-AFM tests were carried out under ultra-high vacuum conditions. Using a scalpel blade mounted to a wobble stick, calcite crystals (Korth Kristalle, Altenholz, Germany) were sliced in-situ to form a (10.4) surface¹⁵¹. The crystal was placed on a double sample holder with an additional Ag(111) surface for tip preparation and heated to roughly 440 K for 1.5 hours to eliminate residual charges¹⁵². NC-AFM studies were carried out using a ScientaOmicron LT qPlus gen.III microscope (Tunusstein, Germany) controlled by a MATRIX controller and W-tips attached to qPlus sensors¹⁵³ as supplied by the manufacturer. On the Ag(111) surface positioned near the calcite sample, tips were produced using standard scanning tunneling microscopy techniques. At background pressures about $p \sim 5 \times 10^{-8}$ mbar, CO was dosed directly into the scan head (Tsample o 10 K while opening the shields). To improve image contrast, metal tips were partially terminated with CO molecules¹⁵⁴. After the NC-AFM experiments, the surface orientation was determined ex-situ by optically detecting the orientation of the ordinary and extraordinary rays of the birefringence.

5.3. Computational method

The generalized gradient approximation (GGA) and the PBE functional, as implemented in the Vienna ab initio simulation package, were used to perform DFT computations (VASP)¹⁵⁵. The projector-augmented wave (PAW) scheme was used to represent the electron–ion interaction¹²². Up to a kinetic energy of 400 eV, the electronic wave functions were expanded into plane waves. The calculations presented here were performed on a slab (four layers thick) that exposed a (10.4) surface with a (1×1) unit cell and included a total of 40 atoms (Ca: 8, C: 8, O: 24), see also Figure 2.1^{43, 156}. This model is comparable to others used in previous research¹⁵⁷⁻¹⁵⁸. It was discovered that a vacuum region of 20 Å was large enough to preclude interactions between the surface and adsorbed molecules, as well as their replica images. Coverage is defined as the quantity of CO molecules divided by the number of surface Ca ions. Except for the lowest layer, all degrees of freedom were allowed to relax until the stresses on the atoms were less than 1 meV Å⁻¹. The total energy and Hellmann–Feynman forces on the atoms (and stresses on the unit cell) were used to optimize the atomic coordinates (and unit cell size for the bulk materials) using a conjugate gradient technique. When the forces on the atoms were less than 1 meV Å⁻¹, the structures were regarded entirely relaxed. Within the Monkhorst–Pack scheme, the Brillouin zone integration was done with a 4 × 4 × 1 mesh. The force-constant method was used to calculate vibrational eigenmodes and frequencies. The starting geometry for the optimization was a CO molecule (bond length 1.14 Å). The force-constant method was used to calculate vibrational eigenmodes and frequencies. The starting geometry for the optimization was a CO molecule (bond length 1.14), positioned vertically on top of Ca²⁺, positioned vertically on top of Ca²⁺.

The difference in total energy between the bulk and the surface per unit area is known as the surface energy, and it may be calculated using the following equation for a stoichiometric surface¹⁵⁹:

$$E_{surf} = (E_{slab} - NE_{bulk})/2A \quad (5-1)$$

where E_{slab} represents the total energy of the surface, E_{bulk} represents the bulk energy, N represents the number of unit cells utilized to construct the slab, and A represents the surface area.

Our calculations yielded a surface energy of 0.50 J/m², which is quite similar to prior estimates¹⁶⁰⁻¹⁶¹.

As a function of CO molecule coverage, the adsorption energy (E_{ads}) can be computed as follows¹⁶²:

$$E_{ads} = \frac{E_n - E_0 - nE_{CO}}{n} \quad (5-2)$$

where E_n is the energy of a surface with n molecules, E_{CO} denotes the energy of a gas-phase molecule, and E_0 denotes the energy of a clean slab.

Strain value is imposed due to the values obtained from previous studies (strain range 0–5%)⁵⁴. The applied elongation, ΔL , can be obtained based on the initial length of the unstrained sample along the loading direction, L_0 , and the loading engineering strain which is equivalent

to $\Delta L/L_0$. The same procedure is used to applied compression along the same direction ($[42\bar{1}]$). The simulation box size in the perpendicular direction of the loading was then adjusted accordingly to ensure uniaxial stress condition in the study, so that stress remained negligible in the perpendicular direction¹²⁴. After applying the loading conditions, structural relaxation was achieved using the conjugate gradient energy minimization method with 10–6eV criteria for energy convergence. To calculate IR spectra, the IBIRON = 8 is set to determine the Hessian matrix (matrix of second derivatives).

5.4. Results and Discussion

5.4.1. Experimental part

After varied exposures of the freshly cleaved calcite(10.4) surface to CO at a substrate temperature of 62 K, the polarization-resolved IRRAS data shown in Figure 5.2a were acquired for p-polarized IR light incident along the surface. An asymmetric single band at 2175.8 cm^{-1} is found for a 0.5 mL exposure, which is attributed to the stretching vibration of CO molecules bound with the C atom to Ca^{2+} -cations at the calcite surface. When the exposure was raised to 0.1 L, the band became more intense while shifting somewhat to a lower frequency, 2174.4 cm^{-1} . The decrease of frequency continued with increasing exposures until a value of 2173.4 cm^{-1} was attained. No additional increases in band strength or changes in band shape were detected for exposures greater than 2.0 L, showing that the calcite(10.4) surface was saturated with CO and no multilayer development occurred at this substrate temperature. In IRRAS data taken with s-polarized light, the CO vibration was also visible (Figure. 5.2b, bottom).

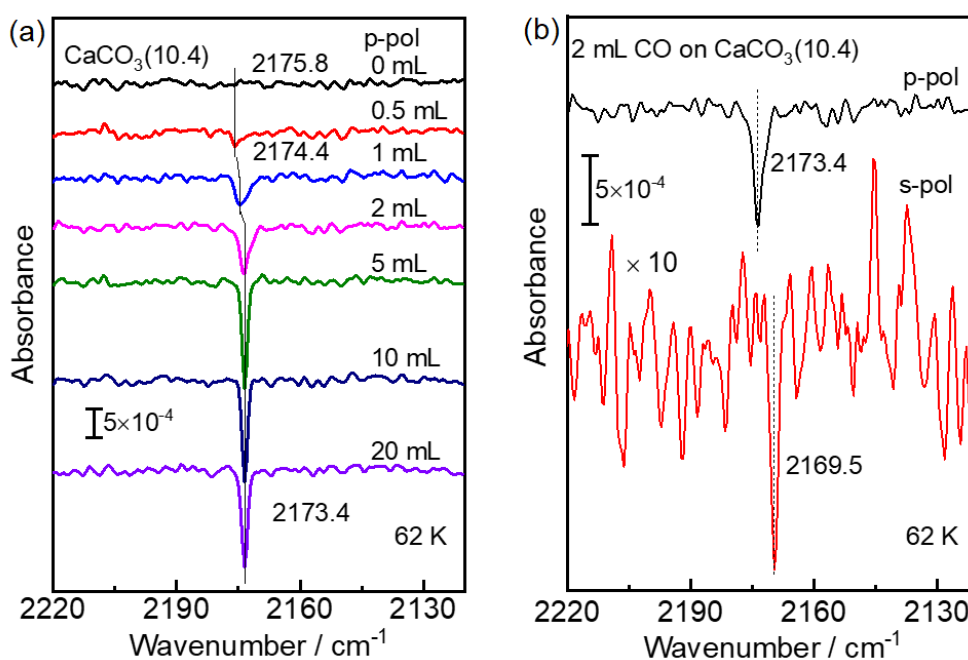


Figure 5.2. (a) IRRAS spectra of CO adsorbed onto the calcite(10.4) surface with increasing exposures using p-polarized light at 62 K. (b) IRRAS spectra for 2 mL CO adsorbed onto the calcite(10.4) surface at 62 K using p-polarized light (top) and s-polarized light (bottom).

When compared to that excited by p-polarized light, the intensity is substantially lower by an order of magnitude (Figure 5.2b, top). Because only vibrational modes with a component of their transition dipole moment (TDM) oriented parallel to the surface may be activated by s-polarized light, the presence of a vibrational characteristic for s-polarization reveals that there must be a static or dynamic tilt angle¹⁴⁹.

We took IRRAS data after heating the CO adlayers to various temperatures in order to calculate the binding energy of the CO adlayers (see Figure 5.3a). The fluctuation in integrated band intensities as a function of surface temperature is seen in Figure 5.3b. For temperatures below 92 K, the position (Figure 5.3a) and intensity (Figure 5.3b) of the CO–Ca²⁺ band remain unchanged. CO begins to desorb from the surface after further annealing to 100 K, resulting in a drop in band intensity and a minor blue shift in the vibrational frequency. Using the Redhead equation¹⁶³, a simple quantitative examination of the IR band intensity evolution reveals a binding energy of 0.31 eV for CO on the calcite(10.4) surface.

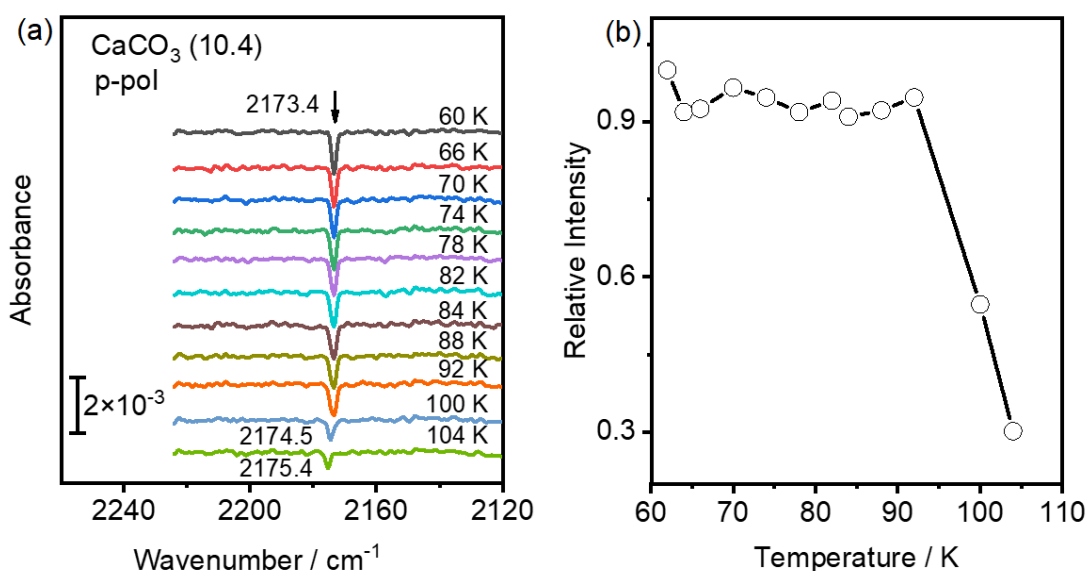


Figure 5.3. (a) IRRAS spectra for 2 mL of CO adsorbed onto calcite(10.4) surfaces at $T = 62$ K and after annealing to the temperatures indicated. (b) Integrated spectral intensity evolution as a function of temperature.

After dosing CO into the cold scan head on calcite(10.4) for three distinct total periods of 25 s, 50 s, and 150 s, we collected AFM micrographs to study the adsorption location and CO arrangement, resulting in coverage of roughly 0.006, 0.013, and 0.067 monolayers (ML). A coverage of two CO molecules per (1×1) unit cell is defined as one ML. It's worth noting that the pressure in the third experiment was slightly higher. Figure 5.4 depicts the corresponding results. In all images, the calcite surface structure is visible as four bright protrusions per (2×1) unit cell, with unit cell diameters of $10 \times 8.1 \text{ \AA}^2$, as indicated by white rectangles. The contrast in Figure 5.4a, b, and d indicates a staggered (zig-zag) structure along the $[4\bar{2}\bar{1}]$ direction, which is due to the differing orientation of the two carbonate groups within the surface unit cell.

In addition, in all micrographs, the (2×1) reconstruction is discernible as a modulation along

the [010] direction of the dark rows. The pg surface symmetry is preserved because no row-pairing reconstruction is visible. Individual dark depressions are seen and identified as single CO molecules, which are not visible on clean calcite(10.4) surfaces (examples are marked by white arrows in Figure 5.4).

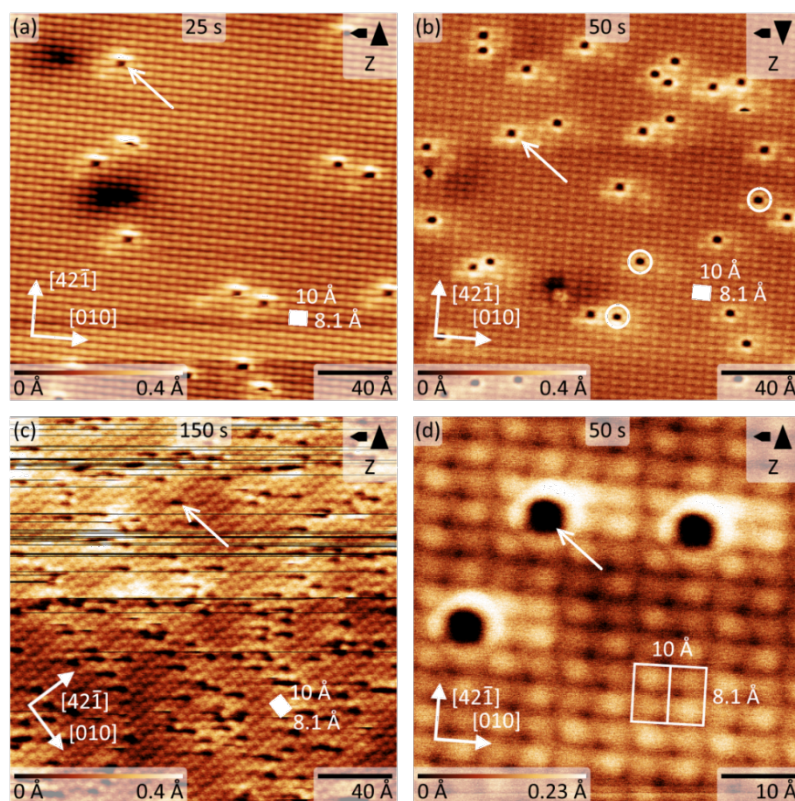


Figure 5.4. NC-AFM imaging of single CO molecules on calcite(10.4) at 5 K with total deposition durations of (a) 25 s, (b and d) 50 s, and (c) 150 s. Data in (b and d) were acquired after dosing further 25 s onto the sample presented in (a). Data in (c) are acquired after dosing for 25 s and additional 125 s. Single CO molecules are marked by an arrow in all figures, molecules slightly off-center with white circles in (b). The (2×1) unit cell is marked by white rectangles in all micrographs.

These depressions are well isolated from one another, yet they are frequently moved around throughout scanning (see Figure 5.4c). We didn't notice any clusters or adsorbate islands forming. The molecules are placed at the site of calcite surface characteristics photographed brightly in NC-AFM, as shown in the detailed micrograph in Figure 5.4d. Despite the IRRAS measurement of a single sharp band, we see molecules somewhat off-center of the bright calcite surface feature (examples are marked by white circles in Figure 5.4b). However, at the IRRAS measurement temperature of 62 K, the difference between these orientations may be thermally averaged, whereas the barrier is too great at the NC-AFM imaging temperature of 5 K. We can also deduce from the IRRAS data that the bright protrusions in these NC-AFM micrographs represent the sites of the surface Ca^{2+} cations because the CO molecules are positioned there.

For NC-AFM measurements of calcite(10.4) surfaces, two imaging models were offered previously: a “positive potential nanotip” imaging model and a “negative potential nanotip” imaging model¹⁶⁴. The imaging was explained as being dominated by electrostatic interactions, in which the oxygen or calcium sublattices are viewed as “bright” due to attraction with a positive or negative ion at the tip apex, respectively¹⁶⁴. As a result, we conclude that the data presented here were collected using a probe tip with a negative termination.

5.4.2. Computational part

5.4.2.1. CO adsorption on unstrained calcite(10.4)

Finally, DFT was used to investigate two distinct CO/calcite configurations: (i) a single CO molecule adsorbed within the (1×1) cell, equivalent to 0.5 ML coverage, and (ii) two CO molecules adsorbed within the (1×1) cell, corresponding to total monolayer coverage (1.0 ML). CO was adsorbed on top of a surface Ca site in all cases and was initially oriented perpendicular to the surface with the carbon pointing downwards. The common coordination of CO on metals and metal oxides conforms to this geometry¹⁶⁵. At 1 ML, DFT calculations revealed a tilt of 14.42° for the two CO molecules within the (1×1) unit cell, and tilts of 14.57° and 15.141 for the two CO molecules within the (1×1) unit cell. Figures 5.5 and 5.6 illustrate the optimal geometries produced for the various configurations, while Table 5.1 lists the relevant parameters. The influence of lateral interactions between CO molecules is revealed by the minor rise in tilt angle with coverage.

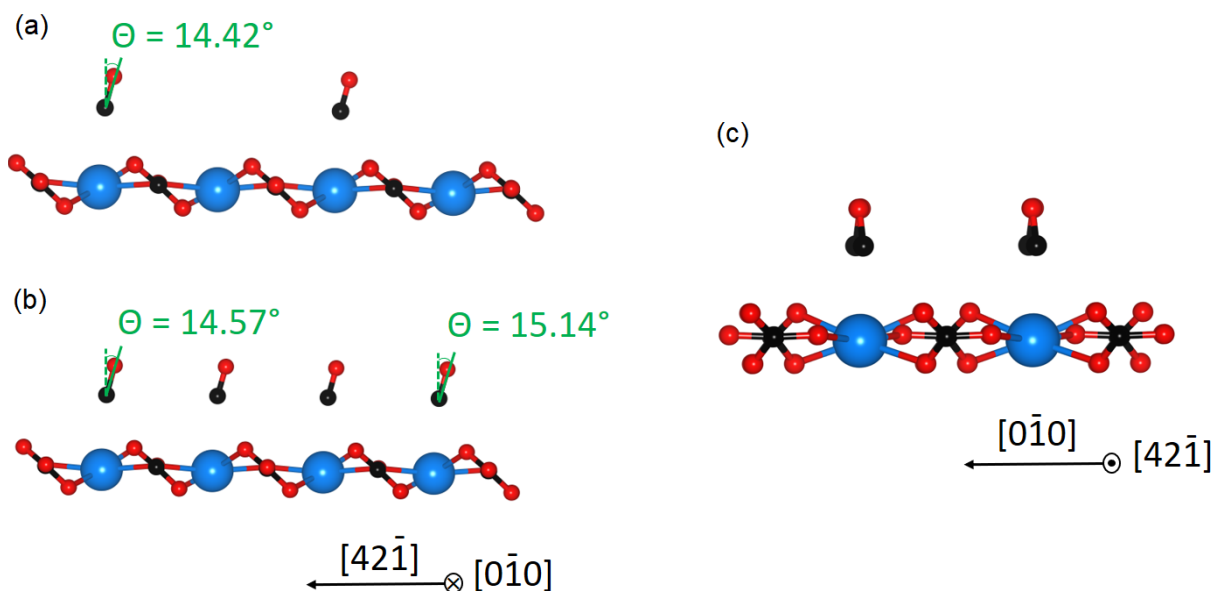


Figure 5.5. After energy minimization, side views of CO/calcite(10.4) for two distinct CO coverages of 0.5 ML (a) and 1.0 ML (b) (b and c). CO tilt angles are included.

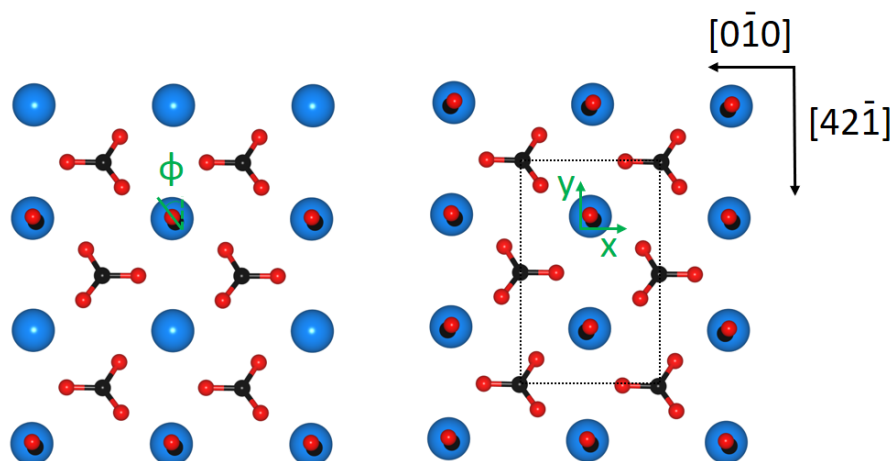


Figure 5.6. One carbon monoxide molecule (0.5 ML coverage, left) and a full monolayer of CO (right) on the energetically preferred adsorption site of a CaCO_3 surface unit cell. After their optimum configurations, ϕ denotes the azimuthal angle of adsorbed CO.

Table 5.1. Parameter characterization of CO/calcite(10.4) after geometry relaxation. The parameters $x(\text{C}-\text{Ca}(\text{surface}))$, $y(\text{C}-\text{Ca}(\text{surface}))$ and $z(\text{C}-\text{Ca}(\text{surface}))$ denote the distance between the carbon atom of the adsorbed CO molecule and the surface Ca ion. $\text{Ca}(\text{surface})-\text{O}(\text{subsurface})$ indicate the distance between the surface Ca ion and O presented in the subsurface. Θ (tilt angle) and ϕ (azimuthal angle) are defined based on the presented methods in Figure 5.5 and 5.6.

Parameters	0.5 ML		1.0 ML
	CO1	CO1	CO2
C-O / Å	1.14	1.14	1.14
$x(\text{C}-\text{Ca}(\text{surface})) / \text{Å}$	0.04	0.06	0.05
$y(\text{C}-\text{Ca}(\text{surface})) / \text{Å}$	0.02	0.02	0.02
$z(\text{C}-\text{Ca}(\text{surface})) / \text{Å}$	2.78	2.78	2.79
$\text{Ca}(\text{surface})-\text{O}(\text{subsurface})$	2.33	2.33	2.33
$\Theta / (\text{deg})$	14.42	14.57	15.14
$\Phi / (\text{deg})$	36.49	36.18	38.34

Table 5.2 shows the predicted adsorption energies and stretching frequencies of CO molecules at various coverages. A stretch frequency of 2123 cm^{-1} was observed for the isolated CO gas phase molecule, indicating a frequency shift ($\Delta\nu$) of 20 cm^{-1} when compared to the experimental value of 2143 cm^{-1} ¹⁶⁶. Here, $\Delta\nu$ represents the calculated frequency shift relative to the computed stretching frequency of gas-phase CO, and ν (corrected) is obtained by adding this $\Delta\nu$ to the experimental CO gas-phase stretching frequency of 2143 cm^{-1} ¹⁶⁷.

When comparing experimental and theoretical results, we will utilize the relative shifts to the unbound molecule, $\Delta\nu$. The adsorption energy of a single CO molecule at 0.5 ML coverage is calculated to be -0.216 eV , and the CO stretching frequency is blue shifted by 27 cm^{-1} compared to the gas phase value. The binding energy is reduced to -0.210 eV for the whole monolayer, and the blue shift is reduced to 19 cm^{-1} .

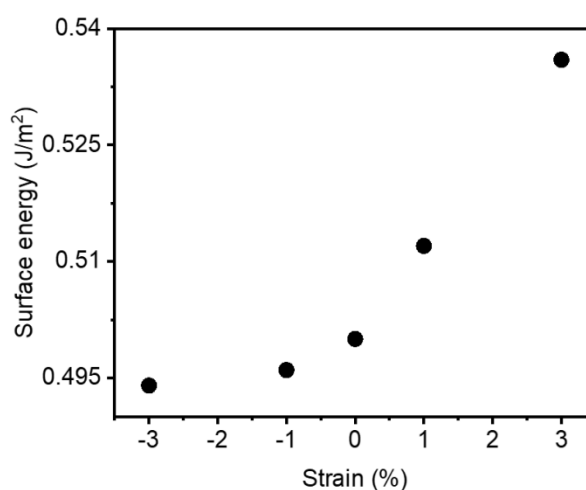
Table 5.2. Adsorption energy and vibrational frequencies as a function of surface coverage

CO Coverage / ML	$\Delta\nu$ Calculated / cm^{-1}	ν (corrected) / cm^{-1}	Measured Frequency / cm^{-1}	Calculated E_{ads} / eV	Measured E_{ads} / eV
0.5	27	2177	2175	-0.216	/
1.0	19	2161	2173	-0.210	-0.31

As with CO adsorption on other oxide surfaces, the reduced binding energy is ascribed to repulsive adsorbate–adsorbate interactions (e.g. TiO_2 ¹⁶⁶). When increasing exposures, the absence of attractive adsorbate–adsorbate interactions also explains why no islands occur. Because the overall blue shift (relative to the free molecule) is the result of a variety of causes, a simple rationalization of the changes in frequency between low and high coverage is challenging. (1) the CO dipole moment's interaction with the surface electric field (Stark effect), (2) the repulsive potential (Pauli repulsion) caused by the CO molecule vibrating against a rigid surface (also called wall effect)¹⁶⁵⁻¹⁶⁶. Intermolecular repulsive interactions, on the other hand, are consistent with NC-AFM results, which show no clustering of CO molecules.

5.4.2.2. CO adsorption on strained calcite(10.4)

We began by looking at the impact of strain on surface energy, which was computed using the Eq. (5.1). The surface energy of the unstrained system is 0.50 J/m^2 , which is quite close to previous predictions. Figure 5.7 depicts the surface energy results for all stretched and compressed surfaces. When uniaxial tensile strain is applied to samples, the surface energy increases. For example, 1% compressive strain yields $= 0.49 \text{ J/m}^2$, while 1% tensile strain yields $= 0.51 \text{ J/m}^2$. The stability of the calcite surface rises slightly with compression, according to the findings.

**Figure 5.7.** Change in surface energy of calcite(10.4) surface upon applying strain of 3%, 1%, -1% and -3%.

5.4.2.3. Effect of strain on CO adsorption

Finally, we study the effect of uniaxial external strain (1%, 3%, -1% and -3%) on the CO adsorption properties of calcite. The E_{ads} of CO molecule (half and full coverage) is calculated using the Eq. (5-2) and the results are shown in Table 5.3. For the considered the type of strain, the adsorption becomes more favorable as the surface stretched and compressed. The result of CO single molecule adsorption is compatible with the surface energy analysis as a surface is stretched further, i.e. the surface becomes less stable as it is stretched, implying that it will interact strongly with CO. The E_{ads} became more favorable with less compression applied, showing high stability of surface under compression. The effect of strain on adsorption is then discussed when full coverage is taken into account. The adsorption of the full coverage decreases compared to the single-molecule adsorption for example from 0.224 for single CO molecule to 0.221 for 1.0 ML when the sample stretched for 1 percent. Because the full coverage represents a more realistic depiction of the amount of gas present, a conclusion that carbon monoxide adsorption is affected by strain might be drawn; nonetheless, this effect is small (~ -0.01 eV).

Table 5.1. Adsorption energy and vibrational frequencies of unstrained and strained calcite(10.4) surfaces as a function of surface coverage.

Strain (%)	1CO			2CO		
	$\Delta\nu$ calculated /cm ⁻¹	ν (corrected) /cm ⁻¹	Calculated E_{ads} / eV	$\Delta\nu$ calculated /cm ⁻¹	ν (corrected) /cm ⁻¹	Calculated E_{ads} / eV
3%	43.5	2186.5	-0.227	34.5	2177.5	-0.225
1%	33.2	2176.2	-0.224	34.5	2177.5	-0.221
0	27	2170	-0.216	19	2162	-0.210
-1%	29.7	2172.7	-0.230	36.4	2179.4	-0.216
-3%	36.2	2179.2	-0.224	33.7	2176.7	-0.213

The strain dependency of CO vibrational frequencies is shown in Table 5.3. According to our calculations, a compressive or tensile strain that affects the lattice constant by 1 to 3% increase the frequency of adsorbed CO molecules. In comparison to unstrained calcite, the obtained blue-shifted vibrational frequencies on stretched calcite surfaces are perfectly consistent with the adsorption energies results. Full coverage has a larger effect on vibrational frequency than half coverage, but not by much, indicating that molecules are not situated in different binding locations (as shown in Figure 5.8). The influence of CO-CO interactions in vibrational frequencies is the dominant factor for 1.0 ML coverage, rather than the strain effect, which results in a redshift in CO vibrational frequency from 0.5 to 1.0 ML. We expected to acquire a greater value of frequency when less compression was applied to the surfaces based on surface energy data, but the opposite was found for half coverage. One possibility is that the reduced volume of the compressed cell has an influence on CO molecule vibration. The next step was to characterize the strain effect parameters of CO/strained-calcite(10.4). As shown in Figure 5.8 at 1 ML, the geometry of adsorbed CO molecules on strained calcites surfaces (stretched

or compressed) is the same as that of unstrained calcite (see Figure 5.6).

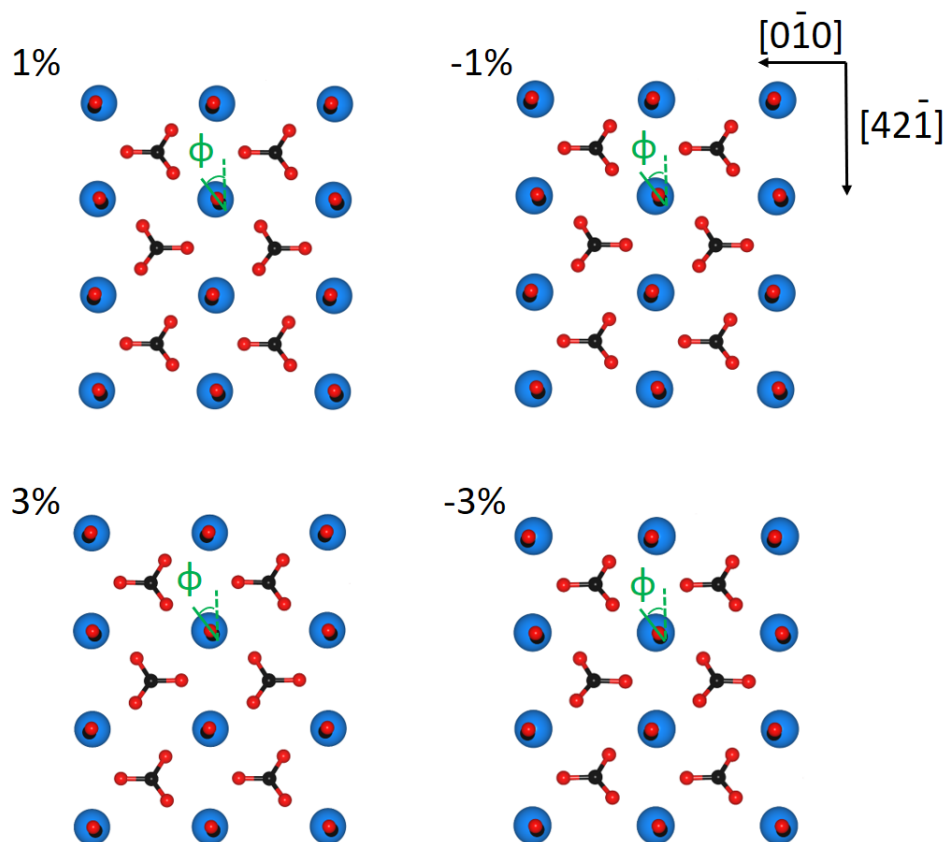


Figure 5.8. Full monolayer of CO on the energetically preferred adsorption site of a strained CaCO₃ surface. After their optimum configurations, ϕ denotes the azimuthal angle of adsorbed CO.

DFT optimization found a tilt of 14.42° for the single CO molecule within the (1×1) unstrained unit cell at 1 ML, while both stretched and compressed strain showed a declining trend, (Table 5.3 and 5.4). Data reveal that the more calcite surfaces are strained, the less CO molecules tilted on the surface relative to an unstrained surface for full coverage of CO molecules. The tilts of 13.33° and 13.18° for 3% stretched surfaces achieved for 1.0 ML, for example, were comparable with the tilts of 14.57° and 15.14° for the two CO molecules within the unstrained calcite. Probably showing a higher contact of adsorbed CO molecules with the stretched surface, confirming the adsorption energy data.

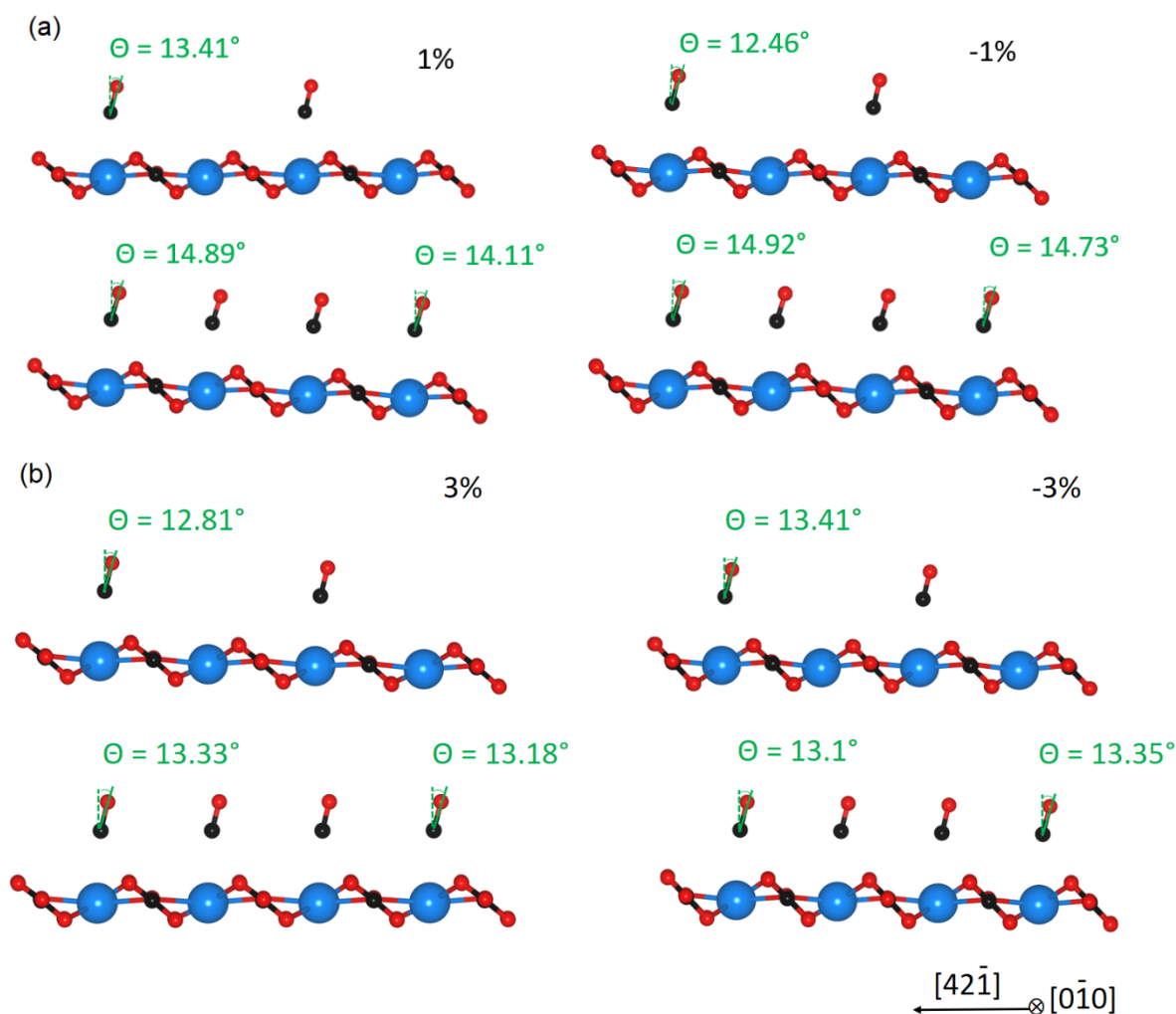


Figure 5.9. Side views of CO/strained calcite(10.4) after energy minimization for two different CO coverages of 0.5 ML and 1.0 ML (b, c). (a) shows the images for strained calcite surfaces by 1% and (b) indicates the images of calcite surfaces strained by 3%.

Table 5.2. Parameter characterization of CO/strained calcite(10.4) after geometry relaxation. The parameters $x(\text{C}-\text{Ca}(\text{surface}))$, $y(\text{C}-\text{Ca}(\text{surface}))$ and $z(\text{C}-\text{Ca}(\text{surface}))$ denote the distance between the carbon atom of the adsorbed CO molecule and the surface Ca ion. $\text{Ca}(\text{surface})-\text{O}(\text{subsurface})$ indicate the distance between the surface Ca ion and O presented in the sublayer. Θ (tilt angle) and Φ (azimuthal angle) are defined based on the presented methods in Figure 5.8 and 5.9a.

Parameters	1%		-1%			
	0.5 ML	1.0 ML	0.5 ML	1.0 ML		
C-O / Å	CO1	CO1	CO2	CO1	CO1	CO2
$x(\text{C}-\text{Ca}(\text{surface})) / \text{Å}$	1.14	1.14	1.14	1.14	1.14	1.14
$y(\text{C}-\text{Ca}(\text{surface})) / \text{Å}$	0.032	0.033	0.039	0.038	0.038	0.042
$z(\text{C}-\text{Ca}(\text{surface})) / \text{Å}$	0.018	0.018	0.018	0.025	0.017	0.016
$\text{Ca}(\text{surface})-\text{O}(\text{subsurface}) / \text{Å}$	2.77	2.80	2.79	2.81	2.77	2.78
$\text{Ca}(\text{surface})-\text{O}(\text{subsurface}) / \text{Å}$	2.35	2.35	2.35	2.36	2.35	2.35
$\Theta / (\text{deg})$	13.41	14.89	14.11	12.46	14.92	14.73
$\Phi / (\text{deg})$	34.10	33.1	28.83	34.79	32.1	31.41

Table 5.3. Parameter characterization of CO/strained calcite(10.4) after geometry relaxation. The parameters $x(\text{C-Ca}(\text{surface}))$, $y(\text{C-Ca}(\text{surface}))$ and $z(\text{C-Ca}(\text{surface}))$ denote the distance between the carbon atom of the adsorbed CO molecule and the surface Ca ion. $\text{Ca}(\text{surface})\text{-O}(\text{subsurface})$ indicate the distance between the surface Ca ion and O presented in the sublayer. Θ (tilt angle) and ϕ (azimuthal angle) are defined based on the presented methods in Figure 5.8 and 5.9b.

Parameters	3%			-3%		
	0.5 ML	1.0 ML		0.5 ML	1.0 ML	
	CO1	CO1	CO2	CO1	CO1	CO2
C-O / Å	1.14	1.14	1.14	1.14	1.14	1.14
$x(\text{C-Ca}(\text{surface})) / \text{Å}$	0.028	0.029	0.025	0.037	0.037	0.047
$y(\text{C-Ca}(\text{surface})) / \text{Å}$	0.017	0.018	0.015	0.021	0.021	0.022
$z(\text{C-Ca}(\text{surface})) / \text{Å}$	2.79	2.78	2.78	2.77	2.79	2.80
$\text{Ca}(\text{surface})\text{-O}(\text{surface})$	2.34	2.34	2.34	2.36	2.35	2.36
$\Theta / (\text{deg})$	12.81	13.33	13.18	13.4	13.1	13.35
$\phi / (\text{deg})$	36.95	36.40	33.54	32.31	33.43	31.14

5.5. CONCLUSION

The adsorption of CO molecules on freshly cleaved calcite(10.4) surfaces was investigated using polarization-resolved IRRAS and NC-AFM. The surface's structural quality was demonstrated by NC-AFM data. CO adsorption led in the appearance of dark features, which were mostly seen on top of light surface features. The surface Ca^{2+} cations were recognized as the latter. In agreement with the NC-AFM findings, IRRAS data obtained with p-polarized incoming light demonstrate that only one adsorbate species is present on the cleaved calcite(10.4) surface. CO adsorbed on the surface of calcite(10.4) was calculated using DFT for two distinct surface coverages (0.5 ML and 1.0 ML). CO adopts a slightly tilted geometry for the two different coverages evaluated here, according to the computations. A blue shift of the vibrational frequencies relative to the unbound molecule is obtained, as predicted by the IRRAS experiments. For 0.5 ML, the gap between observed and theoretical shifts is 2 cm^{-1} , indicating excellent agreement. The disparity between observed and predicted shifts grows to 12 cm^{-1} for 1.0 ML. The mismatch can be explained in part by a missing vdW-potential in the DFT functional. The predicted estimate of 0.210 eV for 1.0 ML adsorption energy is in good agreement with the observed value of 0.31 eV. Higher coverages (1.0 ML vs. 0.5 ML) resulted in lower binding energy, indicating the presence of repulsive interactions between neighboring CO adsorbates. This finding is consistent with NC-AFM data demonstrating that no CO islands have formed. We have studied how uniform strain in the plane parallel to the surface of calcite(10.4) affects the properties of adsorbed CO. The adsorption of CO molecule on calcite(10.4) surface under different external strain was studied. As the surface is stretched or compressed, the adsorption becomes more favorable. A compressive or tensile strain that changes the lattice constant by 1 to 3% increases the frequency of adsorbed CO molecules, according to our calculations. The reported blue-shifted vibrational frequencies on strained calcite surfaces are entirely consistent with the adsorption energies results when compared to unstrained calcite. Adsorbed CO molecules on strained calcites surfaces (stretched or compressed) have the same geometry as

normal calcite molecules. The more strained calcite surfaces are, the fewer CO molecules are tilted on the surface compared to an unstrained surface, according to the data. By quantifying the geomechanical impacts on the adsorbed gas, these data can be used to predict the projected ultimate recovery in carbonaceous tight gas reservoirs.

Chapter 6

6. MONITORING THE CRACK PROPAGATION IN CEMENT BASED MATERIALS WHILE BENDING TEST

The concept of this study was adapted from the published article: "Effect of polymer-coated silica particles in a Portland cement matrix via in-situ infrared spectroscopy" with permission from JOURNAL OF COMPOSITE MATERIALS.

6.1. Novelty of instrumental method

In engineering, knowing the exact properties of a material used in terms of strength, plasticity or brittleness, elasticity, and other properties is also critical. Material samples are tensile tested for this purpose by clamping them in a tensile testing system with a known starting cross-section and loading them with a tensile force. The force is then graphically represented as a function of the length change induced by ΔL ¹⁶⁸⁻¹⁶⁹. This curve is called the force-extension diagram. In this study, a new measurement approach based on in-situ infrared spectroscopy provides insight at the atomic level into various energy dissipation processes at cement-based materials.

6.2. The importance of energy dissipation in cement-based materials

At all times during the mechanical testing process, samples exchange energy with the surrounding environment. External mechanical energy is converted to strain energy, and the thermal energy is retained for use by the system (internal energy). Meanwhile, strain energy may be converted to elastic energy, surface energy, and other sources of energy, which are then released into the environment in various ways, such as acoustic emission and kinetic energy¹⁷⁰. As a result, energy is often transferred through the entire process of specimen deformation and destruction, which was detected in this study through bond vibrations¹⁷¹.

Many infrastructure structures, such as dams, road foundations, bridges, tunnels, and other structures, are made of concrete. As a result of impact loading or the dynamic shock of moving vehicles, earthquakes, and other causes, all of these concrete structures are exposed to vibration forces, resulting in structural damage and fatigue accumulation¹⁷²⁻¹⁷³. Two factors influence the amplitude and frequencies of induced vibration in a given structure: the structure form and the applied dynamic load. Vibrational control is important in this case for extending the structure's life and reducing costs¹⁷⁴⁻¹⁷⁵. One of the most important strategies for minimizing dynamic vibrations is damping, or the dissipation of energy in materials under load. Mechanical energy dissipation is the conversion of energy into another source of energy, such as heat¹⁷⁶. Vibration damping can be accomplished in two ways: passive damping and active damping. Active damping requires a sensor and actuator to overcome vibration, which is

efficient but expensive. Certain materials that can dissipate vibration energy and convert it to heat are used in passive damping (the cheapest and most popular method)¹⁷⁶.

6.3. Adding admixtures in cement-based materials

Polymers are commonly used in passive damping to minimize dynamic stress vibration and improve device efficiency¹⁷⁷⁻¹⁷⁹. The ability of polyethylene (PE) and polypropylene (PP) to resist impact deformation and dissipate impact energy was studied by Constantinides et al.¹⁸⁰. Finegan and Gibson¹⁸¹ studied the damping behavior of polymer composites with coated fibers, finding that coating the fiber with a viscoelastic polymer improves the damping properties significantly. Shape memory polymers are often referred to as smart materials because they can react to external stimuli such as heat, sound, and light¹⁸²⁻¹⁸³. The dissipation of vibration energy is affected by long-range molecular reordering during this reversible change. So, we aimed to use a series of polyurethane named PEG-MDI-DMPA (polyethylene glycol - 4,4-diphenylmethane diisocyanate - and dimethylolpropionic acid) which are known as a triple shape memory polymer⁷³. Gao et al.¹⁸⁴ discovered that grafting SiO₂ nanoparticles onto a rubbery block copolymer improved the epoxy matrix's ductility, fracture resilience, and fatigue crack growth resistance. To improve the mechanical properties of composites, Jiang et al.¹⁸⁵ suggested mixing silica nanoparticles with graphene oxide in epoxy.

6.4. General view

The aim of this research is to better understand the energy dissipation mechanisms in SiO₂@polymer–matrix composites so that damping behavior can be assessed. In this research, we used in-situ infrared spectroscopy in combination with a self-made mechanical instrument (Bieger) to apply external loads and IR radiation at the same time. The obtained IR spectra are expected to provide us with useful information about how modified samples respond to mechanical loading and their energy dissipation mechanism. The predicted role of particles in inhibiting crack propagation and rising energy dissipation of hardened cement paste is depicted in Figure 6.1.

6.5. Methodology

6.5.1. Chemicals

The SiO₂ powders (Silica gel 60, 0.03-0.2 mm) and Polyethylen glycol 1500 (PEG-1500) were purchased from Carl Roth GmbH & Co. KG, Germany. The Polyethylene glycol 600 (PEG-600), Diphenylmethane 4,40 -diisocyanate (MDI) and Sodium hydroxide solution (NaOH solution, 1 mol/L) were purchased from Merck KGaA, Germany. The 2,2-Bis(hydroxymethyl)-propionic acid (DMPA) was provided from Alfa Aesar, Germany. Portland cement (CEM-I 32.5 R) was supplied by HeidelbergCement AG, Germany.

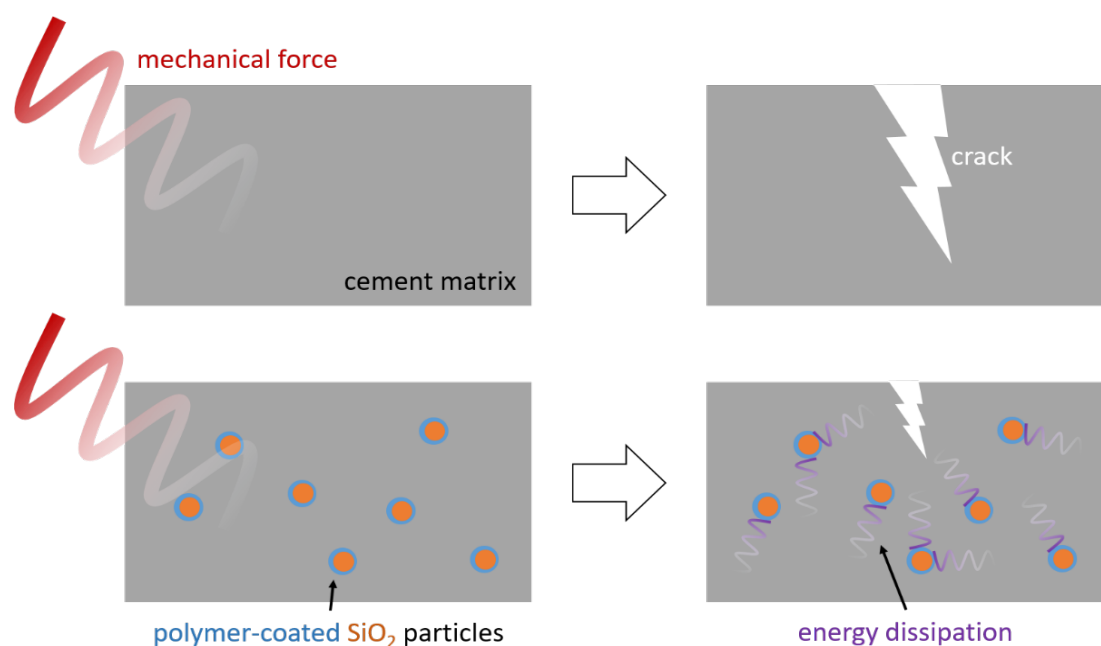


Figure 6.1. Schematic illustration of the effect of the particles on crack growth. It is believed that when mechanical force was applied to pure hardened cement paste, rapid crack propagation occurred, resulting in lower fracture force and abrupt mechanical force release. Incorporated particles, on the other hand, are supposed to act as a barrier to crack growth, resulting in the formation of new micro cracks that require energy to expand and move through the particles. As a result, more energy could be dissipated.

6.5.2. Preparation of polymer coated particles and cement-based composites

In this work, 0.015 mol PEG (PEG was PEG-600 and PEG-1500) and 0.012 mol DMPA were dissolved in 200 mL acetone, 9 g SiO₂ powders were added and dispersed by magnetic stirring for 10 min. After that, 0.025 mol MDI in 50 mL of acetone was added dropwise into above dispersion solution under a 750 r/min speed magnetic stirring, this mixture was heated to 75°C and reacted for 6 h under nitrogen protection. The products were filtrated and washed with acetone and deionized water. To improve the dispersity of the particles, the products were treated with NaOH solution for 30 min, then were filtrated again and washed with deionized water until the pH was. Polymer coated particles were obtained after 6 h of drying in oven at 50°C. The cement-based samples were prepared by first mixing the cement and each type of particles (with PEG-600 and PEG-1500), this mixture was stirred mechanically for 1 min. And then, under continuous stirring, water was added and the resulting mixture was mixed finally for 2 min (procedure in shown in Figure 6.2). And there was also a control sample without particles. For all of the samples, the water/cement ratio was 0.4 while the particle/cement ratio was 0.07. As the difference in modified samples comes from the molecular weight of PEG, the specimens are coded as PEG-i-C (i=molecular weight of PEG and C denoted the Cement matrix). Composition of three groups of pastes is shown in Table 6.1.

Table 6.1. Detailed information of mixture compositions.

Powder phase	Particle / cement	Water / cement	Aging time
CEM I 32.5R	0	0.4	28 days
PEG-600-C	0.07	0.4	28 days
PEG-1500-C	0.07	0.4	28 days

Due to declining the IR beam scattering, EcoMet 250 pro (Buehler) polisher was used to polish the cement-based materials. Micro polish aluminum oxide powder (alumina) was used at very fine grain size, as with 0.05 mm. The base-speed was 150 rpm, the load was 4 lbs and the polishing time was 2:00 minutes. Then, the polished specimens were cut, by means of IsoMet 1000 Precision Saw (Buehler) instrument, into rectangular samples with the size of 30 × 10 × 0.5 mm which is the required dimension for being used in our self-made mechanical device.

6.5.3. In-situ FTIR measurement

Fourier-Transform infrared spectroscopy (FTIR) combined with a three-point bending test. FTIR measurement (spectra from 400 to 4000 cm^{-1} , reflection mode), by VERTEX 70, and applying force in different positions was done simultaneously. In order to apply force on the samples, our self-made device (Bieger) was used (Figure 3.2(d)). The information regarding the applying strain was explained in Chapter 3 (section 3.2.1).

6.5.4. Scanning Electron Microscope (SEM) analysis

Surface morphology of samples before and after bending was analyzed by scanning electron microscopy using Philips XL30 ESEM-FEG (Firma, Ort, Land) at 20 kV.

6.5.5. Nanoindentation investigation

Proper surface preparation is crucial for nanoindentation analysis and therefore great care has been taken. Cross-section of the specimens were cut using a Buehler IsoMet 1000 diamond saw (Buehler, Lake Bluff, Illinois, USA). After epoxy-mounting three consecutive grinding steps followed by three consecutive polishing steps using a Buehler EcoMet 250 Pro Grinder Polisher were performed. In the last step a 50 nm alumina powder has been utilized. Each polishing step was followed by 3 min of ultrasonication in water with detergent to remove any loose particles. Nanoindentation was performed using an Ultra Nanoindentation Tester UNHT3 (Anton Paar GmbH, Graz, Austria) equipped with a diamond Berkovich tip. For each specimen a quadratic grid of 289 indents with a spacing of 10 mm between indents both in x and y direction was collected at a representative area. The applied load was increased for 10 s until the maximum load of 2 mN was reached and held for 5 s, followed by a 10 s unloading period. Young's modulus was then calculated using the Oliver and Pharr method. Since the diameter of the indents is only about 3 mm, different phases of the hardened cement paste with different Young's moduli were analyzed per specimen. Therefore, the standard deviation is large if only

the average of all these phases is given. Nevertheless, these values contain information about the average material properties.

6.6. Synthesis and characterization

The PEG-MDI-DMPA solution is synthesized through polymerization using poly ethylene glycol (PEG) with two molecular weights, 600 g mol^{-1} and 1500 g mol^{-1} , diphenylmethane diisocyanate (MDI) and dimethylolpropionic acid (DMPA). Figure 6.2 depicts the synthetic polymer's chemical structure. The designed polymer is successfully synthesized, according to IR results in Figure 6.3 (red line). The stretching vibration of isocyanate $N = C = O$ is estimated to be about 2270 cm^{-1} ¹⁸⁶. As can be shown, there is no peak at the wavenumber in question, suggesting that the MDI has completely reacted. The peaks observed around 3300 cm^{-1} and 1720 cm^{-1} are related to the stretching vibration of $N - H$ and $C = O$, respectively, illustrating the formation of the urethane group $(-NHCOO-)$ ^{73, 187}.

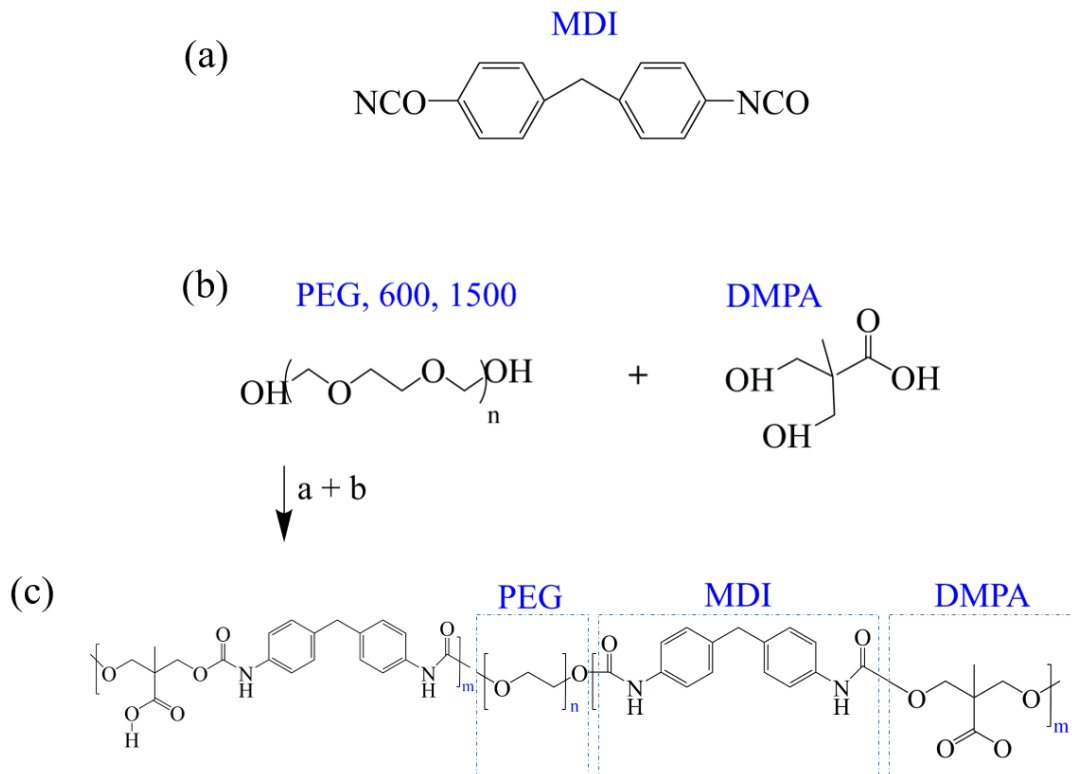


Figure 6.2. Synthetic process of polyethylene glycol - 4,4-diphenylmethane diisocyanate - and dimethylolpropionic acid (PEG-MDI-DMPA). Different molecular weight of (60 and 1500 g/mol) was used.

The stretching vibration of the $Si - O - Si$ bond occurs at 1088 cm^{-1} , 961 cm^{-1} , and 740 cm^{-1} in the green IR curve, indicating the range of the wavenumber region for SiO_2 particles. In addition, the peak around 461 cm^{-1} is associated with the bending vibration of $O - Si - O$ ¹⁸⁸. The determined range (black line) confirms that demonstrating whether SiO_2 and polymer are physically or chemically bound together is difficult. There is no obvious additional peak, such as

$Si - O - C$, that shows the formation of chemical interaction. However, due to contributions from several species, including $Si - O - Si$ and $Si - O - C$ vibrations, peak assignment at 1000- 1500 cm^{-1} is difficult ¹⁸⁹.

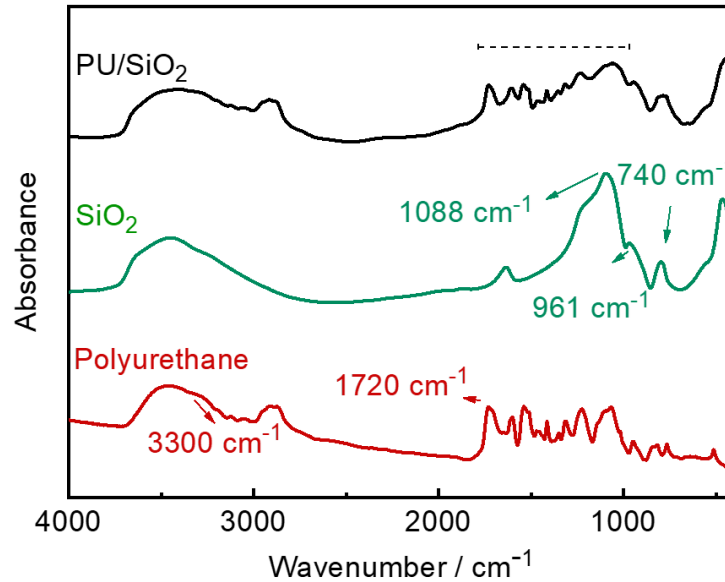


Figure 6.3. IR curves of synthetic polyurethane, SiO₂ particles and polyurethane coated SiO₂ particles (PU/SiO₂).

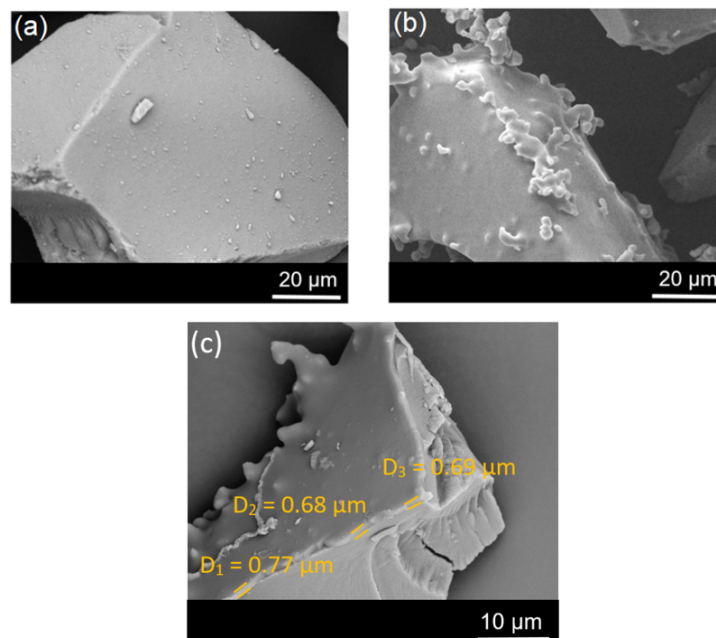


Figure 6.4. SEM images of (a): SiO₂ without polymer coating and (b): PU/SiO₂, the diameter of the inorganic core is between 5-250 microns and the thickness of the measured polymer coating for one of the particles is between 0.6 - 1 microns (c).

To learn more about the polymer coated particles and their distribution in the matrix, an EDX elemental mapping analysis is carried out (Figure 6.5). The findings show that Si is present in the heart and that the polymer is concentrated in the shell. The layer of polymer that restricted the agglomeration of SiO_2 particles may be responsible for the good distribution of Si in SiO_2 @polymer modified cement paste.

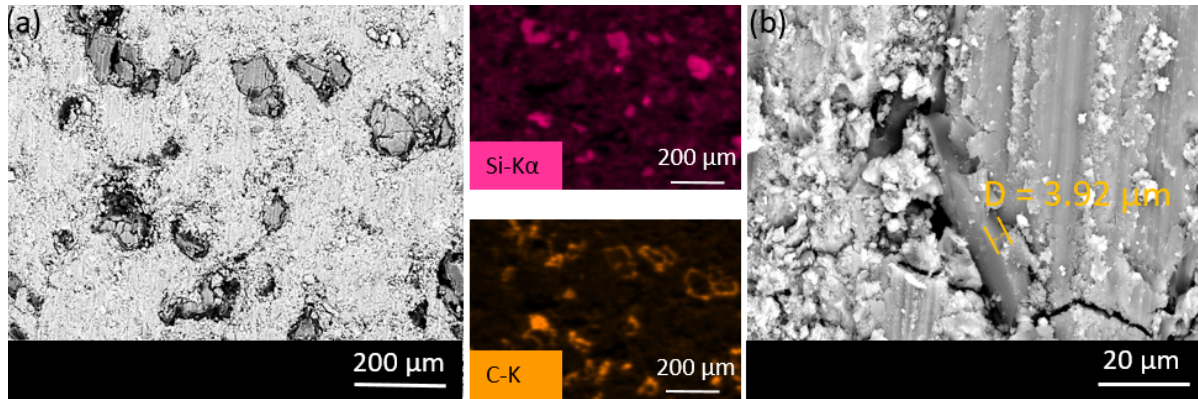


Figure 6.5. The results of SEM/EDX investigations of the C-PEG-600 after 28 days (the images are taken from cross section of sample). Individual elemental maps reveal the presence of silicon related to particles and carbon as cover around them. (b): higher magnification of SEM image which clearly indicates the existence of polymer coated compound in matrix, the measured polymer thickness is $3.92 \mu\text{m}$.

6.7. In-situ IR measurements during mechanical test

Figure 6.6 shows the IR spectra of samples under mechanical loading in various bending positions. Calcium silicate hydrate phases ($C - S - H$) make up about 60% of the hydration products in hardened cement paste, according to several previous reports, and have a major impact on mechanical properties¹⁹⁰⁻¹⁹². In addition, the $C - S - H$ structure is made up of stacking $Ca - O$ layers that are reinforced on both sides by silicate chains. The silicate tetrahedra can also be shown as dimers, dreierketten, or a chain of dreierketten. From a thermodynamic perspective, two hydrolytic reactions occur as the pure C-S-H phase undergoes the tensile process due to activation energy reductions (eq. (6-1) and (6-2))¹⁹³⁻¹⁹⁵. One is that in the presence of water, the ionic bonds between the Ca and $Si - O$ groups are stretched until they break, resulting in the formation of $Ca - OH$ and $Si - OH$. Another possibility is that the covalent $Si - O - Si$ bond will be elongated until it is broken, and the remaining $Si - O$ and Si will immediately react with water to form two $Si - OH$ (eq. 6-2).



The obtained IR results show that only reaction No. 6-2 occurs, implying that only the calcium silicate hydrate phase's silicate chains are affected (Figure 6.6). The energy was absorbed by stretching the $C - O$ bonds in the calcium silicate carbonate process and the $Si - O - Si$ bonds in the $C - S - H$ phase in pure cement (Figure 6.6). The layer structure of $C - S - H$ and calcium silicate carbonate phases is disrupted as the strain increases. They become

less organized, resulting in increased silicate tetrahedral breakage and rearrangements. The peaks at 1266 cm^{-1} and 1187 cm^{-1} are attributed to the antisymmetric stretching vibration of $\text{Si}-\text{O}-\text{Si}$.¹⁹⁶ The asymmetric and bending vibrations of the $\text{C}-\text{O}$ of the CO_3^{2-} group present in the calcium silicate carbonate process can be correlated to the sharp peak at 1582 cm^{-1} and a weak peak at 870 cm^{-1} , respectively¹⁹⁶⁻¹⁹⁷. The first mechanism of energy absorption is observed during stretching of $\text{C}-\text{O}$ bonds, since the material's damage process often begins with the weakest parts¹⁷¹.

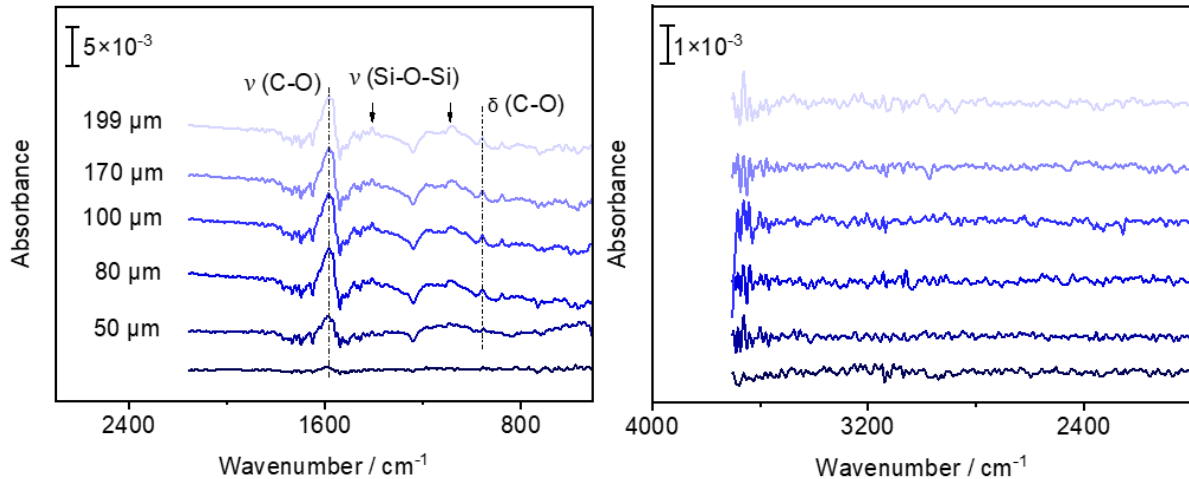


Figure 6.6. IR spectra of unmodified sample in different bending position. The value of deflection (d) for strain level is shown in μm . The black curve shows the zero position (deflection = 0). From up to down the value of curvature increase and the last spectra for each sample indicates the max deflection that is supported by samples before complete failure.

Carbonates are formed through a variety of processes, as discussed in the literature. The first mechanism involves CO_2 diffusing into the surface's empty pores, where it reacts with water from the pore solution to form carbonic acid. The formation of bicarbonate and carbonic ions results from the dissociation of carbonic acid. Calcium carbonate is formed as a result of the reaction between free Ca^{2+} ions and CO_3^{2-} . Furthermore, calcium ions from the calcium silicate hydrate ($\text{C}-\text{S}-\text{H}$) process can react with carbonate ions. The reaction of CO_2 with surface oxygen, which produces CO_3^{2-} , will initiate the second step, which will be followed by the reaction of CO_3^{2-} with calcium ions. Carbonate phase appears to develop on cement samples. Since IR measurements are performed in reflection mode, it's critical that the IR beam's penetration depth reaches the always carbonated surface so that enough data cannot be extracted from the bulk sample below. The FTIR findings (Figures 6.6, 6.7, and 6.8), as well as the observed variations in the presented peaks, suggest that the carbonate phase was not an obstacle to obtaining the desired information during the fracture process. First and foremost, the reaction process between particles and the cement matrix should be considered when considering the modified hardened cement paste. The nature of the interaction between the cementitious and polymeric phases is unknown, and it is a source of debate among

researchers. Some reported that only physical interaction occurs in the system. Other authors assert that physical and chemical interactions between polymers and Portland cement will occur. Chemical interaction, according to Janotka et al.¹⁹⁸, may lead to the formation of complex structures and changes in the hydration cement phases' morphology, composition, and quantity, especially calcium hydroxide.

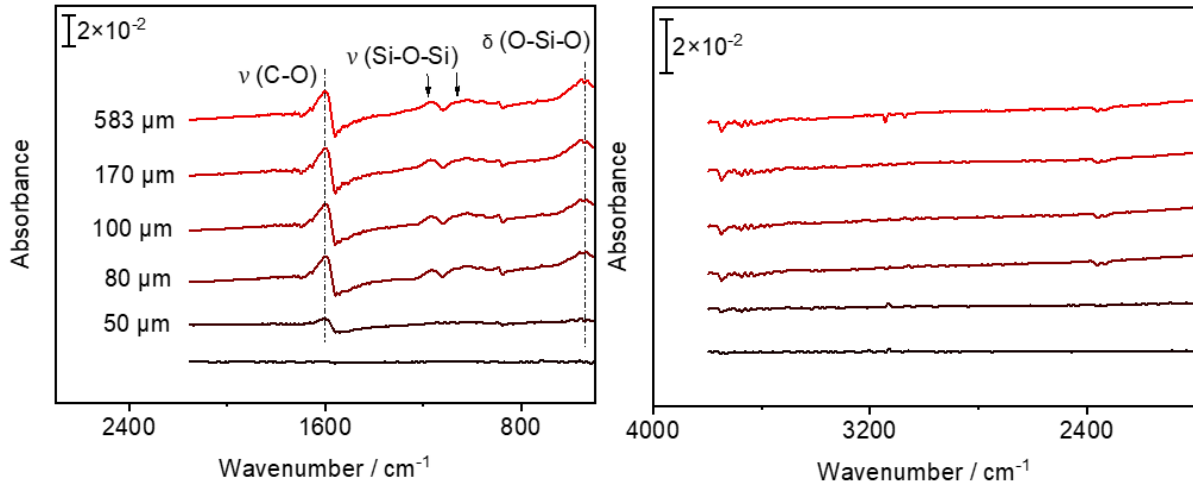


Figure 6.7. IR spectra of sample in various strain level for PEG-600-C. The black curve shows the zero position. The appearance of new peak (O-Si-O) is indication of different process of energy dissipation in the samples, contribution of SiO₂ particles.

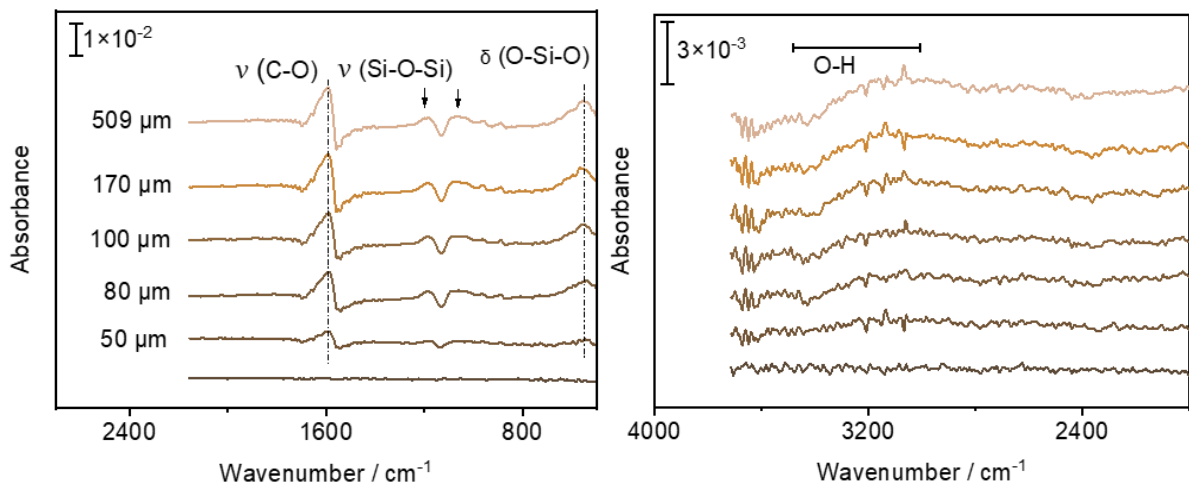


Figure 6.8. IR spectra of sample in various strain level for PEG-1500-C. The black curve shows the zero position. The appearance of new peak (O-Si-O) and (O-H) groups are indication of different process of energy dissipation in the samples.

Table 6-2 shows that the maximum deflection that the PEG-600-C sample can support is roughly three times that of pure hardened cement paste. These types of compounds (with physical or chemical interactions) tend to make the interlayer region in modified cement stronger than pure cement. Since the admixtures may act as nucleation sites for precipitating

cement hydration products, serving as a bridge between voids and cracks; or filler, filling the voids between the cement particles, thereby reducing the material porosity, the modified sample's mechanical strength has improved¹⁹⁹.

Table 6.2. The obtained values of max deflection (d) and max curvature supported by the samples. The value of ultimate force, stress and strain corresponding with max deflection for each sample are also calculated based on the presented formula in experimental part.

Samples	Young's modulus / GPa	Max d / μm	Max curvature / mm	Ultimate force / GPa mm ²	Final stress / GPa	Strain
CEM I 32.5R	9.18 \pm 3.6	199	564.7	8.46E-24	0.0007	0.0002
PEG-600-C	19.2 \pm 14.4	583	192.2	5.18E-23	0.027	0.0012
PEG-1500-C	33.9 \pm 36.8	509	220.6	8.00E-23	0.066	0.0022

As a function of pressure, Figure 6.9 depicts the intensity of energy consumed by various mechanisms. When the stretching vibration intensity of ($Si - O - Si$) is compared, it is clear that more $Si - O - Si$ bonds are involved in carrying out the strain in the modified cement. As a consequence, stress is distributed more evenly, and failure caused by strain concentration is reduced. This rise in intensity also means that the admixture effectively decreases the hydrolytic reaction's energy barrier (Eq. 6-2). Si is assumed to be vulnerable to separating from the $Si - O$ group and forming $2 Si - OH$ due to the coordination of carbon from the polymer's functional group¹⁹³. Furthermore, in contrast to cement without particles, the intensity of the $C - O$ bond connected to the calcium silicate carbonate process is enhanced in PEG-600-C (Figure 6.9). In comparison to the presented phase in pure hardened cement paste, it appears that the carbonate silicate phase in this sample is the weakest phase. One possibility is that the particles reduce the ability Ca^{2+} to bind with carbonate ions, making stretching of $C - O$ bonds in the carbonate silicate process of the PEG-600-C sample easier than in unmodified cement. As a consequence, particle incorporation increases the mechanical strength of cement by carrying more energy with $C - O$ bonds (dissipation of more energy). One notable feature of the IR spectra shown in Figures 6.7 and 6.8 is the presence of a peak about 500 cm^{-1} , which is most likely due to particle incorporation. The presented peak about 500 cm^{-1} is due to $O - Si - O$ bending vibrations, as shown in Figure 6.3 (black FTIR curve)¹⁸⁸. The emergence of this peak shows a new pathway of energy dissipation in the samples, which delays the final failure by preventing rapid stress decrease.

The first hypothesis was that the viscoelastic properties of the polymer process are primarily responsible for the energy dissipation of particles reinforced cement. The damping property of polymers is strongly temperature dependent, according to Sharafi et. al¹⁷⁸. Excessive viscoelastic motion of polymer chains, particularly near the glass transition temperature, is linked to increased damping capability. This could explain why there was no peak directly related to the polymeric phase in IR measurements of PEG-600-C. The broad peak is observed at the wavenumber 3400 cm^{-1} due to an increase in the molecular weight of PEG chains (PEG-

1500). It belongs to the $O - H$ vibrations and may indicate viscoelastic behavior in a polymer^{73, 187}. The PEG-MDI-DMPA triple shape memory consists of a soft segment (PEG chains) and a hard segment (MDI-DMPA). The presence of hydrogen bonding between PEG and the carboxyl group, which prevents PEG from crystallizing and increases the mobility of these chains, makes PEG a soft segment¹⁸⁷. The hard segment is made up of MDI and DMPA, and the dimers are mostly made up of carboxyl groups (found in the hard segment). In this polymeric structure, there are two types of hydrogen bonding interactions: one with themselves as dimers in the hard segment and the other with PEG in the soft segment (Figure 6.10(a) and (b)).

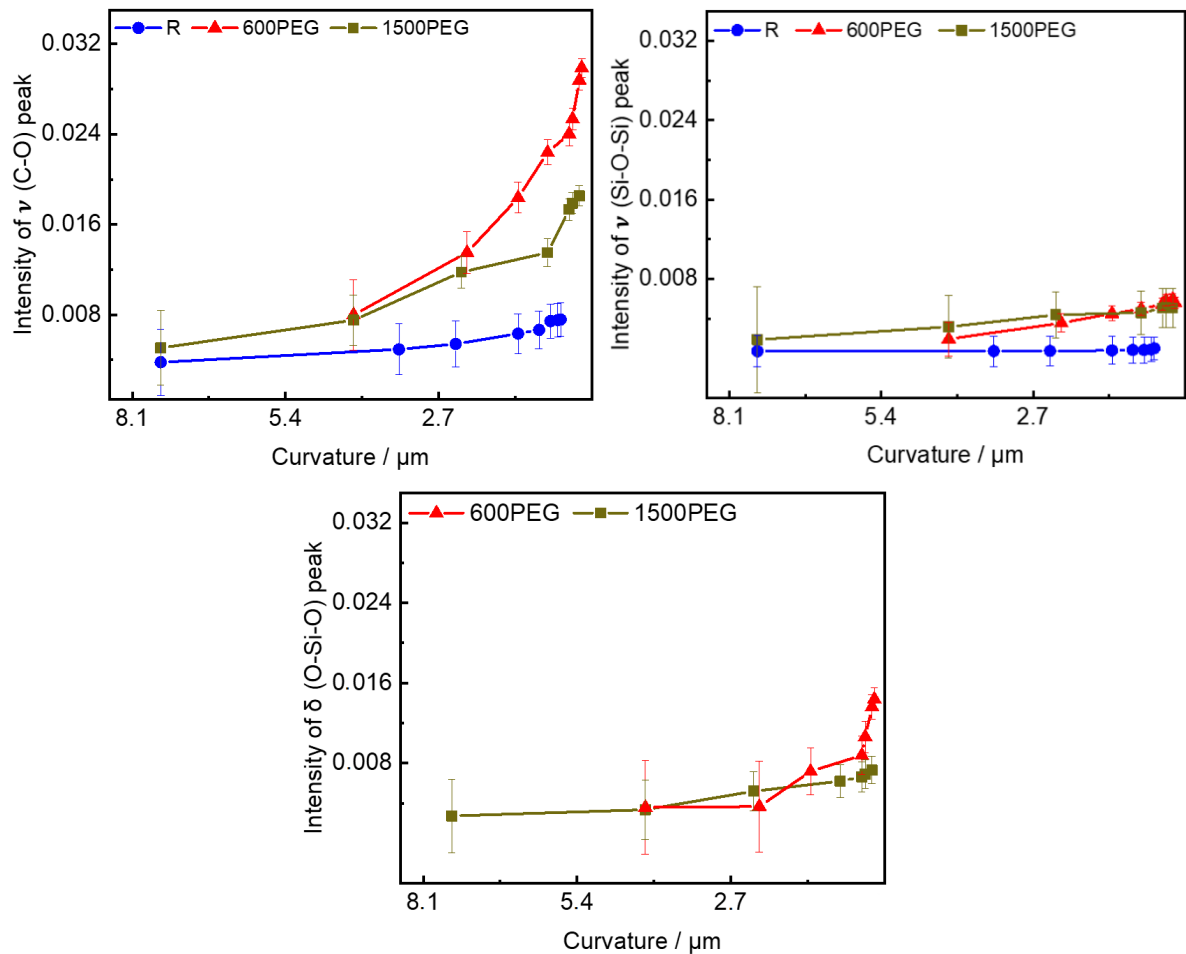


Figure 6.9. The measured intensity of the stretching vibration of (Si-O-Si), bending vibration of O-Si-O and C-O peaks of the CEM I 32.5R, PEG-600-C and PEG-1500-C as a function of curvature (μm). Each point represents one bending position when the samples undergo external mechanical force.

Increasing the molecular weight of PEG results in less MDI-DMPA segment content and less carboxyl groups in this polymer. As a result, increasing PEG chain length can result in more hydrogen bonding between PEG and carboxylic acid. Since the stretching vibration of $O - H$ is observed in the PEG-1500 sample, the corresponding peak is more likely to be correlated with the hydrogen bonding carboxyl groups and soft segment (not between two carboxylic groups).

As a result, some energy is consumed to stretch and sever the $O-H$ bonds¹⁸⁷. As a consequence of the improvements made to the chemical state of the PEG molecule, such as increasing the number of oxyethylene (OE) groups in the PEG chain and thus the number of hydrogenbondable groups, a new mechanism for dissipating strain energy has emerged. The linear relationship between the PEG molecular weight and the samples' young's modulus is shown in Table 6.2. As compared to PEG-600-C, the ultimate fracture force in PEG-1500-C is higher, owing to more interactions between the particles and the cement matrix. According to E. McNamee et al.²⁰⁰, the higher molecular weight of PEG causes entanglement of the PEG chains, resulting in a solid polymeric content (Figure 6.10(c)). Since the higher molecular weight of PEG causes higher cement strength as well as a new mechanism of energy dissipation, the polymer phase in the PEG-1500 sample is still sufficiently flexible to bend/flex for touching with the other surface. The argument is that as the length of the PEG chain grows longer, less energy is absorbed through other processes (especially at higher strain levels (Figure 6.9)). As the PEG molecular weight increases, a balance is achieved between overall deformation (toughness) and sample strength.

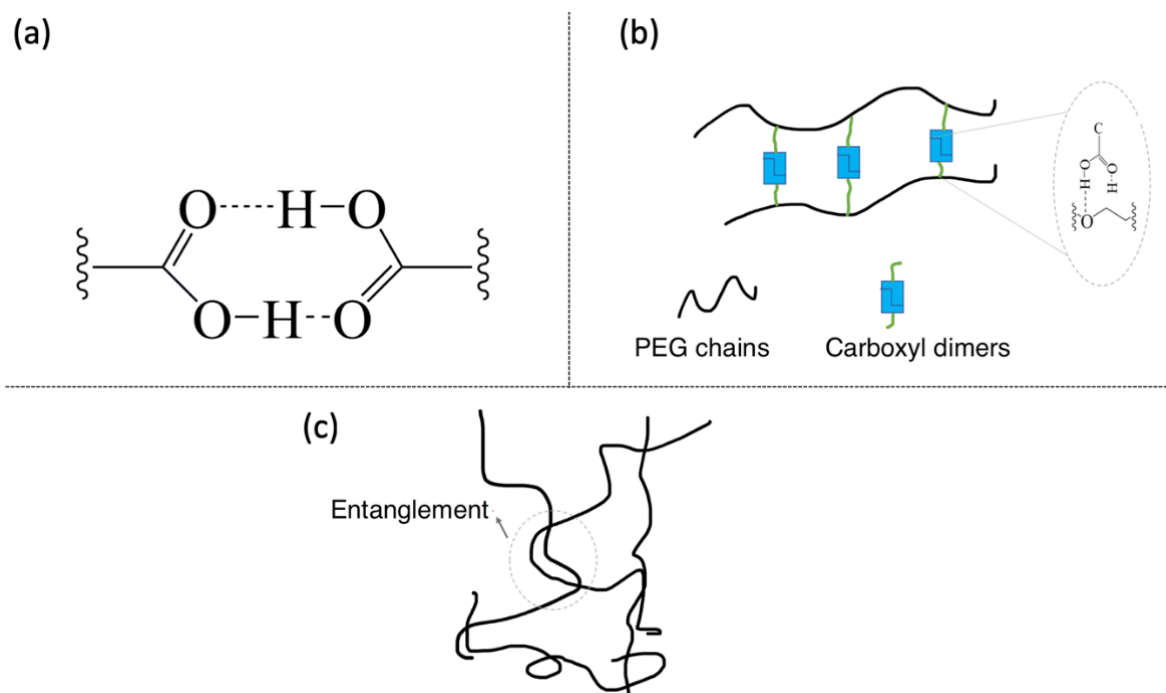


Figure 6.10. Two types of hydrogen bonding in PEG-MDI-DMPA. (a): hydrogen bonding between carboxylic acid, (b): hydrogen bonding between PEG and carboxyl group. Schematic illustration (c) shows PEG chain crosses and gets entanglement that might occurred with increasing the molecular weight of PEG.

6.8. Summary

The in-situ FTIR results show how the particles in the cement matrix increase the energy dissipation process and prevent the full release of strain energy, resulting in sample rupture. The $Si - O - Si$ and $C - O$ bonds were primarily responsible for dissipating energy in pure cement. The addition of particles lowers the hydrolytic reaction energy of $Si - O - Si$, allowing the modified samples to carry more energy. The existence of extra peaks associated with bending vibration of $O - Si - O$ and stretching of hydrogen bonds indicates that cement containing admixtures dissipated more energy through various mechanisms. Both ultimate load of failure and deformation increased in the same way from the unmodified sample to the cement with PEG-600 particles. Stretching the $O - H$ bonds induces a new mechanism for energy absorption when the molecular weight of the PEG is increased. PEG-1500-C also has a higher strength, which is likely due to a stronger interface bonding between the particles and the cement matrix. However, higher molecular weight of PEG decreased the overall deformation in this study. Therefore, there is a balance between the strength and deformation of cements with the molecular weight of PEG. In conclusion, since damping is a material's energy dissipation characteristic, it is possible to determine the damping property of samples subjected to external mechanical loading using FTIR results.

Chapter 7

7. CONCLUSION AND RECOMMENDATIONS

7.1. General Remarks

This thesis focused on atomic-scale investigation of strain effect on silicon and mineral materials (calcite and cement-based materials), in which the strain effect on surface reactivity for silicon wafers, CO adsorption parameters for calcite and monitoring the crack propagation for cement-based samples were our main concerns. In response to these goals, new mechanical machines were designed to investigate and provide the experimental data required to elucidate the necessary information. To in-situ track the strain-induced changes when applying force, these new devices were combined with IR spectroscopy and drop shape analyzer machines. The computational calculations (DFT) were performed with the aim of providing interpretation and guidance for performed experimental work. This thesis has provided a framework within which the strain effect on surface structure, adsorption properties, vibrational frequency and surface reactivity be investigated experimentally and computationally.

7.2. Research Objectives and Outcomes

In Section 1.2, a number of main research objectives were identified. Each of the objectives have been addressed in depth within the thesis and the following outcomes have been derived:

- (a) The following are the strain effects on H-Si microstructure: distribution of Si-H bonds (stretching and bending modes) and formation of new bonds (metastable three center (TCB)) due to hydrogen diffusion.
- (b) Strain demonstrates its ability to change the path way reaction of hydrogen terminated surface, resulting in a significant shift in the kinetic of surface reactions.
- (c) Direct formation of Si-OH linkages with substrate oxidation is produced upon the reaction between water and strained hydrogen terminated surface.
- (d) NC-AFM data demonstrate that CO adsorption on calcite(10.4) surface caused dark features to emerge on top of light surface features.
- (e) IRRAS data collected with p-polarized incoming light confirm the NC-AFM findings that just one adsorbate species is present on the cleaved calcite(10.4) surface.
- (f) According to the calculations, CO adopts a slightly tilted geometry for the two different coverages considered in this study.
- (g) The IRRAS experiments indicated a blue shift in vibrational frequencies of adsorbed CO on calcite(10.4) when compared to the unbound molecule.
- (h) Lower binding energy was observed at higher coverages (1.0 ML vs. 0.5 ML), showing the presence of repulsive interactions between nearby CO adsorbates.
- (i) The adsorption of CO molecules becomes more favorable as the calcite surface is stretched or compressed.

- (j) The reported blue-shifted vibrational frequencies on stained calcite surfaces are entirely consistent with the adsorption energies results when compared to unstrained calcite.
- (k) According to the findings, the more strained calcite surfaces are, the less CO molecules are tilted on the surface compared to an unstrained surface.
- (l) In-situ FTIR results show how the particles in the cement matrix increase the mechanism of energy dissipation process and prevent the full release of strain energy, resulting in sample rupture.
- (m) In the pure cement, $Si - O - Si$ and $C - O$ bonds were primarily responsible for dissipating energy.
- (n) The existence of extra peaks associated with bending vibration of $O - Si - O$ and stretching of hydrogen bonds indicates that cement containing admixtures dissipated more energy through various mechanisms.
- (o) Stretching the $O - H$ bonds induces a new mechanism for energy absorption when the molecular weight of the PEG is increased.
- (p) Since damping is a material's energy dissipation characteristic, it's possible to assess the damping property of samples subjected to external mechanical loading using FTIR results.

7.3. Recommendations and Scope for Future Research

Regarding H-silicon(111), in this study we investigate the strain effect on surface reactivity of hydrogenated Si(111). The Si(111) surface is the most suitable from a chemist's perspective because it has a large number of chemically distinct sites. The terrace site has an unstrained silicon monohydride termination, while the extremely distorted (112) step site has a silicon dihydride termination, and the strained and distorted silicon monohydride terminated kink site has a strained and distorted silicon monohydride termination. The mechanism of the rate-limiting step can also be inferred by correlating the structure of individual sites with their calculated reactivities. The theoretical work in this thesis is limited since only completely hydrogenated Si(111) is used as a model, and it is necessary to create the structure of H-Si(111) with defects as well. Furthermore, liquid water is used to investigate surface reactivity, but water vapors and oxygen are better candidates for bringing the experimental state closer to what occurs in the manufacturing or application lines of these samples. In the case of the cement-based samples, it's worth noting that as the hydration progressed, C-S-H gels, calcium hydroxide (CH), and ettringite (AFt) are expected to precipitate as the main hydrates in Portland cement. In this study (explained in chapter 6) the volume of different phases in pure cement and the modified samples is not calculated. As a result, the role of particles (SiO_2 @polymer) in hydrate formation could not be discussed in depth. Furthermore, in order to achieve the desired results after particle integration, a thorough analysis of the factors influencing particle distribution, particle-to-cement ratio, and various mixing processes is needed. In most cases of "sonochemistry", sound heats and compresses the system²⁰¹. The influence of sound on chemical reactions is difficult to explain using traditional explanations since sound frequency is low and stimulates phonons of long wavelength with little energy. These are unlikely to have

an impact on the rate of chemical reactions. As a result, it was hypothesized that the strain caused by the sound wave may play a role in the process. Strain effects are likely to have a role in supported catalysts, particularly those that use small clusters. When a cluster like this is deposited on a support, it undergoes two changes: a charge rearrangement and a geometric strain. As a result, it's probable that the strain is responsible for some of the change in catalytic activity generated by depositing clusters on an inert support. As a result, strain is an effect that can be seen in a wide range of occurrences.

REFERENCES

- (1) Thissen, P.; Seitz, O.; Chabal, Y. J. Wet chemical surface functionalization of oxide-free silicon. *Progress in Surface Science* 2012, 87 (9-12), 272-290, DOI: 10.1016/j.progsurf.2012.10.003.
- (2) Michalak, D. J.; Amy, S. R.; Aureau, D.; Dai, M.; Esteve, A.; Chabal, Y. J. Nanopatterning Si(111) surfaces as a selective surface-chemistry route. *Nature Materials* 2010, 9 (3), 266-271, DOI: 10.1038/nmat2611.
- (3) Batfalsky, P.; Haanappel, V. A. C.; Malzbender, J.; Menzler, N. H.; Shemet, V.; Vinke, I. C.; Steinbrech, R. W. Chemical interaction between glass-ceramic sealants and interconnect steels in SOFC stacks. *Journal of Power Sources* 2006, 155 (2), 128-137, DOI: 10.1016/j.jpowsour.2005.05.046.
- (4) Siddique, R.; Chahal, N. Use of silicon and ferrosilicon industry by-products (silica fume) in cement paste and mortar. *Resources Conservation and Recycling* 2011, 55 (8), 739-744, DOI:10.1016/j.resconrec.2011.03.004.
- (5) Yang, D. G.; Ernst, L. J.; van't Hof, C.; Kiasat, M. S.; Bisschop, J.; Janssen, J.; Kuper, F.; Liang, Z. N.; Schravendeel, R.; Zhang, F. Q. Vertical die crack stresses of Flip Chip induced in major package assembly processes. *Microelectronics Reliability* 2000, 40 (8-10), 1533-1538, DOI: 10.1016/s0026-2714(00)00156-6.
- (6) Shkarayev, S.; Savastiouk, S.; Siniaguine, O. Stress and reliability analysis of electronic packages with ultra-thin chips. *Journal of Electronic Packaging* 2003, 125 (1), 98-103, DOI: 10.1115/1.1535932.
- (7) Mercado, L. L.; Wieser, H.; Hauck, T. Multichip package delamination and the fracture analysis. *Transactions on Advanced Packaging* 2003, 26 (2), 152-159, DOI: 10.1109/tadvp.2003.817335.
- (8) Queeney, K.; Herbots, N.; Shaw, J. M.; Atluri, V.; Chabal, Y. Infrared spectroscopic analysis of an ordered Si/SiO₂ interface. *Applied physics letters* 2004, 84 (4), 493-495.
- (9) Weldon, M.; Queeney, K.; Chabal, Y.; Stefanov, B.; Raghavachari, K. Mechanistic studies of silicon oxidation. *Journal of Vacuum Science & Technology B: Microelectronics and Nanometer Structures Processing, Measurement, and Phenomena* 1999, 17 (4), 1795-1802.
- (10) Yen, J.-Y.; Hwu, J.-G. Enhancement of silicon oxidation rate due to tensile mechanical stress. *Applied Physics Letters* 2000, 76 (14), 1834-1835.
- (11) Wu, M.; Metiu, H. The effect of strain on the adsorption of CO on Pd(100). *The Journal of Chemical Physics* 2000, 113 (3), 1177-1183.
- (12) Morse, J. W.; Mackenzie, F. T. *Geochemistry of sedimentary carbonates*, Elsevier: 1990.
- (13) Tucker, M. E.; Wright, V. P. *Carbonate sedimentology*, John Wiley & Sons: 2009.
- (14) Wang, J.-J.; Zhu, J.-G.; Chiu, C.; Zhang, H. Experimental study on fracture toughness and tensile strength of a clay. *Engineering Geology* 2007, 94 (1-2), 65-75.
- (15) Ghosni, N.; Samali, B.; Vessalas, K. In Energy absorption and flexural toughness evaluation of fibre reinforced polymer modified concrete, *Proceedings of the 8th International Conference on Fracture Mechanics of Concrete and Concrete Structures (FraMCoS-8)*, 11-14 March, Toledo, Spain, 2013; pp 1122-1130.
- (16) Sun, Y.; Thompson, S. E.; Nishida, T. *Strain effect in semiconductors: theory and device applications*, Springer Science & Business Media: 2009.
- (17) Schaller, R. R. Moore's law: past, present and future. *spectrum* 1997, 34 (6), 52-59.
- (18) Chabal, Y. J. *Fundamental Aspects of silicon oxidation*. 2012.
- (19) Gokce, B.; Adles, E. J.; Aspnes, D. E.; Gundogdu, K. Measurement and control of in-plane surface chemistry during the oxidation of H-terminated Si(111). *Proceedings of the National Academy of Sciences* 2010, 107 (41), 17503-17508.
- (20) Bergfeld, S.; Braunschweig, B.; Daum, W. Nonlinear optical spectroscopy of suboxides at oxidized Si(111) interfaces. *Physical review letters* 2004, 93 (9), 097402.

- (21) Zhang, X.; Chabal, Y.; Christman, S.; Chaban, E.; Garfunkel, E. Oxidation of H-covered flat and vicinal Si(111)-1×1 surfaces. *Journal of Vacuum Science & Technology A: Vacuum, Surfaces, and Films* 2001, 19 (4), 1725-1729.
- (22) Juarez, M. F.; Patrino, E. M.; Paredes-Olivera, P. Quantum Mechanical Investigation of the Influence of the Local Environment on the Vibrational Properties of Hydrogenated Si(111). *The Journal of Physical Chemistry C* 2009, 113 (2), 681-690.
- (23) Soria, F. A.; Patrino, E. M.; Paredes-Olivera, P. Oxidation of hydrogenated Si(111) by a radical propagation mechanism. *The Journal of Physical Chemistry C* 2012, 116 (46), 24607-24615.
- (24) Schnur, S.; Groß, A. Strain and coordination effects in the adsorption properties of early transition metals. *Physical Review B* 2010 : 033402.
- (25) Pasco, R.; Ficalora, P. A work function-chemisorption study of hydrogen on iron: Kinetics and strain effects. In *Perspectives in Hydrogen in Metals*; Elsevier: 1986; pp 145-162.
- (26) Marjaoui, A.; Stephan, R.; Hanf, M.-C.; Diani, M.; Sonnet, P. Using strain to control molecule chemisorption on silicene. *The Journal of chemical physics* 2017, 147 (4), 044705.
- (27) Men, F.; Packard, W.; Webb, M. Si(100) surface under an externally applied stress. *Physical review letters* 1988, 61 (21), 2469.
- (28) Arrott, A.; Heinrich, B.; Purcell, S.; Legally, M. *Kinetics of Ordering and Growth at Surfaces*. 1990.
- (29) Sander, D.; Ibach, H. Experimental determination of adsorbate-induced surface stress: Oxygen on Si(111) and Si(100). *Physical Review B* 1991, 43 (5), 4263.
- (30) Grossmann, A.; Erley, W.; Ibach, H. Adsorbate-induced surface stress and surface reconstruction: oxygen, sulfur and carbon on Ni(111). *Surface science* 1995, 337 (3), 183-189.
- (31) Ibach, H. Adsorbate-induced surface stress. *Journal of Vacuum Science & Technology A: Vacuum, Surfaces, and Films* 1994, 12 (4), 2240-2245.
- (32) Grossmann, A.; Erley, W.; Hannon, J.; Ibach, H. Giant surface stress in heteroepitaxial films: invalidation of a classical rule in epitaxy. *Physical review letters* 1996, 77 (1), 127.
- (33) Gsell, M.; Jakob, P.; Menzel, D. Effect of substrate strain on adsorption. *Science* 1998, 280 (5364), 717-720.
- (34) Rodriguez, J. A.; Goodman, D. W. The nature of the metal-metal bond in bimetallic surfaces. *Science* 1992, 257 (5072), 897-903.
- (35) Madey, T.; Nien, C.-H.; Pelhos, K.; Kolodziej, J.; Abdelrehim, I.; Tao, H.-S. Faceting induced by ultrathin metal films: structure, electronic properties and reactivity. *Surface science* 1999, 438 (1-3), 191-206.
- (36) Larsen, J.; Chorkendorff, I. Increased dissociation probability of CH₄ on Co/Cu(111). *Surface science* 1998, 405 (1), 62-73.
- (37) Ratsch, C.; Seitsonen, A. P.; Scheffler, M. Strain dependence of surface diffusion: Ag on Ag(111) and Pt(111). *Physical Review B* 1997, 55 (11), 6750.
- (38) Reddy, M. S. Biomineralization of calcium carbonates and their engineered applications: a review. *Frontiers in microbiology* 2013, 4, 314.
- (39) Cölfen, H. Precipitation of carbonates: recent progress in controlled production of complex shapes. *Current opinion in colloid & interface science* 2003, 8 (1), 23-31.
- (40) Hlubina, P.; Urbańczyk, W. Dispersion of the group birefringence of a calcite crystal measured by white-light spectral interferometry. *Measurement Science and Technology* 2005, 16 (6), 1267.
- (41) Matter, J. M.; Kelemen, P. B. Permanent storage of carbon dioxide in geological reservoirs by mineral carbonation. *Nature Geoscience* 2009, 2 (12), 837-841.
- (42) Fleet, M. E.; Deer, W. A.; Howie, R. A.; Zussman, J. In *Rock-forming minerals: micas*, Geological Society of London: 1978.
- (43) Kerisit, S.; Parker, S. C.; Harding, J. H. Atomistic simulation of the dissociative adsorption of water on calcite surfaces. *Journal of Physical Chemistry B* 2003, 107 (31), 7676-7682, DOI: 10.1021/jp034201b.
- (44) Tasker, P. The stability of ionic crystal surfaces. *Journal of Physics C: Solid State Physics* 1979, 12 (22), 4977.

- (45) de Leeuw, N. H.; Parker, S. C. Surface structure and morphology of calcium carbonate polymorphs calcite, aragonite, and vaterite: an atomistic approach. *The Journal of Physical Chemistry B* 1998, 102 (16), 2914-2922.
- (46) Rahe, P.; Schütte, J.; Kühnle, A. NC-AFM contrast formation on the calcite(10.4) surface. *Journal of physics: condensed matter* 2012, 24 (8), 084006.
- (47) Al Siddiqi, A.; Dawe, R. A review of petroleum engineering aspects of Qatar's oil and gas. 1998.
- (48) Rybacki, E.; Evans, B.; Janssen, C.; Wirth, R.; Dresen, G. Influence of stress, temperature, and strain on calcite twins constrained by deformation experiments. *Tectonophysics* 2013, 601, 20-36.
- (49) Smith, S. A.; Nielsen, S.; Di Toro, G. Strain localization and the onset of dynamic weakening in calcite fault gouge. *Earth and Planetary Science Letters* 2015, 413, 25-36.
- (50) Jenkins, A.; Fathi, E.; Belyadi, F. Stress field behavior induced by hydraulic fracture in shale reservoirs: A practical view on cluster spacing. *Journal of Natural Gas Science and Engineering* 2017, 48, 186-196.
- (51) Higgins-Borchardt, S.; Sitchler, J.; Bratton, T. Geomechanics for unconventional reservoirs. In *Unconventional Oil and Gas Resources Handbook*; Elsevier: 2016; pp 199-213.
- (52) Rutter, E. H. The influence of temperature, strain rate and interstitial water in the experimental deformation of calcite rocks. *Tectonophysics* 1974, 22 (3-4), 311-334.
- (53) Turner, F. J.; Griggs, D. T.; Heard, H. Experimental deformation of calcite crystals. *Geological Society of America Bulletin* 1954, 65 (9), 883-934.
- (54) Elbashier, E.; Hussein, I.; Carchini, G.; Pour, A. S.; Berdiyrov, G. R. Effect of strain on gas adsorption in tight gas carbonates: A DFT study. *Computational Materials Science* 2021, 188, 110186.
- (55) Pang, B.; Zhang, Y.; Liu, G.; She, W. Interface properties of nanosilica-modified waterborne epoxy cement repairing system. *ACS applied materials & interfaces* 2018, 10 (25), 21696-21711.
- (56) Bimel, C.; Tipping, E.; Anderson, R. B.; Finkel, E. B.; Phelan, W. S.; Ault, C. M.; Foreman, B. E.; Phillips, D. W.; Ayers, C. M.; Fricks, T. J., Guide for concrete floor and slab construction. Report of the American Concrete Institute (ACI) committee: 1997.
- (57) Lewry, A.; Crewdson, L. Approaches to testing the durability of materials used in the construction and maintenance of buildings. *Construction and Building Materials* 1994, 8 (4), 211-222.
- (58) Woods, H. Durability of concrete construction. 1968.
- (59) Yang, Q.; Zhang, S.; Wu, X. Deicer-scaling resistance of phosphate cement-based binder for rapid repair of concrete. *Cement and concrete research* 2002, 32 (1), 165-168.
- (60) Al-Zahrani, M.; Maslehuddin, M.; Al-Dulaijan, S.; Ibrahim, M. Mechanical properties and durability characteristics of polymer-and cement-based repair materials. *Cement and Concrete Composites* 2003, 25 (4-5), 527-537.
- (61) Ding, H.; Xiang, R.; Song, Z. M.; Yu, Z. L. In Polymer/inorganic composite materials for quick repair of cement concrete pavement, *Materials science forum*, Trans Tech Publ: 2006; pp 614-617.
- (62) Ghosni, N.; Samali, B.; Valipour, H. In Flexural behaviour of high strength concrete composite incorporating long hooked-end steel fibres, *Proceedings of the 23rd Australasian Conference on the Mechanics of Structures and Materials (ACMSM23)*, Byron Bay, Australia, 9-12 December 2014; pp 327-332.
- (63) Bentur, A.; Mindess, S. *Fibre reinforced cementitious composites*, Crc Press: 2006.
- (64) Furlan Jr, S.; de Hanai, J. B. Shear behaviour of fiber reinforced concrete beams. *Cement and concrete composites* 1997, 19 (4), 359-366.
- (65) Chandra, S.; Flodin, P. Interactions of polymers and organic admixtures on portland cement hydration. *Cement and Concrete Research* 1987, 17 (6), 875-890.
- (66) Andayani, S. W.; Suratman, R.; Imran, I. Polymer Modified Concrete of Blended Cement and Natural Latex Copolymer: Static and Dynamic Analysis. *Open Journal of Civil Engineering* 2018, 8 (2), 205-220.
- (67) Wahby, W. Fifty Years'history Of Polymers In Concrete In Review. In: *Polymers In Concrete: The First Thirty Years*. Publication of: American Concrete Institute 2003.

- (68) Lendlein, A.; Kelch, S. Shape-memory polymers. *Angewandte Chemie International Edition* 2002, 41 (12), 2034-2057.
- (69) Kelch, S.; Steuer, S.; Schmidt, A. M.; Lendlein, A. Shape-memory polymer networks from oligo [(ϵ -hydroxycaproate)-co-glycolate] dimethacrylates and butyl acrylate with adjustable hydrolytic degradation rate. *Biomacromolecules* 2007, 8 (3), 1018-1027.
- (70) Dietsch, B.; Tong, T. A review-: Features and benefits of shape memory polymers (smgs). *Journal of advanced materials* 2007, 39 (2), 3-12.
- (71) Lewis, C. L.; Dell, E. M. A review of shape memory polymers bearing reversible binding groups. *Journal of Polymer Science Part B: Polymer Physics* 2016, 54 (14), 1340-1364.
- (72) Flory, P. J.; Rehner Jr, J. Statistical mechanics of cross-linked polymer networks I. Rubberlike elasticity. *The journal of chemical physics* 1943, 11 (11), 512-520.
- (73) Song, Q. J.; Chen, H. M.; Zhou, S. B.; Zhao, K. Q.; Wang, B. Q.; Hu, P. Thermo- and pH-sensitive shape memory polyurethane containing carboxyl groups. *Polymer Chemistry* 2016, 7 (9), 1739-1746, DOI: 10.1039/c5py02010g.
- (74) Nili, M.; Ehsani, A.; Shabani, K. In Influence of nano-SiO₂ and micro-silica on concrete performance, *Proceedings Second International Conference on Sustainable Construction Materials and Technologies*, 2010; pp 1-5.
- (75) Jo, B.-W.; Kim, C.-H.; Tae, G.-h.; Park, J.-B. Characteristics of cement mortar with nano-SiO₂ particles. *Construction and building materials* 2007, 21 (6), 1351-1355.
- (76) Givi, A. N.; Rashid, S. A.; Aziz, F. N. A.; Salleh, M. A. M. Experimental investigation of the size effects of SiO₂ nano-particles on the mechanical properties of binary blended concrete. *Composites Part B: Engineering* 2010, 41 (8), 673-677.
- (77) Dixit, P. M.; Dixit, U. S. Review of Stress, Linear Strain and Elastic Stress-Strain Relations. *Modeling of Metal Forming and Machining Processes: by Finite Element and Soft Computing Methods* 2008, 33-94.
- (78) Niwano, M.; Miura, T. a.; Miyamoto, N. Hydrogen Exchange Reaction on Hydrogen-Terminated Si(100) Surface during Storage in Water. *Journal of the Electrochemical Society* 1998, 145 (2), 659.
- (79) De Keyser, K.; Van Bockstael, C.; Detavernier, C.; Van Meirhaeghe, R.; Jordan-Sweet, J.; Lavoie, C. Epitaxial formation of a metastable hexagonal nickel-silicide. *Electrochemical and Solid State Letters* 2008, 11 (9), H266.
- (80) Weinberger, B.; Peterson, G.; Eschrich, T.; Krasinski, H. Surface chemistry of HF passivated silicon: X-ray photoelectron and ion scattering spectroscopy results. *Journal of applied physics* 1986, 60 (9), 3232-3234.
- (81) Burrows, V. YJ Chabal, GS Higashi, K. Raghavachari, and SB Christman. *Appl. Phys. Lett* 1988, 53, 998.
- (82) Ubara, H.; Imura, T.; Hiraki, A. Formation of Si-H bonds on the surface of microcrystalline silicon covered with SiO_x by HF treatment. *Solid State Communications* 1984, 50 (7), 673-675.
- (83) Imura, T.; Mogi, K.; Hiraki, A.; Nakashima, S.; Mitsuishi, A. Hydrogenated crystalline Silicon fabricated at low-substrate temperatures by reactive sputtering in He-H₂ atmosphere. *Solid State Communications* 1981, 40 (2), 161-164.
- (84) Trucks, G.; Raghavachari, K.; Higashi, G.; Chabal, Y. Mechanism of HF etching of silicon surfaces: A theoretical understanding of hydrogen passivation. *Physical review letters* 1990, 65 (4), 504.
- (85) De Gennes, P.-G.; Brochard-Wyart, F.; Quéré, D. *Capillarity and wetting phenomena: drops, bubbles, pearls, waves*, Springer Science & Business Media: 2013.
- (86) Nadkarni, G.; Garoff, S. An investigation of microscopic aspects of contact angle hysteresis: Pinning of the contact line on a single defect. *EPL (Europhysics Letters)* 1992, 20 (6), 523.
- (87) Onda, T.; Shibuichi, S.; Satoh, N.; Tsujii, K. Super-water-repellent fractal surfaces. *Langmuir* 1996, 12 (9), 2125-2127.
- (88) Young, T. III. An essay on the cohesion of fluids. *Philosophical transactions of the royal society of London* 1805, (95), 65-87.
- (89) Schrödinger, E. *Schrödinger 1926C. Annalen der Physik* 1926, 79, 734.

- (90) Hohenberg, P.; Kohn, W. Density functional theory (DFT). *Phys. Rev* 1964, 136, B864.
- (91) Kohn, W.; Sham, L. J. Self-consistent equations including exchange and correlation effects. *Physical review* 1965, 140 (4A), A1133.
- (92) Thomas, L. H. In *The calculation of atomic fields*, Mathematical proceedings of the Cambridge philosophical society, Cambridge University Press: 1927; pp 542-548.
- (93) Baseden, K. A.; Tye, J. W. Introduction to density functional theory: calculations by hand on the helium atom. *Journal of Chemical Education* 2014, 91 (12), 2116-2123.
- (94) Cramer, C. J. *Essentials of computational chemistry: theories and models*, John Wiley & Sons: 2013.
- (95) Clark, T. *A Handbook of computational chemistry; a practical guide to chemical and energy calculations*. 1985.
- (96) Cook, D. B. *Handbook of computational quantum chemistry*, Courier Corporation: 2005.
- (97) Kubicki, J. D.; Watts, H. D. Quantum mechanical modeling of the vibrational spectra of minerals with a focus on clays. *Minerals* 2019, 9 (3), 141.
- (98) Yamaguchi, Y.; Frisch, M.; Gaw, J.; Schaefer III, H. F.; Binkley, J. S. Analytic evaluation and basis set dependence of intensities of infrared spectra. *The Journal of chemical physics* 1986, 84 (4), 2262-2278.
- (99) Henkelman, G.; Uberuaga, B. P.; Jónsson, H. A climbing image nudged elastic band method for finding saddle points and minimum energy paths. *The Journal of chemical physics* 2000, 113 (22), 9901-9904.
- (100) Jónsson, H.; Mills, G.; Jacobsen, K. W. Nudged elastic band method for finding minimum energy paths of transitions. 1998.
- (101) Berne, B. J.; Ciccotti, G.; Coker, D. F. *Classical and quantum dynamics in condensed phase simulations: Proceedings of the International School of Physics*, World Scientific: 1998.
- (102) Sheppard, D.; Terrell, R.; Henkelman, G. Optimization methods for finding minimum energy paths. *The Journal of chemical physics* 2008, 128 (13), 134106.
- (103) Pratt, L. R. A statistical method for identifying transition states in high dimensional problems. *The Journal of chemical physics* 1986, 85 (9), 5045-5048.
- (104) Zweben, C.; Smith, W.; Wardle, M. In *Test methods for fiber tensile strength, composite flexural modulus, and properties of fabric-reinforced laminates*, Composite Materials: Testing and Design (Fifth Conference), ASTM International: 1979.
- (105) ASTM, I. *Standard test methods for plane-strain fracture toughness and strain energy release rate of plastic materials*. ASTM D5045-99 2007.
- (106) Jaccodine, R. J. Surface Energy Of Germanium And Silicon. *Journal of the Electrochemical Society* 1963, 110 (6), 524-527, DOI: 10.1149/1.2425806.
- (107) Messerschmidt, R. G.; Harthcock, M. A. *Infrared microspectroscopy. Theory and applications*. 1988.
- (108) Smith, B. C. *Fundamentals of Fourier transform infrared spectroscopy*, CRC press: 2011.
- (109) Kemp, W. *Organic spectroscopy*, Macmillan International Higher Education: 2017.
- (110) Bandyopadhyay, A.; Bose, S. *Characterization of biomaterials*, Newnes: 2013.
- (111) Hilal, N.; Ismail, A. F.; Matsuura, T.; Oatley-Radcliffe, D. *Membrane characterization*, Elsevier: 2017.
- (112) Tuttle, B.; Van de Walle, C. G. Structure, energetics, and vibrational properties of Si-H bond dissociation in silicon. *Physical review B* 1999, 59 (20), 12884.
- (113) Pankove, J. I.; Johnson, N. M. *Hydrogen in Semiconductors: Hydrogen in Silicon*. 1991.
- (114) Niwano, M.; Kageyama, J. i.; Kurita, K.; Kinashi, K.; Takahashi, I.; Miyamoto, N. Infrared spectroscopy study of initial stages of oxidation of hydrogen-terminated Si surfaces stored in air. *Journal of applied physics* 1994, 76 (4), 2157-2163.
- (115) Harp, G.; Han, Z.; Tonner, B. X-ray absorption near edge structures of intermediate oxidation states of silicon in silicon oxides during thermal desorption. *Journal of Vacuum Science & Technology A: Vacuum, Surfaces, and Films* 1990, 8 (3), 2566-2569.
- (116) Kamiura, Y.; Hasegawa, K.; Sano, Y.; Mizokawa, Y.; Kawamoto, K. Initial oxidation phenomena of heavily phosphorus-doped silicon in dry oxygen. *Journal of Vacuum Science & Technology B:*

- Microelectronics and Nanometer Structures Processing, Measurement, and Phenomena 2002, 20 (6), 2187-2191.
- (117) Morita, M.; Ohmi, T.; Hasegawa, E.; Kawakami, M.; Ohwada, M. Growth of native oxide on a silicon surface. *Journal of Applied Physics* 1990, 68 (3), 1272-1281.
- (118) Gokce, B.; Aspnes, D. E.; Lucovsky, G.; Gundogdu, K. Bond-specific reaction kinetics during the oxidation of Si(111): Effect of n-type doping. *Applied Physics Letters* 2011, 98 (2), 021904.
- (119) Kresse, G.; Furthmüller, J. Efficiency of ab-initio total energy calculations for metals and semiconductors using a plane-wave basis set. *Computational materials science* 1996, 6 (1), 15-50.
- (120) Joachim, P. The Perdew-Burke-Ernzerhof exchange correlation functional applied to the G2-1 test set using a plane-wave-basis set. *The Journal of chemical physics* 122.23 2005: 234102.
- (121) Perdew, J. P.; Burke, K.; Ernzerhof, M. Generalized gradient approximation made simple. *Physical review letters* 1996, 77 (18), 3865.
- (122) Kresse, G.; Joubert, D. From ultrasoft pseudopotentials to the projector augmented-wave method. *Physical review b* 1999, 59 (3), 1758.
- (123) Chadi, D. J.; Cohen, M. L. Special points in the Brillouin zone. *Physical Review B* 1973, 8 (12), 5747.
- (124) Mortazavi, B.; Rahaman, O.; Dianat, A.; Rabczuk, T. Mechanical responses of borophene sheets: a first-principles study. *Physical Chemistry Chemical Physics* 2016, 18 (39), 27405-27413.
- (125) Miura, T.-a.; Niwano, M.; Shoji, D.; Miyamoto, N. Initial stages of oxidation of hydrogen-terminated Si surface stored in air. *Applied surface science* 1996, 100, 454-459.
- (126) Darwich, R.; Cabarrocas, P. R. I.; Vallon, S.; Ossikovski, R.; Morin, P.; Zellama, K. Observation by infrared transmission spectroscopy and infrared ellipsometry of a new hydrogen bond during light-soaking of a-Si: H. *Philosophical Magazine B* 1995, 72 (3), 363-372.
- (127) Estreicher, S. Equilibrium sites and electronic structure of interstitial hydrogen in Si. *Physical Review B* 1987, 36 (17), 9122.
- (128) Deák, P.; Snyder, L. C.; Corbett, J. W. State and motion of hydrogen in crystalline silicon. *Physical Review B* 1988, 37 (12), 6887.
- (129) Van de Walle, C. G. Energies of various configurations of hydrogen in silicon. *Physical Review B* 1994, 49 (7), 4579.
- (130) Pajot, B.; Clerjaud, B.; Chevallier, J. Vibrational properties of hydrogen in compound semiconductors. *Physica B: Condensed Matter* 1991, 170 (1-4), 371-382.
- (131) Godet, C.; Schmirgeld, L.; Zuppiroli, L.; Sardin, G.; Gujrathi, S.; Oxorn, K. Optical properties and chemical reactivity of hydrogenated amorphous boron thin films. *Journal of materials science* 1991, 26 (23), 6408-6418.
- (132) Schaftenaar, G.; Noordik, J. H. Molden: a pre-and post-processing program for molecular and electronic structures. *Journal of computer-aided molecular design* 2000, 14 (2), 123-134.
- (133) Godet, C.; Roca i Cabarrocas, P. Role of Si-H bonding in Si:H metastability. *Journal of applied physics* 1996, 80 (1), 97-102.
- (134) Caudano, Y.; Thiry, P.; Chabal, Y. J. Investigation of the bending vibrations of vicinal H/Si(111) surfaces by infrared spectroscopy. *Surface science* 2002, 502, 91-95.
- (135) Watanabe, S.; Sugita, Y. Anisotropic dynamic polarization of surface vibrations associated with H on stepped Si(111). *Chemical physics letters* 1995, 244 (1-2), 105-110.
- (136) Zaibi, M.; Sebenne, C.; Lacharme, J. Temperature-Activated Reactions of H₂O and NH₃ with H-Passivated Si(111) Surfaces. *Surface Review and Letters* 2001, 25-31.
- (137) Michalak, D. J.; Amy, S. R.; Esteve, A.; Chabal, Y. J. Investigation of the chemical purity of silicon surfaces reacted with liquid methanol. *The Journal of Physical Chemistry C* 2008, 112 (31), 11907-11919.
- (138) Thissen, P.; Peixoto, T.; Longo, R. C.; Peng, W.; Schmidt, W. G.; Cho, K.; Chabal, Y. J. Activation of surface hydroxyl groups by modification of H-terminated Si(111) surfaces. *Journal of the American Chemical Society* 2012, 134 (21), 8869-8874.

- (139) Iftiqar, S. Structural studies on semiconducting hydrogenated amorphous silicon oxide films. *High Temperature Material Processes: An International Quarterly of High-Technology Plasma Processes* 2002, 6 (1).
- (140) Miura, T. a.; Niwano, M.; Shoji, D.; Miyamoto, N. Kinetics of oxidation on hydrogen-terminated Si(100) and (111) surfaces stored in air. *Journal of applied physics* 1996, 79 (8), 4373-4380.
- (141) Fuchs, F.; Schmidt, W.; Bechstedt, F. Understanding the optical anisotropy of oxidized Si(001) surfaces. *Physical Review B* 2005, 72 (7), 075353.
- (142) Rode, S.; Oyabu, N.; Kobayashi, K.; Yamada, H.; Kühnle, A. True atomic-resolution imaging of calcite(10.4) in aqueous solution by frequency modulation atomic force microscopy. *Langmuir* 2009, 25 (5), 2850-2853.
- (143) Schütte, J.; Rahe, P.; Tröger, L.; Rode, S.; Bechstein, R.; Reichling, M.; Kühnle, A. Clear signature of the (2× 1) reconstruction of calcite(10.4). *Langmuir* 2010, 26 (11), 8295-8300.
- (144) Raina, G.; Gauldie, R.; Sharma, S. K.; Helsley, C. E. A study of the calcite cleavage plane using the atomic force microscope. *Ferroelectrics Letters Section* 1994, 17 (3-4), 65-72.
- (145) Schütte, J.; Rahe, P.; Tröger, L.; Rode, S.; Bechstein, R.; Reichling, M.; Kühnle, A. Clear Signature of the (2 x 1) Reconstruction of Calcite(10.4). *Langmuir* 2010, 26 (11).
- (146) Stipp, S. L.; Hochella Jr, M. F. Structure and bonding environments at the calcite surface as observed with X-ray photoelectron spectroscopy (XPS) and low energy electron diffraction (LEED). *Geochimica et Cosmochimica Acta* 1991, 55 (6), 1723-1736.
- (147) Rachlin, A. L.; Henderson, G. S.; Goh, M. C. An atomic force microscope (AFM) study of the calcite cleavage plane: Image averaging in Fourier space. *American Mineralogist* 1992, 77 (9-10), 904-910.
- (148) Wöll, C. Structure and Chemical Properties of Oxide Nanoparticles Determined by Surface-Ligand IR Spectroscopy. *ACS Catalysis* 2019, 10 (1), 168-176.
- (149) Wang, Y.; Wöll, C. IR spectroscopic investigations of chemical and photochemical reactions on metal oxides: bridging the materials gap. *Chemical Society Reviews* 2017, 46 (7), 1875-1932.
- (150) Parlangeau, C.; Dimanov, A.; Lacombe, O.; Hallais, S.; Daniel, J.-M. Uniaxial compression of calcite single crystals at room temperature: insights into twinning activation and development. *Solid Earth* 2019, 10 (1), 307-316.
- (151) Tröger, L.; Schütte, J.; Ostendorf, F.; Kühnle, A.; Reichling, M. Concept for support and cleavage of brittle crystals. *Review of Scientific Instruments* 2009, 80 (6), 063703.
- (152) Barth, C.; Henry, C. R. Kelvin probe force microscopy on surfaces of UHV cleaved ionic crystals. *Nanotechnology* 2006, 17 (7), S155.
- (153) Giessibl, F. J. High-speed force sensor for force microscopy and profilometry utilizing a quartz tuning fork. *Applied Physics Letters* 1998, 73 (26), 3956-3958.
- (154) Bartels, L.; Meyer, G.; Rieder, K.-H. Controlled vertical manipulation of single CO molecules with the scanning tunneling microscope: A route to chemical contrast. *Applied Physics Letters* 1997, 71 (2), 213-215.
- (155) Troullier, N.; Jose Luis, M. Efficient pseudopotentials for plane-wave calculations. *Physical Review B* 1996.
- (156) Lardge, J. S.; Duffy, D. M.; Gillan, M. J. Investigation of the Interaction of Water with the Calcite (10.4) Surface Using Ab Initio Simulation. *Journal of Physical Chemistry C* 2009, 113 (17), 7207-7212, DOI: 10.1021/jp806109y.
- (157) Erica, B.; Marco, B.; Dino, A. Structure and adhesion energy of the calcite(10.4)/ice Ih(001) and baryte(210)/ice Ih(001) interfaces. *CrystEngComm* 2019, 21 (18), 2920-2928.
- (158) Fenter, P.; Sturchio, N. Calcite(10.4)-water interface structure, revisited. *Geochimica et Cosmochimica Acta* 2012, 97, 58-69.
- (159) Giraud, N.; Weidler, P. G.; Laye, F.; Schwotzer, M.; Lahann, J.; Wöll, C.; Thissen, P. Corrosion of Concrete by Water-Induced Metal-Proton Exchange. *Journal of Physical Chemistry C* 2016, 120 (39), 22455-22459, DOI: 10.1021/acs.jpcc.6b07347.

- (160) Bruno, M.; Bittarello, E.; Massaro, F.; Aquilano, D. The effect of impurities on the structure and energy of a crystal surface: Mg impurities in calcite as a case study. *CrystEngComm* 2018, 20 (32), 4556-4564.
- (161) Kerisit, S.; Parker, S. C.; Harding, J. H. Atomistic simulation of the dissociative adsorption of water on calcite surfaces. *The Journal of Physical Chemistry B* 2003, 107 (31), 7676-7682.
- (162) Sanna, S.; Schmidt, W. G.; Thissen, P. Formation of Hydroxyl Groups at Calcium-Silicate-Hydrate (C-S-H): Coexistence of Ca-OH and Si-OH on Wollastonite(001). *Journal of Physical Chemistry C* 2014, 118 (15), 8007-8013, DOI: 10.1021/jp500170t.
- (163) Redhead, P. Thermal desorption of gases. *Vacuum* 1962, 12 (4), 203-211.
- (164) Foster, A. S.; Shluger, A. L.; Nieminen, R. M. Quantitative modelling in scanning force microscopy on insulators. *Applied surface science* 2002, 188 (3-4), 306-318.
- (165) Pacchioni, G.; Ferrari, A. M.; Bagus, P. S. Cluster and band structure ab initio calculations on the adsorption of CO on acid sites of the TiO₂(110) surface. *Surface Science* 1996, 350 (1-3), 159-175, DOI: 10.1016/0039-6028(95)01057-2.
- (166) Ramalho, J. P. P.; Illas, F.; Gomes, J. R. B. Adsorption of CO on the rutile TiO₂(110) surface: a dispersion-corrected density functional theory study. *Physical Chemistry Chemical Physics* 2017, 19 (3), 2487-2494, DOI: 10.1039/c6cp06971a.
- (167) Setvin, M.; Buchholz, M.; Hou, W.; Zhang, C.; Stöger, B.; Hulva, J.; Simschitz, T.; Shi, X.; Pavelec, J.; Parkinson, G. S. A multitechnique study of CO adsorption on the TiO₂(101) anatase surface. *The Journal of Physical Chemistry C* 2015, 119 (36), 21044-21052.
- (168) Astm, I. ASTM E8/E8M-16a: Standard Test Methods for Tension Testing of Metallic Materials. West Conshohocken, PA, USA: ASTM International 2016.
- (169) Nádai, A.; Hodge Jr, P. Theory of Flow and Fracture of Solids, vol. II. 1963.
- (170) Li, W. M.; Xu, J. Y. Impact characterization of basalt fiber reinforced geopolymeric concrete using a 100-mm-diameter split Hopkinson pressure bar. *Materials Science and Engineering a-Structural Materials Properties Microstructure and Processing* 2009, 513-14, 145-153, DOI: 10.1016/j.msea.2009.02.033.
- (171) Lu, S.; Xu, J. Y.; Bai, E. L.; Luo, X. Effect of particles with different mechanical properties on the energy dissipation properties of concrete. *Construction and Building Materials* 2017, 144, 502-515, DOI: 10.1016/j.conbuildmat.2017.02.161.
- (172) Zheng, L.; Huo, X. S.; Yuan, Y. Experimental investigation on dynamic properties of rubberized concrete. *Construction and building materials* 2008, 22 (5), 939-947.
- (173) Shalchy, F.; Rahbar, N. Nanostructural characteristics and interfacial properties of polymer fibers in cement matrix. *ACS applied materials & interfaces* 2015, 7 (31), 17278-17286.
- (174) Li, W.-W.; Ji, W.-M.; Liu, Y.; Xing, F.; Liu, Y.-K. Damping property of a cement-based material containing carbon nanotube. *Journal of Nanomaterials* 2015, 16 (1), 418.
- (175) Ou, J. Structural Vibration Control-Active, Semi-Active and Smart Control Systems. Press of Science, China (in Chinese) 2003.
- (176) Han, S. J.; Chung, D. D. L. Mechanical energy dissipation using carbon fiber polymer-matrix structural composites with filler incorporation. *Journal of Materials Science* 2012, 47 (5), 2434-2453, DOI: 10.1007/s10853-011-6066-7.
- (177) Singh, R. K.; Kant, R.; Pandey, S. S.; Asfer, M.; Bhattacharya, B.; Panigrahi, P. K.; Bhattacharya, S. Passive vibration damping using polymer pads with microchannel arrays. *Journal of Microelectromechanical Systems* 2013, 22 (3), 695-707.
- (178) Sharafi, S.; Li, G. Q. Multiscale modeling of vibration damping response of shape memory polymer fibers. *Composites Part B-Engineering* 2016, 91, 306-314, DOI: 10.1016/j.compositesb.2015.12.046.
- (179) Geethamma, V.; Asaletha, R.; Kalarikkal, N.; Thomas, S. Vibration and sound damping in polymers. *Resonance* 2014, 19 (9), 821-833.
- (180) Constantinides, G.; Tweedie, C. A.; Holbrook, D. M.; Barragan, P.; Smith, J. F.; Van Vlietl, K. J. Quantifying deformation and energy dissipation of polymeric surfaces under localized impact.

- Materials Science and Engineering a-Structural Materials Properties Microstructure and Processing 2008, 489 (1-2), 403-412, DOI: 10.1016/j.msea.2007.12.044.
- (181) Finegan, I. C.; Gibson, R. F. Analytical modeling of damping at micromechanical level in polymer composites reinforced with coated fibers. *Composites science and technology* 2000, 60 (7), 1077-1084.
- (182) Hu, J. L.; Zhu, Y.; Huang, H. H.; Lu, J. Recent advances in shape-memory polymers: Structure, mechanism, functionality, modeling and applications. *Progress in Polymer Science* 2012, 37 (12), 1720-1763, DOI: 10.1016/j.progpolymsci.2012.06.001.
- (183) Hager, M. D.; Bode, S.; Weber, C.; Schubert, U. S. Shape memory polymers: Past, present and future developments. *Progress in Polymer Science* 2015, 49-50, 3-33, DOI: 10.1016/j.progpolymsci.2015.04.002.
- (184) Gao, J.; Li, J.; Zhao, S.; Benicewicz, B. C.; Hillborg, H.; Schadler, L. S. Effect of graft density and molecular weight on mechanical properties of rubbery block copolymer grafted SiO₂ nanoparticle toughened epoxy. *Polymer* 2013, 54 (15), 3961-3973.
- (185) Jiang, T.; Kuila, T.; Kim, N. H.; Ku, B.-C.; Lee, J. H. Enhanced mechanical properties of silanized silica nanoparticle attached graphene oxide/epoxy composites. *Composites Science and Technology* 2013, 79, 115-125.
- (186) Song, Q.; Chen, H.; Zhou, S.; Zhao, K.; Wang, B.; Hu, P. Thermo-and pH-sensitive shape memory polyurethane containing carboxyl groups. *Polymer Chemistry* 2016, 7 (9), 1739-1746.
- (187) Zhu, K.; Song, Q. J.; Chen, H. M.; Hu, P. Thermally assisted self-healing polyurethane containing carboxyl groups. *Journal of Applied Polymer Science* 2018, 135 (9), DOI: 10.1002/app.45929.
- (188) Oh, T.; Choi, C. K. Comparison between SiOC Thin Films Fabricated by Using Plasma Enhance Chemical Vapor Deposition and SiO₂ Thin Films by Using Fourier Transform Infrared Spectroscopy. *Journal of the Korean Physical Society* 2010, 56 (4), 1150-1155, DOI: 10.3938/jkps.56.1150.
- (189) Tian, R. H.; Seitz, O.; Li, M.; Hu, W. C.; Chabal, Y. J.; Gao, J. M. Infrared Characterization of Interfacial Si-O Bond Formation on Silanized Flat SiO₂/Si Surfaces. *Langmuir* 2010, 26 (7), 4563-4566, DOI: 10.1021/la904597c.
- (190) Mendoza, O.; Giraldo, C.; Camargo, S. S.; Tobon, J. I. Structural and nano-mechanical properties of Calcium Silicate Hydrate (C-S-H) formed from alite hydration in the presence of sodium and potassium hydroxide. *Cement and Concrete Research* 2015, 74, 88-94, DOI: 10.1016/j.cemconres.2015.04.006.
- (191) Kunther, W.; Lothenbach, B.; Skibsted, J. Influence of the Ca/Si ratio of the C-S-H phase on the interaction with sulfate ions and its impact on the ettringite crystallization pressure. *Cement and Concrete Research* 2015, 69, 37-49, DOI: 10.1016/j.cemconres.2014.12.002.
- (192) Lothenbach, B.; Nonat, A. Calcium silicate hydrates: Solid and liquid phase composition. *Cement and Concrete Research* 2015, 78, 57-70, DOI: 10.1016/j.cemconres.2015.03.019.
- (193) Zhou, Y.; Hou, D. S.; Geng, G. Q.; Feng, P.; Yu, J.; Jiang, J. Y. Insights into the interfacial strengthening mechanisms of calcium-silicate-hydrate/polymer nanocomposites. *Physical Chemistry Chemical Physics* 2018, 20 (12), 8247-8266, DOI: 10.1039/c8cp00328a.
- (194) Hou, D. S.; Zhao, T. J.; Ma, H. Y.; Li, Z. J. Reactive Molecular Simulation on Water Confined in the Nanopores of the Calcium Silicate Hydrate Gel: Structure, Reactivity, and Mechanical Properties. *Journal of Physical Chemistry C* 2015, 119 (3), 1346-1358, DOI: 10.1021/jp509292q.
- (195) Zhu, T.; Li, J.; Lin, X.; Yip, S. Stress-dependent molecular pathways of silica-water reaction. *Journal of the Mechanics and Physics of Solids* 2005, 53 (7), 1597-1623, DOI: 10.1016/j.jmps.2005.02.002.
- (196) Giraud, N.; Bergdolt, S.; Laye, F.; Krolla, P.; Lahann, J.; Thissen, P. Dehydration and dehydroxylation of C-S-H phases synthesized on silicon wafers. *Applied Surface Science* 2018, 433, 589-595, DOI: 10.1016/j.apsusc.2011.10.039.
- (197) Giraud, N.; Wohlgemuth, J.; Bergdolt, S.; Heinle, M.; Thissen, P. Passivation of Hydrated Cement. *Acs Sustainable Chemistry & Engineering* 2018, 6 (1), 727-737, DOI: 10.1021/acssuschemeng.7b03045.
- (198) Giraud, N.; Thissen, P. Carbonation Competing Functionalization on Calcium-Silicate-Hydrates: Investigation of Four Promising Surface-Activation Techniques. *ACS Sustainable Chemistry & Engineering* 2016, 4 (7), 3985-3994.

- (199) Sobolev, K.; Sanchez, F.; Vivian, I. In The use of nanoparticle admixtures to improve the performance of concrete, 12th International Conference on Recent Advances in Concrete Technology and Sustainability Issues. Ottawa, 2012; pp 455-469.
- (200) McNamee, C. E.; Yamamoto, S.; Higashitani, K. Effect of the physicochemical properties of poly (ethylene glycol) brushes on their binding to cells. *Biophysical journal* 2007, 93 (1), 324-334.
- (201) Suslick, K. S. *Sonochemistry*. *Science* 1990, 247 (4949), 1439-1445.
- (202) Mazzara, C.; Jupille, J.; Zheng, W.-Q.; Tanguy, M.; Tadjeddine, A.; Dumas, P. Hydrogen-terminated Si(111) and Si(100) by wet chemical treatment: linear and non-linear infrared spectroscopy. *Surface science* 1999, 427, 208-213.
- (203) Dumas, P.; Chabal, Y.; Jakob, P. Morphology of hydrogen-terminated Si(111) and Si(100) surfaces upon etching in HF and buffered-HF solutions. *Surface science* 1992, 269, 867-878.

APPENDIX

Appendix A: Additional information for chapter 4

The deconvolution of the FTIR spectra

All absorbance spectra are processed by subtracting IR spectrum of each sample after piranha cleaning and then by flattening the baseline to remove drifts. OPUS software was used to integrate the peak areas, and, when appropriate, peaks were fitted using Origin software. For the deconvolution of the spectra, OriginPro 2020b, a software peak analyzer tool (goal: Fit Peaks Pro; baseline mode: user defined; peak finding method: second derivative; fitting function: Lorentzian) was used on all the spectra. Data for the best fit to observed peaks in FTIR spectrum: wavenumbers (cm^{-1}), full-width at half maximum (FWHM) of the peaks from the Lorentz line shape, area and Height (H) are presented in below tables. For our data, manual baseline correction yields the best results. We picked points that define a new baseline and the baseline was composed of straight-line segments between these points. This baseline is subtracted from the spectrum to yield the baseline corrected spectrum. The method that we used for anchor points detection was 2nd-order derivative. All peaks of the 2nd-order derivative curve are found by the Local Maximum method. With the peaks of 2nd-order derivative in hand, we can adopt the points which lie closest to the peaks as anchor points.

1. Lorentzian deconvolution of Si-H stretching mode

The IR features and their assignments and hydrogen stretch modes are reported in Table A1. As shown in Figure 1, instead of sharp Si-H stretching mode around 2083.3 cm⁻¹, two additional frequencies are observed at ~2067 cm⁻¹ and ~2097 cm⁻¹. These modes, are assigned to the antisymmetric and symmetric, respectively, of coupled monohydride at steps of the Si(111) surface ($\nu_{as} = \sim 2065 \text{ cm}^{-1}$ and $\nu_{ss} = \sim 2097 \text{ cm}^{-1}$)²⁰²⁻²⁰³. The Si-H stretch spectrum is particularly sensitive to oxygen agglomeration into the first Si-Si bonds²¹. For the purposes of this research, we focused only on Si-H stretching vibration at 2083.3 cm⁻¹ (terrace monohydride stretching mode) to investigate the surface reactivity of our samples.

Table A1. Data for the best fit to the Si-H stretching mode in Figure 5a (main manuscript): wavenumber, full-width at half maximum (FWHM) of the peaks from the Lorentz line shape, Area, R-value and Height (H).

<i>Strain values</i>	<i>Wavenumber / cm⁻¹</i>	<i>FWHM</i>	<i>Area</i>	<i>R-Quadrat</i>	<i>H</i>
<i>Ref</i>	2067.04±0.53	7.5±1.68	6.15E-4±1.1E-4	0.99	5.2E-5
	2083.30±0.04	7.25±0.14	0.008±1.41E-4	0.99	7.0E-4
	2097.19±0.62	10.74±2.03	9.98E-4±1.6E-4	0.99	5.9E-5
<i>0.006%</i>	2097.34±0.82	16.24±2.3	0.002±3.6E-4	0.98	8.9E-5
	2082.73±0.15	10.71±0.69	0.005±3.9E-4	0.98	3.2E-4
	2069.05±0.59	9.05±1.9E-4	9.7E-4±2.0E-4	0.98	6.8E-5
<i>0.1%</i>	2098.53±0.62	16.38±1.9	0.0022±2.6E-4	0.98	8.5E-5
	2082.66±0.11	10.41±0.53	0.005±2.8E-4	0.98	3.1E-4
	2068.53±0.54	10.76±1.7	0.001±1.8E-4	0.98	6.9E-5
<i>0.3%</i>	2099.83±1.2	16.86±3.5	0.001±3.4E-4	0.98	5.1E-5
	2082.94±0.2	14.62±1.06	0.005±4.8E-4	0.98	2.5E-4
	2068.8±0.48	9.21±1.70	0.001±2.2E-4	0.98	7.2E-5
<i>0.5%</i>	2097.81±1.1	16.04±3.04	0.001±3.4E-4	0.97	6.0E-5
	2082.64±0.19	12.23±0.95	0.004±4.2E-4	0.97	2.4E-4
	2069.15±0.44	9.47±1.5	0.001±2.1E-4	0.97	8.5E-5
<i>1.0%</i>	2095.16±2.3	20.27±4.6	0.002±0.001	0.95	7.4E-5
	2081.74±0.69	16.15±4.1	0.003±0.001	0.95	1.5E-4
	2069.38±0.83	8.6±3.40	8.2E-4±4.7E-4	0.95	6.0E-5

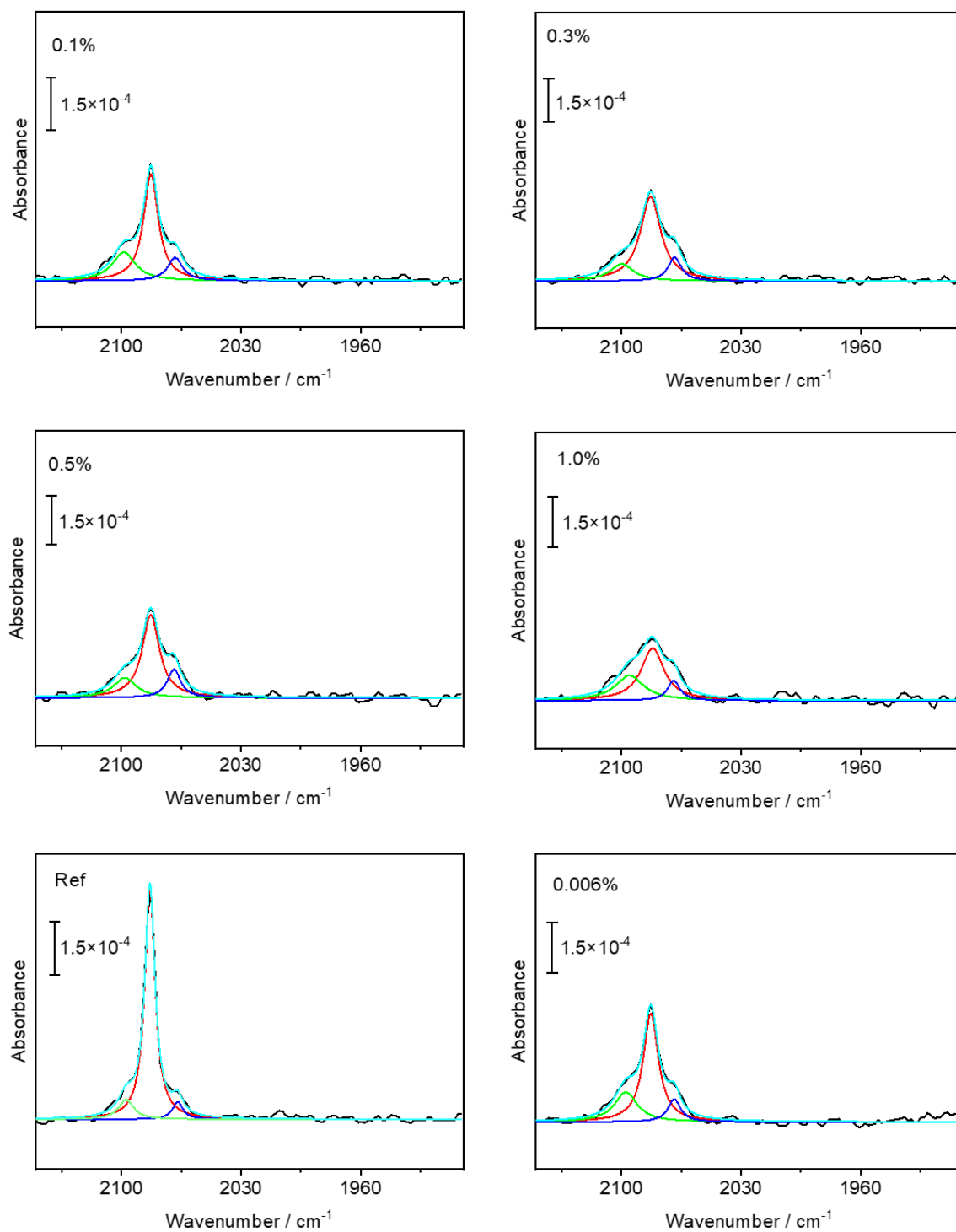


Figure A1. Lorentzian deconvolution of spectra of Si-H stretching mode before bending (Ref) and after mechanical test at the strain levels of (0.006-0.1-0.3-0.5 and 1.0)%.

2. Lorentzian deconvolution of Si-H-Si stretching mode

Table A2. Data for the best fit to stretching Si-H-Si mode in Figure 5a (main manuscript): wavenumber, full-width at half maximum (FWHM) of the peaks from the Lorentz line shape, Area, R-value and Height (H).

<i>Strain values</i>	<i>Wavenumber / cm⁻¹</i>	<i>FWHM</i>	<i>Area</i>	<i>R-Quadrat</i>	<i>H</i>
0.006%	1710.64±0.35	11.18±0.97	0.004±4.1E-4	0.95	2.5E-4
	1719.71±0.64	10.03±0.0	0.0018±2.8E-4	0.95	1.1E-4
	1737.02±0.26	14.35±0.5	-0.0057±0.0	0.95	-2.5E-4
0.1%	1710.5±0.27	10.72±0.81	0.003±3.1E-4	0.95	2.3E-4
	1720.99±0.56	12.26±0.0	0.0026±E-4	0.95	1.3E-4
	1736.47±0.30	14.95±0.0	-0.0039±E-4	0.95	-1.9E-4
0.3%	1711.14±0.25	11.76±0.73	0.004±2.17	0.96	2.3E-4
	1718.77±0.33	8.86±0.74	0.002±0.0	0.96	1.4E-4
	1737.15±0.27	12.61±0.89	-0.0036±2.1	0.96	-1.8E-4
0.5%	1710.66±0.27	11.31±0.84	0.006±4.8E-4	0.95	3.4E-4
	1722.3±0.51	9.51±1.7	0.002±4.6E-4	0.95	1.6E-4
	1736.11±0.31	11.82±0.59	-0.0045±0.0	0.95	-2.2E-4
1.0%	1710.02±0.27	9.9±0.0	0.009±4.0E-4	0.89	5.9E-4
	1723.68±0.36	7.89±1.17	0.004±5.5E-4	0.89	3.8E-4

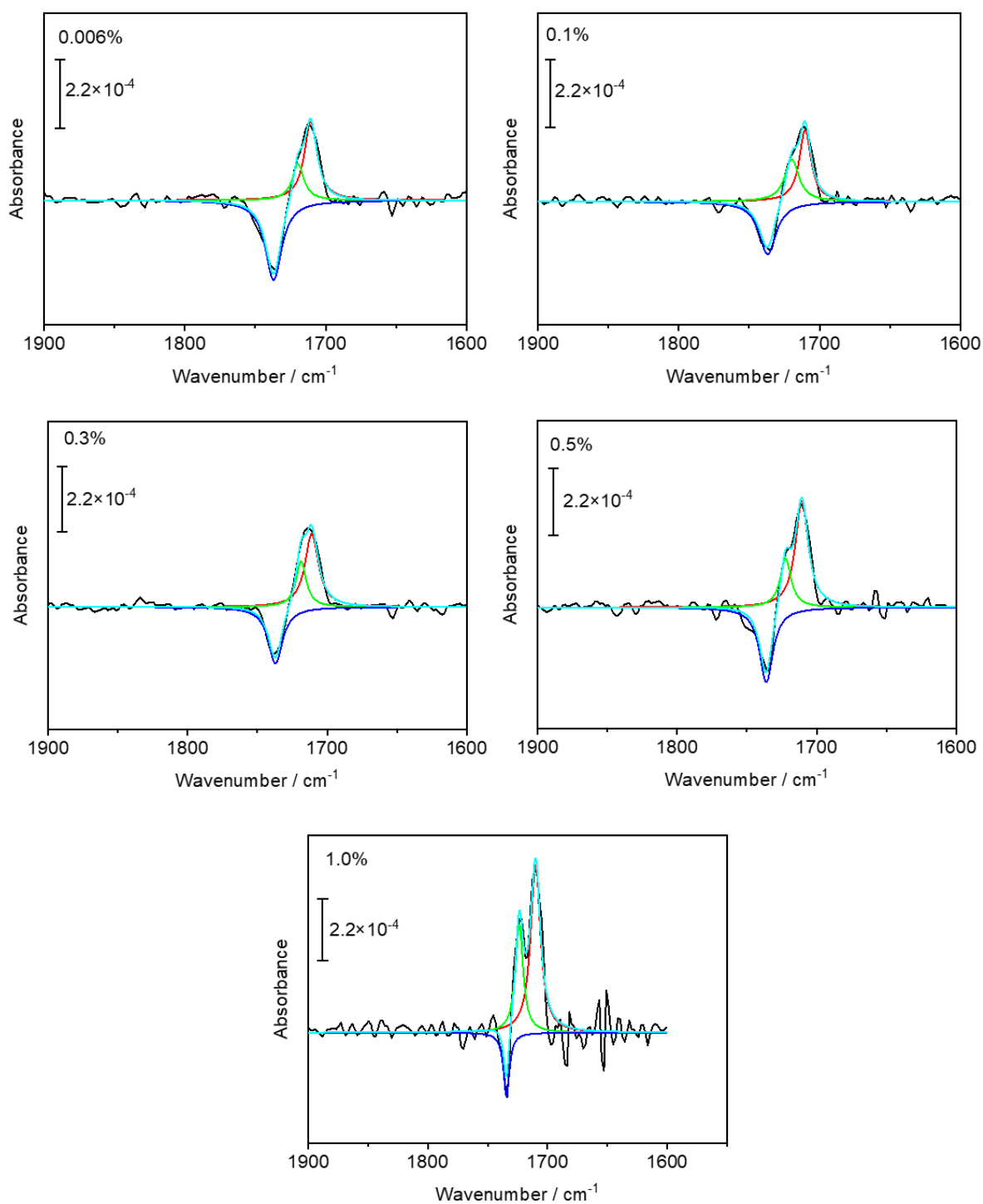


Figure A2. Lorentzian deconvolution of the peak related to Si-H-Si stretching band of strained H-Si(111) at the strain values of (0.006-0.1-0.3-0.5 and 1.0)%.

3. Lorentzian deconvolution of Si-H bending mode

Molden software was used to visualize the calculated infrared results presented in Figure 8e (main manuscript). The peak at 1915.0 cm^{-1} , as shown in Table 3, is related to the stretching mode of Si-H, which belongs to the Si-H-Si groups. The bending mode of the TCB metastable bond is higher in frequency than the bending mode of the up Si-H bonds, according to the findings. ($\delta_{\text{TCB}} = 640.644\text{ cm}^{-1}$ and $\delta = 622.39\text{ cm}^{-1}$).

Table A3. The calculated IR vibrations for the strained H-Si(111) model, containing TCB bond along the $[4\bar{4}\bar{1}]$ direction. The type of vibrations (ν : stretching and δ : bending) are determined using visualization software, molden.

<i>Wavenumber / cm⁻¹</i>	<i>Si-H band</i>	<i>Si-H-Si band</i>
2100.45	ν mode	
1915.06		ν mode
640.46		δ mode
622.39	δ mode	
619.83	δ mode	

Based on the above assumptions, and taking into account the fact that the band at 626.40 cm^{-1} is linked to the bending mode of Si-H (As the IR spectra are measured with resolution 4 cm^{-1} , variance in peak position with 2 cm^{-1} is reasonable), It's more likely that the measured bending peak at higher frequency for the strained sample is related to the bending mode of the Si-H-Si group.

Table A4. Data for the best fit to bending Si-H peak in Figure 5b (main manuscript): wavenumber, full-width at half maximum (FWHM) of the peaks from the Lorentz line shape, Area, R-value and Height (H).

<i>Lorentzian</i>	<i>Wavenumber / cm⁻¹</i>	<i>FWHM</i>	<i>Area</i>	<i>R-Quadrat</i>	<i>H</i>
Ref	629.65±1.3	4.02±2.2	0.011±0.1	0.98	0.0018
	626.40±0.5	4.69±2.1	0.017±0.03	0.98	0.0024
	622.49±1.1	0.0018	0.000±0.005	0.98	0.00
0.006%	627.64±1.1	4.6±2.2	0.02±0.02	0.98	0.0027
	624.12±1.5	4.8±1.6	0.014±0.009	0.98	0.0018
	620.18±1.9	5.2±3.5	0.009±0.001	0.98	0.0011
0.1%	631.22±0.2	4.2±1.1	0.01±1.5	0.98	0.0016
	627.51±0.8	4.5±0.9	0.02±1.5	0.98	0.0029
	624.37±1.1	4.5±0.6	0.016±3.5	0.98	0.0003
0.3%	631.59±0.7	4.2±0.6	0.014±3.5	0.98	0.0023
	629.68±0.9	4.7±0.4	0.009±2.5	0.98	0.0015
	627.70±0.3	4.3±1.1	0.008±1.2	0.98	0.0131
0.5%	633.02±1.2	4+ 2.4	0.016±0.01	0.99	0.0023
	630.57±1.1	4+11.5	0.020±0.7	0.99	0.0031
	627.69±0.5	4+9.3	0.002±0.06	0.99	0.0010
1.0%	632.26±1.1	7.8±5.5	0.051±0.01	0.99	0.0041
	626.05±1.5	5.5±6.4	0.021±0.005	0.99	0.0024
	618.31±0.8	4.5±2.2	0.007±0.003	0.99	0.0011

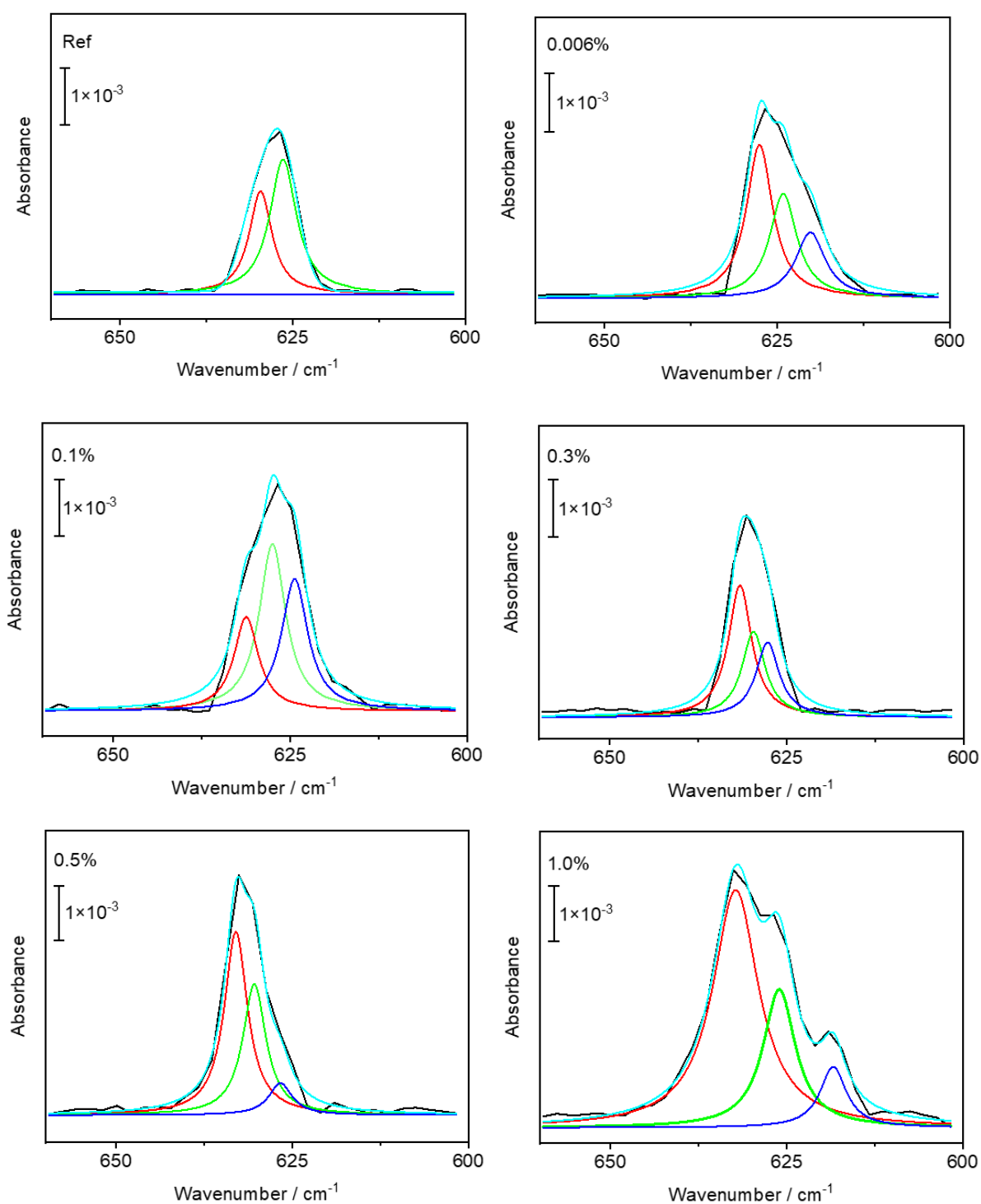


Figure A3. Lorentzian deconvolution of spectra of Si-H bending peak before (Ref) and after mechanical test at strain values of (0.006-0.1-0.3-0.5 and 1.0)%.

4. Three possibilities for the formation of Si-H-Si metastable bonds on ϵ -H-Si(111)

According to the explanations (section (I), main manuscript), it is concluded that the great strain-induced change is the hydrogen diffusion into Si-Si back bond. Therefore, three models can be studied in which strain is applied in direction of $[100]$ with different orientation of metastable Si-H-Si bonds in relation to directions of Si-Si back bonds; $[4\bar{4}\bar{1}]$, $[\bar{5}\bar{1}01]$ and $[\bar{1}0\bar{5}\bar{1}]$. These so-called path I, II, and III are shown schematically in Figure 4a-c with strain direction, possible direction of Si-H-Si group, and the angle between them. As shown, direction of Si-Si back bonds in path I and III are equivalent due to symmetry operation; belonging to the same family of direction.

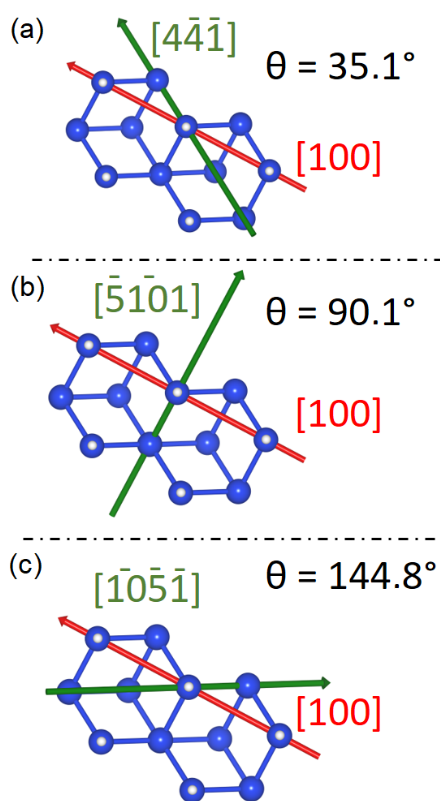


Figure A4. (a-c) Schematic representation of three models of ϵ -H-Si(111); red arrow shows the direction of strain and green arrow represents the orientation of Si-H-Si group. (a-c) Top view of part of models which are called as path I, path II and path III related to the orientation of Si-H-Si which is formed in directions of $[4\bar{4}\bar{1}]$, $[\bar{5}\bar{1}01]$ and $[\bar{1}0\bar{5}\bar{1}]$, respectively. Theta (θ) also indicate the angle between strain direction $[100]$ and Si-Si back bonds.

5. Lorentzian deconvolution of Si-OH bending mode

Table A5. Data for the best fit to the bending Si-OH mode in Figure 10b (main manuscript): wavenumber, full-width at half maximum (FWHM) of the peaks from the Lorentz line shape, Area, R-value and Height (H).

<i>Reaction time (min)</i>	<i>Wavenumber / cm⁻¹</i>	<i>FWHM</i>	<i>Area</i>	<i>R-Quadrat</i>	<i>H</i>
0.5	809.61	5.945	0.0021	0.94	2.2704E-4
	803.69	7.622	0.0044	0.94	3.7505E-4
	791.73	8.044	0.0049	0.94	3.9149E-4
	784.96	6.827	0.0056	0.94	5.2683E-4
	774.42	6.691E-4	1.5047E-4	0.94	1.5047E-4
2	808.96	7.658	0.0028	0.93	2.3728E-4
	803.38	7.413	0.0039	0.93	3.3528E-4
	791.71	7.906	0.0048	0.93	3.9400E-4
	784.98	6.692	0.0055	0.93	5.2737E-4
	774.56	4.593	8.0033E-4	0.93	1.1093E-4
5	787.72	17.672	0.0281	0.98	0.00101
	800.23	14.736	0.0133	0.98	5.7587E-4
	811.06	15.636	0.0140	0.98	5.7266E-4
	824.66	12.384	0.0124	0.98	6.4028E-4
	837.13	7.964	0.0026	0.98	2.0925E-4
10	789.21	19.797	0.0340	0.98	0.0011
	798.87	10.482	0.0112	0.98	6.8096E-4
	809.99	8.657	0.0123	0.98	9.0920E-4
	821.52	11.909	0.0167	0.98	8.9401E-4
	834.31	12.351	0.0060	0.98	3.1292E-4
20	790.29	17.289	0.0449	0.98	0.0016
	800.00	9.250	0.0085	0.98	5.93E-4
	810.56	11.716	0.0165	0.98	8.93E-4
	822.32	14.342	0.0160	0.98	7.7701E-4
	835.18	18.288	0.0138	0.98	4.8456E-4

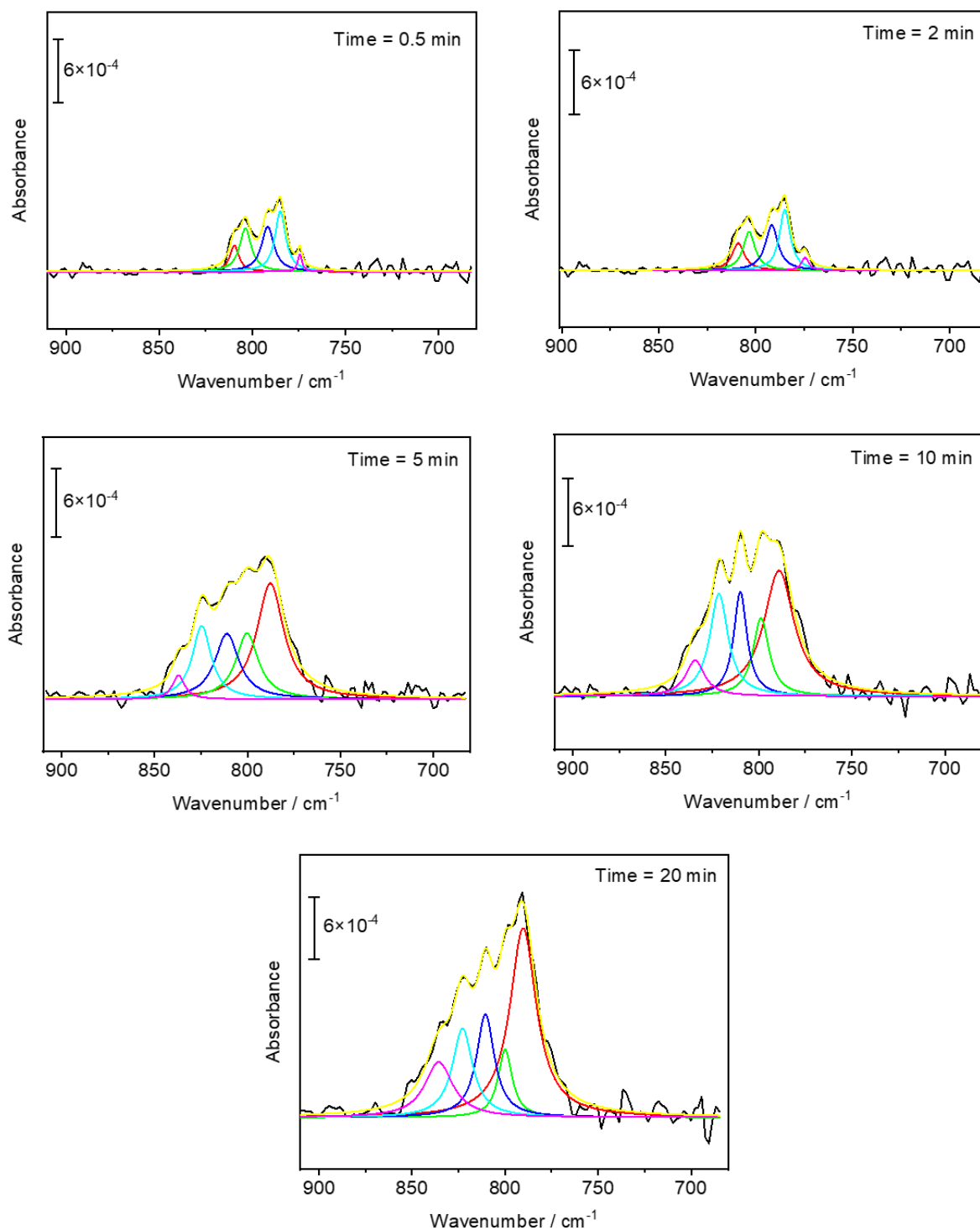


Figure A5. Lorentzian deconvolution of spectra of Si-OH bending mode of strained H-Si(111) (strain level = 0.3%) in different reaction times with water.

6. Lorentzian deconvolution of Si-O-Si modes

Table A6. Data for the best fit to the stretching Si-O-Si modes in Figure 10c (main manuscript): wavenumber, full-width at half maximum (FWHM) of the peaks from the Lorentz line shape, Area, R-value and Height (H).

<i>Reaction time (min)</i>	<i>Wavenumber / cm⁻¹</i>	<i>FWHM</i>	<i>Area</i>	<i>R-Quadrat</i>	<i>H</i>
5	1234.59	29.380	0.365	0.99	0.0079
	1209.48	43.328	0.396	0.99	0.0058
	1162.00	74.329	0.481	0.99	0.0041
	1056.65	88.988	0.644	0.99	0.0046
10	1232.80	34.225	0.903	0.99	0.0168
	1204.51	43.737	0.610	0.99	0.0088
	1156.69	74.148	0.820	0.99	0.0070
	1058.77	81.510	1.057	0.99	0.0082
20	1235.58	28.030	0.728	0.98	0.0165
	1210.60	43.935	0.761	0.98	0.0110
	1156.82	80.430	0.919	0.98	0.0072
	1060.94	77.551	1.036	0.98	0.0085

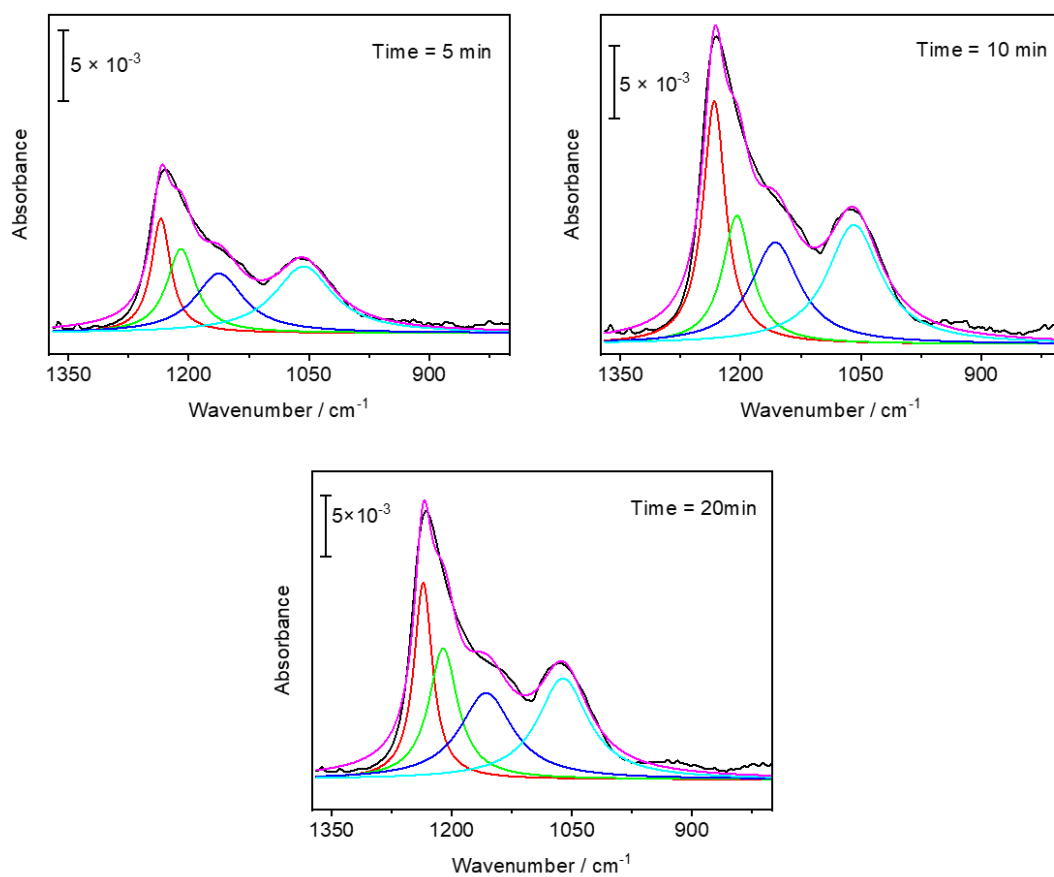


Figure A6. Lorentzian deconvolution of spectra of Si-O-Si modes of strained H-Si(111) (strain level = 0.3%) in different reaction times with water.

7. Lorentzian deconvolution of Si-H stretching mode

Table A7. Data for the best fit to the stretching Si-H stretching mode in Figure 10a (main manuscript): wavenumber, full-width at half maximum (FWHM) of the peaks from the Lorentz line shape, Area, R-value and Height (H).

<i>Reaction time (min)</i>	<i>Wavenumber / cm⁻¹</i>	<i>FWHM</i>	<i>Area</i>	<i>R-Quadrat</i>	<i>H</i>
0.5	2083,21	7,539	0,0061	0.99	5,22E-4
	2070,10	9,405	0,0015	0.99	1,03E-4
	2061,52	9,414	5,95E-4	0.99	4,02E-5
	2095,95	10,825	0,0021	0.99	1,23E-4
	2108,78	7,855	6,59E-4	0.99	5,34E-5
2	2082,64	11,495	0,0042	0.99	2,35E-4
	2071,21	7,940	0,0015	0.99	1,21E-4
	2064,59	4,482	4,32E-4	0.99	6,14E-5
	2095,20	12,891	0,0025	0.99	1,24E-4
	2107,44	10,349	8,889E-4	0.99	5,46E-5
5	2083,28	12,135	0,0054	0.97	2,83E-4
	2096,67	9,779	0,0016	0.97	1,09E-4
	2107,81	8,846	6,75E-4	0.97	4,86E-5
	2070,35	7,462	0,0013	0.97	1,17E-4
	2064,55	2,874	3,038E-4	0.97	6,73E-5
10	2083,00	12,787	0,0025	0.99	1,24E-4
	2069,71	11,340	0,0013	0.99	7,75E-5
	2062,95	3,002	1,686E-4	0.99	3,57E-5
	2094,58	13,262	0,0015	0.99	7,44E-5
	2109,89	10,005	4,20E-4	0.99	2,67E-5
20	2081,94	12,249	0,0021	0.97	1,10E-4
	2072,91	9,053	8,17E-4	0.97	5,749E-5
	2065,23	7,180	6,73E-4	0.97	5,96E-5
	2093,19	12,364	0,0014	0.97	7,56E-5
	2105,48	8,568	2,33E-4	0.97	1,732E-5

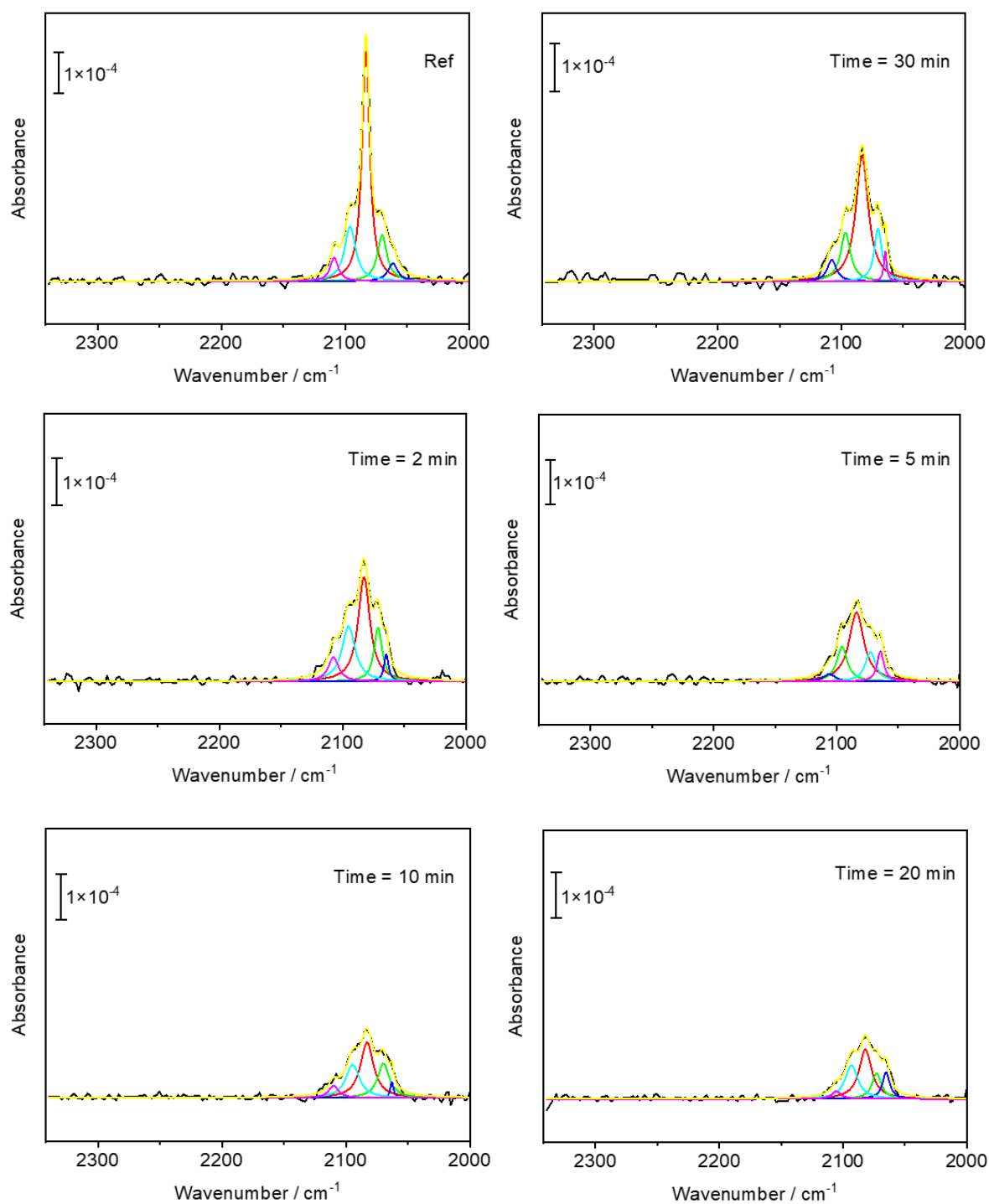


Figure A7. Lorentzian deconvolution of spectra of Si-H stretching mode of strained H-Si(111) (strain level = 0.3%) in different reaction time with water.

8. DFT calculation of oxygen effect on Si-OH peak position

The Si-OH peak position at around 809 cm^{-1} remained constant during the reaction time between strained H-Si(111) and water, according to the data for the fit of Si-OH (Table 5). Based on this observation, we conclude that the surface will be converged by $\text{Si}_3\text{Si-OH}$ and SiO_x , since residing oxygen under Si-OH results in peak position¹³⁷. To test this hypothesis, we construct three hydroxylated strained H-Si(111) models with different number of oxygen beneath the Si-OH group. Consistent with our assumption, results demonstrate that atop Si-OH vibrational mode are blue-shifted owing to the influence of oxygen. When the number of oxygen increases, the bending and stretching peaks corresponding to the Si-OH modes are blue-shifted by 15.2 cm^{-1} and 80.2 cm^{-1} , respectively. However, the measured peak position for bending vibration of Si-OH remained constant following generation of Si-O-Si peaks. The concluding remark could be covering the surface by $\text{Si}_3\text{Si-OH}$ and SiO_x groups.

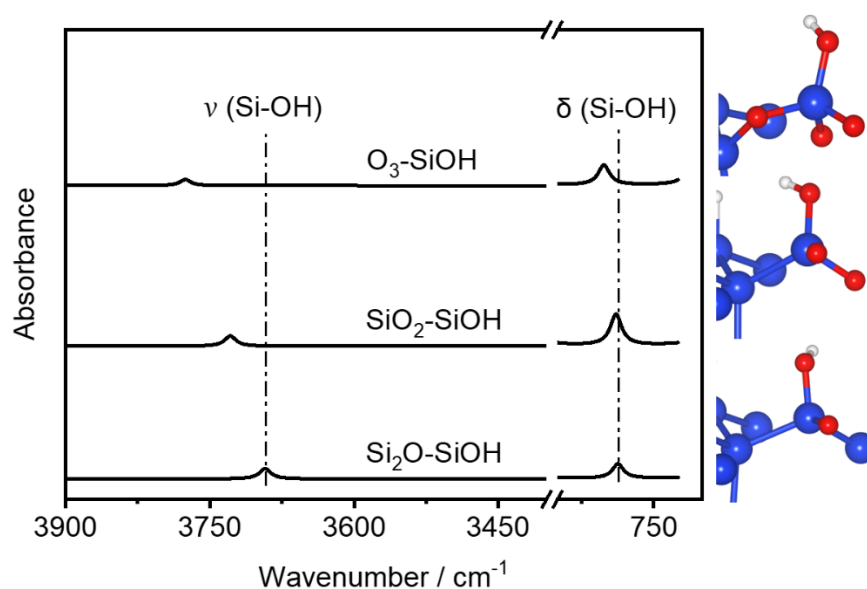


Figure A8. Calculated IR spectra of oxide surfaces strained H-Si(111) as a function of number oxygen being reside below Si-OH.

9. DFT calculation of reactivity of strained H-Si(111) with water

The reaction of one molecule of water with H-Si(111) while the Si-H-Si formation is occurred along the $[4\bar{4}\bar{1}]$ direction is demonstrated in Figure 9. The images show water decomposition upon adsorption. We concluded from the results that oxidation of up bonds is facilitated by the tensile strain as the following observations: Si atom from the Si-H-Si group (purple arrow) and one hydrogen from water molecule adsorbed with each other. H cap reacts with O in an up bond oxidation forming Si-OH without any energy barrier. Also, H-Si-Si-H group is formed through a reaction between the underlying silicon (orange arrow) and the second hydrogen of the water molecule. The length of the Si-Si bond in the coupled monohydride (H-Si-Si-H) is closer to the bond length (2.35 Å) than Si(111) presenting as $d_{\text{Si-Si}} = 3.84$ Å.

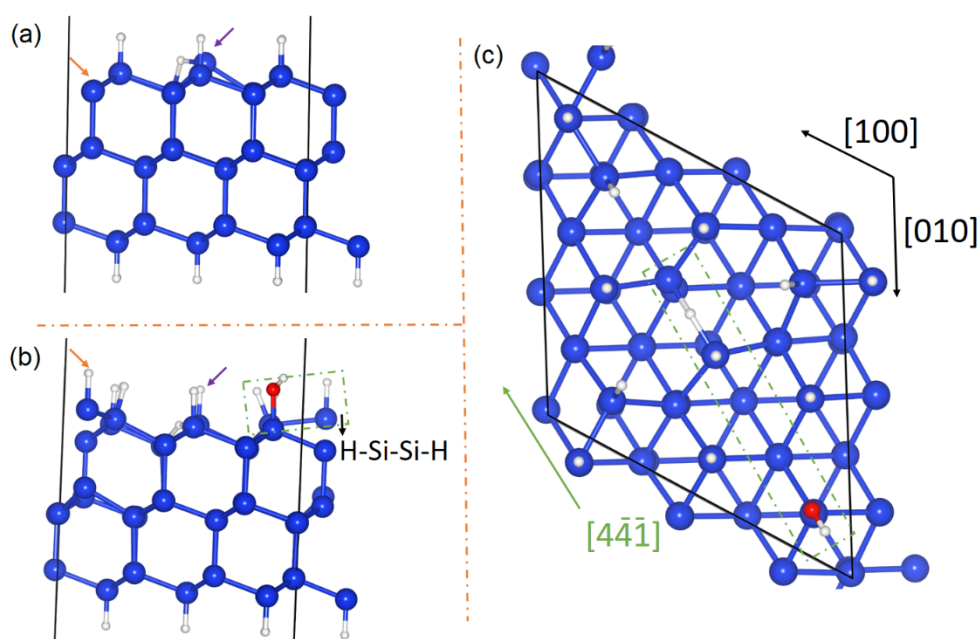


Figure A9. First step of the reaction between strained model (formed Si-H-Si along the $[4\bar{4}\bar{1}]$ direction) with water; (a) structure of model before the reaction with water, (b) new configuration of structure after reaction with water which show the formation of Si-OH (reaction between Si-H up bond with O of water), H-Si-Si-H (reaction between underlying Si (shown with orange arrow) with H of water and Si-H-Si-H (reaction between the Si of Si-H-Si group (shown with purple arrow) with H of water), and (c) top view of structure after reaction with water.

Appendix B: In situ contact angle measurement during mechanical test

1. In-situ contact angle measurement during the reaction of strained H-Si (111) with glycerol

Instead, we designed wetting experiment that allow us to measure directly the strain impact on surface reactivity by measuring the contact angle. Robust measurement of contact angle (CA) is a labor task because the rate of water evaporation is too high. This remains when applying same condition in the present experiment. Glycerol has the surface tension of $\gamma = 0.063$ N/m and thereby in our experiment, it is an appropriate candidate to produce a droplet instead of water. Droplets are placed near the center of wafers and viewed from the side with an optical microscope. In order to assure with the equilibrium of the contact line, contact angle is measured within about 10 min of droplet deposition. Young-Dupre's law is utilized in which $\gamma_{lv} \cos \theta_Y = \gamma_{sv} - \gamma_{sl}$, where s, l and v indicate the solid, liquid, and vapor phases and θ_Y is the contact angle at equilibrium. Freshly unstrained H-terminated surface exhibit a contact angle of $\sim 74^\circ$, which decrease with strain due to the increasing the chemical attack (Figure 4.15). The experiments are performed in controlled atmosphere of N_2 gas with glycerol as a non-volatile liquid. So, decreasing in contact angle is not explained by evaporation of the liquid. Decreasing contact angle with strain is clear evidence for spreading the glycerol droplet due to increase of hydrophilicity of the surface associated with the transformation $Si - H \rightarrow Si - OC_3H_7O_2$ occurring under strain condition.

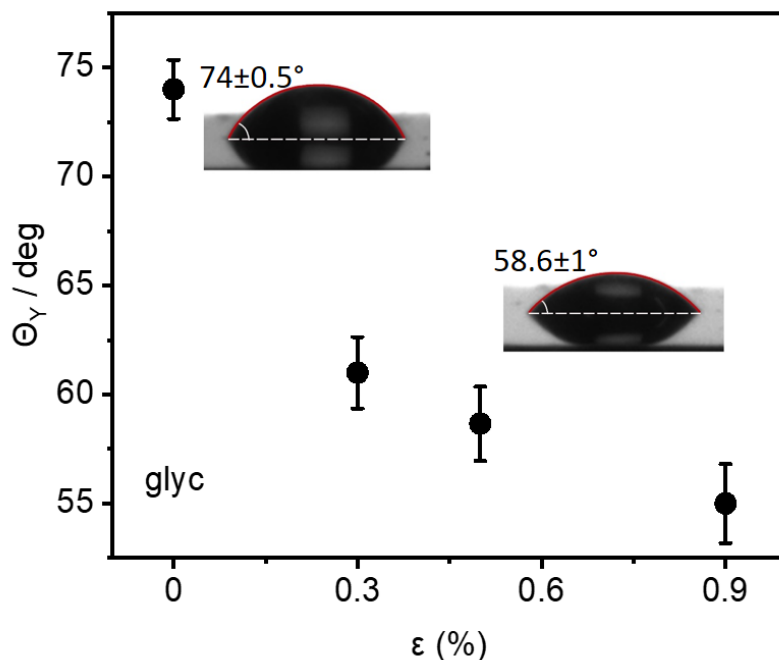


Figure B1. Contact angle measurement on H-Si(111) as a function of strain. The images related to unstrained and 0.5% strained samples are shown. Anything below the horizontal white dashed line is a reflection of the substrate. The error bar is standard error averaged based on the three repeated experimental results at least.

In carrying out the contact angle measurements, care must be taken to ensure that change in physical roughness does not cause artifacts. Therefore, the chemical reactivity of glycerol with ϵ -H-Si (111) is also tested using FTIR measurement (Figure 4.16) and NEB calculation (Figure 4.17). The FTIR spectrum of ϵ -H-Si (111) after reaction with glycerol is indicated in Figure 10 (b). Signals in the range of $2940\text{-}2870\text{ cm}^{-1}$ are attributed to the symmetric and asymmetric stretching vibration of methylene group. The exchange of some atop Si-H groups with atop Si-OC₃H₇O₂ groups is demonstrated by the appearance of a complex mode involving C-H stretching and bending motions, respectively, at $2940\text{-}2870\text{ cm}^{-1}$ and $\sim 750\text{-}800\text{ cm}^{-1}$, C-O stretching vibration around 1100 cm^{-1} , combined with decrease in Si-H intensity peak.

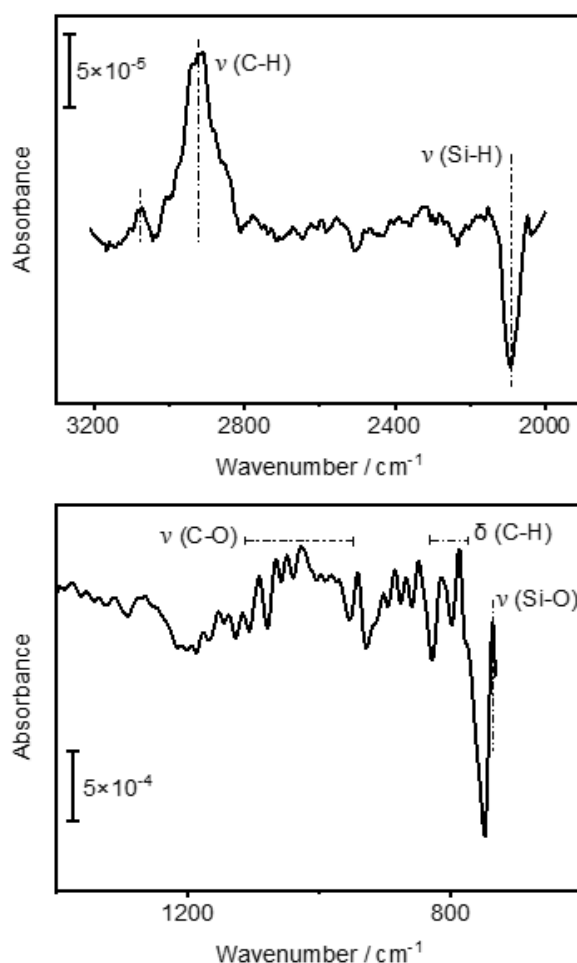


Figure B2. FTIR spectra of strained H-Si(111) after 20 min reaction with glycerol (volume = $0.2\ \mu\text{l}$). The spectrum is referenced relative to the unstrained fresh H-Si(111).

The NEB results (Figure 4.17) confirm that despite direct chemisorption is not occurred, there is only a kinetic barrier equal to 0.183 eV (4.2 kcal mol^{-1}) for converting physisorption to chemisorption that is consistency with reaction at room temperature. Given all the consistency checks that have been performed (NEB calculation and FTIR measurement), it is clear that chemical reaction on the surface cause of our main observation.

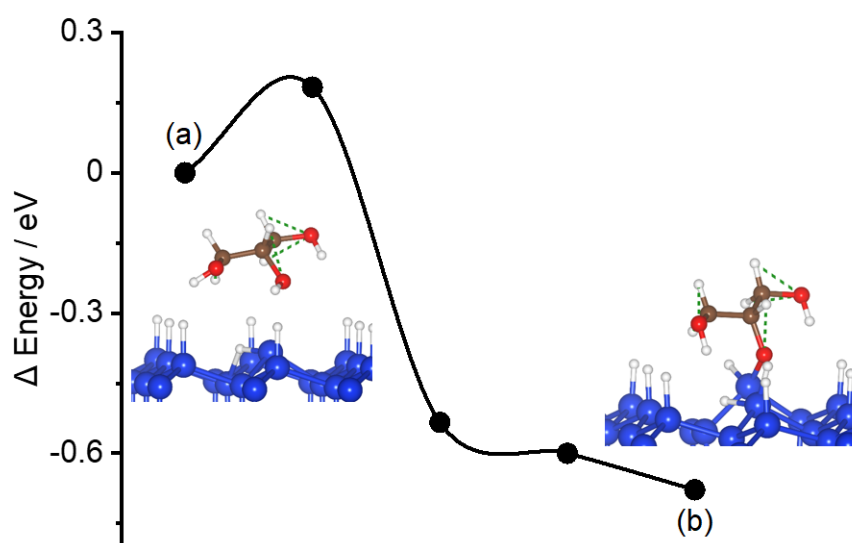


Figure B3. Figure B3. Reaction pathway for the reaction of glycerol on strained H-Si(111), (a) and (b) indicate the initial and final structures, respectively.

Moving forward, our study is motivated by the on-going- debate on whether or not surface reactivity on strained surface can be monitored by contact angle measurement. Decreasing the contact angel with strain justifies the diffusion of glycerol droplet due to increasing in hydrophilicity of the surface in association with the following transformation, which occurs under strain condition ($\text{Si} - \text{H} \rightarrow \text{Si} - \text{OC}_3\text{H}_7\text{O}_2$).

LIST OF ABBREVIATIONS

DFT.....	Density Functional Theory
H-Si(111).....	Hydrogen- terminated Silicon(111)
IR.....	Infrared
IC.....	Integrated Circuit
FTIR.....	Fourier Transformation Infrared Spectroscopy
e-ph.....	electron-phonon
MOSFET.....	metal-oxide-semiconductor field-effect transistor
CMOS.....	complementary metal-oxide-semiconductor
STM.....	scanning tunneling microscopy
AFM.....	atomic force microscopy
ASCE.....	American Society of Civil Engineers
ITZ.....	interfacial transition zone
PVA.....	Polyvinylalcohol
SBR.....	Styrene Butadiene Rubber
SMPs.....	Shape-memory polymers
T _g	glass transition temperature
MDI.....	diphenylmethane diisocyanate
PEG.....	poly ethylene glycol
DMPA.....	dimethylolpropionic
FCC.....	Face-Centered Cubic
HF.....	hydrogen fluoride
PES.....	potential energy surface
NEB.....	Nudged Elastic Band
MEP.....	minimum energy pathway
FRP.....	fiber-reinforced plastics
SHG.....	second-harmonic generation
CZ.....	Czochralsk
DTGS.....	pyroelectric detector
VASP.....	Vienna ab initio simulation package
PBE.....	Perdew-Burke-Ernzerhof
PAW.....	projector augmented wave
TCB.....	three-center bond
TO.....	transverse optical
LO.....	longitudinal optical
BZ.....	Brillouin Zone
SE.....	Spectroscopic Ellipsometry
AS.....	asymmetrical stretching

AS1.....	in-phase asymmetric stretching
AS2.....	out-of-phase asymmetric stretching
FWHM.....	full-width at half maximum
PU.....	polyurethane
EDX.....	Energy-dispersive X-ray spectroscopy
OE.....	oxyethylene
LEED.....	Low Energy Electron Diffraction
IRRAS.....	infrared reflection absorption spectroscopy
NC-AFM.....	non-contact atomic force microscopy
L.....	Langmuir

LIST OF FIGURES

Figure 1.1. Schematic illustration of general concept behind the strain-induced changes on the microstructure which lead to increasing surface reactivity. Dark and blue colors represent silicon atoms, whereas white and pink colors represent hydrogen atoms. Our hypothesis was that strain caused changes in the microstructure of H-Silicon(111), such as hydrogen diffusion and the formation of new bonds. The formation of new bond like Si-H-Si is shown in the picture of ϵ -H-Silicon(111). 2

Figure 1.2. Schematic illustration of calcite(10.4) surface as one of the main gas adsorption reservoir. Carbon, oxygen, and calcium are represented by the colors black, red, and blue, respectively. 3

Figure 1.3. Schematic illustration of SiO₂@polymer-matrix composite before and after mechanical test. The multiple pathways of energy adsorption by materials compounds are represented by the IR graph derived from the in-situ IR measurement during the mechanical test. Blue, yellow and orange colors represent the cement-matrix, SiO₂ particles and polyurethane, respectively. Our assumption was that the mechanical energy is often transferred through the entire process of specimen deformation and destruction that can be detected through the bond vibrations. 3

Figure 2.1. Top (a) and side (b) views of the (1×1) calcite(10.4) surface model (a = 5.0 Å and b = 8.1 Å). The marked green section shows the atoms exposed at the surface, revealing that the oxygens are located at two different but equivalent positions. (red: oxygen, black: carbon, blue: calcium). 8

Figure 2.2. Schematic illustration of polymer (diphenylmethane diisocyanate (MDI), poly ethylene glycol (PEG) and dimethylolpropionic acid (DMPA)) coated SiO₂ particles used as admixture into the cement past. Different molecular weight of PEG (600 and 1500 g mol⁻¹) is used. N – H and C = O associated with the urethane groups which is expected to be observed in IR results after synthesis of polymer. 11

Figure 2.3. 2-dimensional diagram for (a) an undeformed lattice and (b) a deformed lattice¹⁶. x and y are two unit vectors to represent the unstrained lattice, and in the simple square lattice, they correspond to the lattice basis vectors. 12

Figure 2.4. Illustration of an infinitesimal cube's surface stress components¹⁶. $\tau_{\alpha\beta}$ where $\alpha, \beta = x, y, z$ represents force applied in the α direction to the unit area of the plane whose outward-drawn normal lies in the β direction. 13

Figure 2.5. Crystal structure representing (a) (100) orientation (b) (111) orientation. 14

Figure 2.6. Structure of Si(111) (a) Top view, (b) Side view. The hexagonal symmetry of Si atoms is shown in top view image. Green and blue Si atoms are located under the surface and on the surface, respectively. The distance between Si atoms is 3.84 Å. 14

Figure 2.7. Mechanism leading to the formation of H-terminated Si surface by HF etching: The last step of oxygen removal from SiO₂ involves HF attack of the Si–O bond, with removal of OH as H₂O and termination of the surface Si atom with F. Further attack of the p-polarized Si ^{δ^-} –Si ^{δ^+} leads to H-termination⁸². Partially positive and negative charges of atoms are indicated as + and -, respectively. 15

Figure 2.8. Water drop on a surface (a) with water contact angle θ , (b) advancing θ_a and (c) receding

θ contact angles.....	16
Figure 2.8. Young's model of surface wetting for flat surfaces; θ indicates static contact angle, and γ_{LV} , γ_{SL} and γ_{SV} are interfacial free energies of the liquid-vapour, solid-liquid, and solid-vapour interfaces, respectively.....	17
Figure 2.9. Two components make up the nudged elastic band force F^{NEB} : the spring force F_i^{SII} , along the tangent $\hat{\tau}_i$, and the perpendicular force due to the potential F_i^\perp . The unprojected force due to the potential F_i is also shown for completeness.....	20
Figure 3.1. Bruker's 3-point-bend test setup on UMT Tribo laboratory. The image is taken from the 3-Point Bend Testing Bruker.....	23
Figure 3.2. (a) Technical drawing of our self-made machine, (b) schematic illustration of the relation between the radius of curvature, ρ , wafer curvature and the strains within a wafer exposed to bending moments.(c) The graph shows the procedure of applying loading on the sample in different positions (the number of positions is equal to the number of spindle steps) and (d) the schematic illustration of the self-made instrument contain stepper motor, movable sample holder (1), sample (2), nose-like metal piece (3) and (4) spindle.....	24
Figure 3.3. IR spectra of repeated measurements on gold-coated Aluminum which was bended equal to 2,9 μm in each step.....	25
Figure 3.4. (a) Technical drawing of our second self-made bending device. (b) The schematic illustration of our self-made mechanical device for measuring in-situ contact angle while bending. Different parts of this machine are shown; needle (1), the white box which is filled by N_2 gas to keep the sample from the environment (2), sample (3), spindle (4), empty place to screw the mechanical machine with Shape-Analyzer-DSA100E device (5) and stepper motor (green part).....	26
Figure 3.5. The actual images of our self-made mechanical devices; (up) the image of first device which was placed into glovebox for in-situ IR measurement, and (down) the picture of second device which was combined with drop shape analyzer machine.	27
Figure 3.6. Electromagnetic spectrum. Infrared regions are separated into three regions: (1) Near-infrared ($12820\text{-}4000\text{ cm}^{-1}$); Mid-infrared ($4000\text{-}400\text{ cm}^{-1}$) and Far-infrared ($400\text{-}33\text{ cm}^{-1}$) ¹⁰⁹⁻¹¹⁰	28
Figure 3.7. The optical diagram of a Michelson interferometer ¹⁰⁷ . The Michelson interferometer has four arms. The infrared source, as well as a collimating mirror that collects the light from the source and aligns its rays, are housed in the upper arm. A fixed mirror is a mirror that does not move and is in a fixed position in the Michelson interferometer's bottom arm.	29
Figure 3.8. A plot of light intensity (or detector signal) versus optical path difference for a mirror moving away from the beamsplitter in a Michelson interferometer. Such a plot is called an interferogram. This is the interferogram for a single wavelength of light passing through the interferometer ¹⁰⁷	30
Figure 4.1. Flow diagram of applying strain and measuring IR spectra of hydrogen terminated silicon(111).....	32

- Figure 4.2.** Flow diagram of procedure to study the reactivity of unstrained hydrogen terminated silicon toward liquid water at different reaction times of 0.5- 2- 5- 10 and 20 minute..... 33
- Figure 4.3.** Flow diagram of procedure to study the reactivity of strained hydrogen terminated silicon (strain level = 0.3%) toward liquid water at different reaction times of 0.5- 2- 5- 10 and 20 minute. 34
- Figure 4.4.** FTIR spectra of H-Si(111) surface subjected to different strain levels (percent). The dark blue spectrum (Ref) is corresponding to unstrained sample (fresh H-Si(111)). Spectrum of sample (silicon(111)) after piranha cleaning is used as background for all of the presented spectra. 35
- Figure 4.5.** Variation of peak intensity as a function of strain: (a) intensity of stretching Si-H mode, (b) intensity of new induced band (three center bond (TCB)) due to strain effect, and (c) intensity of bending Si-H mode. All of the peaks are fitted by Lorentzian function (Appendix A, Table A1, A2 and A4). 36
- Figure 4.6.** Possible configuration that resulted from strain effect on Si-Si and Si-H bond length and orientation; hydrogen diffusion, breaking Si-Si bond and formation of Si-H-Si (TCB). (a) and (b) show the side and top views of models, respectively. (c) Represent the part of models experienced higher change following hydrogen movement. Information regarding the Si-Si and Si-H bonds (presented in (c)) is provided in Table 4.2. (d) Measured bond distance of Si-H-Si using CrystalMaker software, and (e) calculated IR spectra of unstrained H-Si(111) (green curve) and 0.3% strained model (along [100] direction) containing Si-H-Si bond (blue curve). Molden is used to define the type of the vibrational modes of the TCB bond (Appendix A, Table A3). 38
- Figure 4.7.** IR spectra of an unstrained H-Si(111) before (black curve, Ref) and after reaction with water (green curves) as a function of reaction time. The numbers (0.5, 2, 5, 10 and 20) represent the reaction times which are expressed in minute. The spectrum of sample after piranha cleaning (not shown) is used as background for all spectra. For clarity, the results are plotted in to separate spectra region of (a) 2310-2050 cm^{-1} and (b) 1300-800 cm^{-1} . (c) Energy profile as a function of reaction coordinate for the reaction of water with the Si-H bond and Si-Si back bond. The panels (a, b, c and d) indicate the energy of the critical points taking as a reference the water molecule adsorbed on the surface..... 40
- Figure 4.8.** IR spectra of strained H-Si(111) after reaction with water as a function of reaction time .Black curve (Ref) is spectrum of fresh $\text{NH}_4\text{F}/\text{HF}$ treated sample. The absorbance spectra are processed by subtracting IR spectrum of sample after piranha cleaning. The numbers (0.5, 2, 5, 10 and 20) show the reaction times (expressed in minute) of strained H-Si(111) (strain = 0.3%) with water. The spectra are separated into three important regions; (a) Si-H stretching peak, (b) generation of bending Si-OH mode, and (c) the formation of Si-O-Si modes. The data for the best fit with Lorentzian function is provided in Appendix A, Figures A5, A6 and A7. 42
- Figure 4.9.** Energy profile for the reaction of hydroxylated strained H-Si(111) with water. (a-c) Panels show the initial, intermediate and final structures, respectively..... 43
- Figure 5.1.** Photograph of a calcite (CaCO_3) single crystal mounted in the sample holder (designed for UHV cleavage) with the (10.4) surface pointing up. Size of the base plate of the sample holder is 8 x8 mm^2 46
- Figure 5.2.** (a) IRRAS spectra of CO adsorbed onto the calcite(10.4) surface with increasing exposures

using p-polarized light at 62 K. (b) IRRAS spectra for 2 mL CO adsorbed onto the calcite(10.4) surface at 62 K using p-polarized light (top) and s-polarized light (bottom).48

Figure 5.3. (a) IRRAS spectra for 2 mL of CO adsorbed onto calcite(10.4) surfaces at $T = 62$ K and after annealing to the temperatures indicated. (b) Integrated spectral intensity evolution as a function of temperature.49

Figure 5.4. NC-AFM imaging of single CO molecules on calcite(10.4) at 5 K with total deposition durations of (a) 25 s, (b and d) 50 s, and (c) 150 s. Data in (b and d) were acquired after dosing further 25 s onto the sample presented in (a). Data in (c) are acquired after dosing for 25 s and additional 125 s. Single CO molecules are marked by an arrow in all figures, molecules slightly off-center with white circles in (b). The (2×1) unit cell is marked by white rectangles in all micrographs.50

Figure 5.5. After energy minimization, side views of CO/calcite(10.4) for two distinct CO coverages of 0.5 ML (a) and 1.0 ML (b) (b and c). CO tilt angles are included.51

Figure 5.6. One carbon monoxide molecule (0.5 ML coverage, left) and a full monolayer of CO (right) on the energetically preferred adsorption site of a CaCO_3 surface unit cell. After their optimum configurations, F denotes the azimuthal angle of adsorbed CO.52

Figure 5.7. Change in surface energy of calcite(10.4) surface upon applying strain of 3%, 1%, -1% and -3%.53

Figure 5.8. Full monolayer of CO on the energetically preferred adsorption site of a strained CaCO_3 surface. After their optimum configurations, F denotes the azimuthal angle of adsorbed CO.55

Figure 5.9. Side views of CO/strained calcite(10.4) after energy minimization for two different CO coverages of 0.5 ML and 1.0 ML (b, c). (a) shows the images for strained calcite surfaces by 1% and (b) indicates the images of calcite surfaces strained by 3%.56

Figure 6.1. Schematic illustration of the effect of the particles on crack growth. It is believed that when mechanical force was applied to pure hardened cement paste, rapid crack propagation occurred, resulting in lower fracture force and abrupt mechanical force release. Incorporated particles, on the other hand, are supposed to act as a barrier to crack growth, resulting in the formation of new micro cracks that require energy to expand and move through the particles. As a result, more energy could be dissipated.61

Figure 6.2. Synthetic process of polyethylene glycol - 4,4-diphenylmethane diisocyanate - and dimethylolpropionic acid (PEG-MDI-DMPA). Different molecular weight of (60 and 1500 g/mol) was used.63

Figure 6.3. IR curves of synthetic polyurethane, SiO_2 particles and polyurethane coated SiO_2 particles (PU/ SiO_2).64

Figure 6.4. SEM images of (a): SiO_2 without polymer coating and (b): PU/ SiO_2 , the diameter of the inorganic core is between 5-250 microns and the thickness of the measured polymer coating for one of the particles is between 0.6 - 1 microns (c).64

Figure 6.5. The results of SEM/EDX investigations of the C-PEG-600 after 28 days (the images are taken from cross section of sample). Individual elemental maps reveal the presence of silicon related to

particles and carbon as cover around them. (b): higher magnification of SEM image which clearly indicates the existence of polymer coated compound in matrix, the measured polymer thickness is $3.92 \mu\text{m}$ 65

Figure 6.6. IR spectra of unmodified sample in different bending position. The value of deflection (d) for strain level is shown in μm . The black curve shows the zero position (deflection = 0). From up to down the value of curvature increase and the last spectra for each sample indicates the max deflection that is supported by samples before complete failure. 66

Figure 6.7. IR spectra of sample in various strain level for PEG-600-C. The black curve shows the zero position. The appearance of new peak (O-Si-O) is indication of different process of energy dissipation in the samples, contribution of SiO_2 particles. 67

Figure 6.8. IR spectra of sample in various strain level for PEG-1500-C. The black curve shows the zero position. The appearance of new peak (O-Si-O) and (O-H) groups are indication of different process of energy dissipation in the samples. 67

Figure 6.9. The measured intensity of the stretching vibration of (Si-O-Si), bending vibration of O-Si-O and C-O peaks of the CEM I 32.5R, PEG-600-C and PEG-1500-C as a function of curvature (μm). Each point represents one bending position when the samples undergo external mechanical force. 69

Figure 6.10. Two types of hydrogen bonding in PEG-MDI-DMPA. (a): hydrogen bonding between carboxylic acid, (b): hydrogen bonding between PEG and carboxyl group. Schematic illustration (c) shows PEG chain crosses and gets entanglement that might occurred with increasing the molecular weight of PEG. 70

LIST OF TABLES

Table 4.1. Calculated values of deflection, force and strain corresponding to number of steps.	34
Table 4.2. Calculated Si-Si and Si-H bond lengths for the optimized structures of two models, unstrained H-Si(111) and strained H-Si(111).....	39
Table 5.1. Adsorption energy and vibrational frequencies of unstrained and strained calcite(10.4) surfaces as a function of surface coverage.	54
Table 5.2. Parameter characterization of CO/strained calcite(10.4) after geometry relaxation. The parameters $x(\text{C-Ca}(\text{surface}))$, $y(\text{C-Ca}(\text{surface}))$ and $z(\text{C-Ca}(\text{surface}))$ denote the distance between the carbon atom of the adsorbed CO molecule and the surface Ca ion. $\text{Ca}_{(\text{surface})}\text{-O}_{(\text{subsurface})}$ indicate the distance between the surface Ca ion and O presented in the sublayer. Θ (tilt angle) and ϕ (azimuthal angle) are defined based on the presented methods in Figure 5.8 and 5.9a.	56
Table 5.3. Parameter characterization of CO/strained calcite(10.4) after geometry relaxation. The parameters $x(\text{C-Ca}(\text{surface}))$, $y(\text{C-Ca}(\text{surface}))$ and $z(\text{C-Ca}(\text{surface}))$ denote the distance between the carbon atom of the adsorbed CO molecule and the surface Ca ion. $\text{Ca}_{(\text{surface})}\text{-O}_{(\text{subsurface})}$ indicate the distance between the surface Ca ion and O presented in the sublayer. Θ (tilt angle) and ϕ (azimuthal angle) are defined based on the presented methods in Figure 5.8 and 5.9b.	57
Table 6.1. Detailed information of mixture compositions.....	62
Table 6.2. The obtained values of max deflection (d) and max curvature supported by the samples. The value of ultimate force, stress and strain corresponding with max deflection for each sample are also calculated based on the presented formula in experimental part.	68

ACKNOWLEDGEMENTS

First and foremost, I would like to thank Dr. Peter Thissen for allowing me to pursue my PhD in his working group. In addition, I would like to extend my gratitude to Prof. Christof Wöll for giving me a chance to be a part of the IFG team.

I'd like to express my thankfulness to the Deutsche Forschungsgemeinschaft (DFG) for their financial support of the implemented projects in thesis.

My sincere thanks to Jonas Wohlgemuth for the innumerable favors and help I have gotten from you and Franz Königer for all the nice and timely breaks and talks.

Deepest thanks to all my friends back in Iran (Rooja, Esmat, Malihe, Golshan) and many others all around the world for always being there.

Lastly, I would like extend my heartfelt thanks to all of my department colleagues who have been there throughout this journey, among them; Prof. Andreas Gerdes, Mohammadreza Izadifar, Nils Schewe, Beatriz Arevalo Galvan, Jonas Kaltenbach, Felix Krause and Mohammad Monjur ul Islam and Dr. Matthias Schwotzer.

LIST OF PUBLICATIONS

From this thesis

- **Effect of polymer-coated silica particles in a Portland cement matrix via in-situ infrared spectroscopy**, T. Mohammadi Hafshejani, Ch. Feng, J. Wohlgemuth, F. Krause, A. Bogner, F. Dehn, P. Thissen, **Journal of Composite Materials** (2021), <https://doi.org/10.1177/0021998320952152>
- **CO adsorption on the calcite(10.4) surface: a combined experimental and theoretical study**, T. Mohammadi Hafshejani, W. Wang, J. Heggemann, Al. Nefedov, S. Heissler, Y. Wang, Ph. Rahe, P. Thissen, Ch. Wöll, **Journal of Physical Chemistry Chemical Physics** (2020), <https://doi.org/10.1039/DOCP02698K>
- **Strain Activation of Surface Chemistry on H-terminated Si(111)**, T. Mohammadi Hafshejani, J. Wohlgemuth, P. Thissen, **Journal of Physical Chemistry C** (2021)

Conference Contributions

- **Energy Dissipation of the Modified Cement Matrix During Fracture Process**, 3rd International Conference on the Chemistry of Construction Materials 15.03.2021-17.03.2021, Online / talk
- **Investigation of Micro-stress at Si-SiO₂ interface using Infrared spectroscopy**, German Physical Society-DPG conference, 04.05.2019 / talk

